2009

A non-body conformal grid method for simulations of laminar and turbulent flows with a compressible large eddy simulation solver

Wen Wang
Iowa State University

A non-body conformal grid method for simulations of laminar and turbulent flows with a compressible large eddy simulation solver

by

Wen Wang

A dissertation submitted to the graduate faculty

in partial fulfillment of the requirements for the degree of

DOCTOR OF PHILOSOPHY

Major: Mechanical Engineering

Program of Study Committee:
Richard H. Pletcher, Co-major Professor
Shankar Subramaniam, Co-major Professor
Ted Heindel
Michael Olsen
Zhi Jian Wang

Iowa State University

Ames, Iowa

2009

TABLE OF CONTENTS

LIST OF TABLES

LIST OF FIGURES

ACKNOWLEDGEMENTS

I would like to take this opportunity to express my thanks to those who helped me with various aspects of conducting this research and the writing of this thesis.

First and foremost, I am deeply grateful to my major adviser, Professor Richard H. Pletcher for his guidance, patience and support throughout this research and the writing of this thesis. Professor Pletcher not only introduced me into the world of computational fluid dynamics, but also guided me into the depth and breadth of the research of large eddy simulation. His insights and words of encouragement have often inspired me and renewed my hopes for completing my graduate education. I would like to express my appreciation for my co-advisor, Professor Shankar Subramaniam, for leading me to the field of multiphase flow simulation. His lectures were among the best ones I have ever attended. I would also like to thank my committee members for their efforts and contributions to this work: Professor Ted Heindel, Professor Michael Olsen and Professor ZhiJian Wang. To Professor Wang, thanks are due for teaching me the advanced topics of CFD such as unstructured grid method and spectral volume method. To Professor Heindel and Professor Olsen, my gratitude extends to their invaluable advice on writing this thesis.

During my study in Iowa State University, my life and research have been enriched by my colleagues in CFD lab. I would like to thank all of my friends at ISU for their help and support. Last, but not the least, I am indebted to my parents for their unconditional love and support.

This research was partially supported by the DOE/NE Idaho Operations Office through contract DE-AC07-05ID14517 under the I-NERI program. The computer resources provided by the Iowa State High Performance Computing Center and the Minnesota Supercomputing Institute are gratefully acknowledged.

ABSTRACT

A non-body conformal grid method for simulation of laminar and turbulent flows within complex geometries is developed and incoporated into a compressible large eddy simulation (LES) solver. The underlying finite volume solver for the filtered compressible Navier-Stokes equations is based on a second-order dual-time step approach with preconditioning for low Mach number flow simulations. The time marching was done with an implicit lower-upper-symmetric-Gauss-Seidel (LU-SGS) scheme. The small scale motions were modeled by a dynamic subgrid-scale (SGS) model. The code was developed in a multiblock framework and parallelized using the message passing interface (MPI).

To satisfy the boundary conditions on an arbitrary immersed interface, the velocity field at the grid points near the interface is reconstructed locally without smearing the sharp interface. To treat the moving interface situation, a field extension strategy is used which resolved the velocity and pressure issues when a moving solid grid point becomes a fluid grid point.

A variety of laminar and turbulent flow problems are considered to validate the accuracy and range of applicability of the method. In particular, flow over a circular cylinder with different Reynolds numbers and Mach numbers is simulated and an order of accuracy analysis is conducted. A turbulent pipe flow is also solved with a Cartesian grid and good agreement of the simulation results with experimental results validates the capability of the current solver in turbulent flow simulations. Then a rectangular duct containing a cylindrical rod is studied and the simulation results are compared to those obtained from body-fitted grid methods. Next, turbulent heated flow simulations with a non-body conformal grid method are discussed. Laminar flow over a heated cylinder with different Reynolds numbers and temperature ratios is simulated first. The characteristic flow properties such as drag and lift coefficients, Strouhal

number and Nusselt number are compared to experimental results. Then the simulation of heated turbulent pipe flow with an isoflux boundary condition is presented using the non-body conformal grids. To demonstrate the applicability of the non-body conformal grid method in compressible flows, transonic and supersonic flow over a cylinder are simulated and qualitative results are studied. Next flow over an oscillating cylinder is studied to demonstrate the capability in solving flow over moving objects. Finally, as a representative of complex geometry flow, subchannel flow surrounding two cylindrical rods in a rectangular duct is studied and the simulation results are compared to simulation and experimental results by other investigators.

CHAPTER 1. INTRODUCTION

1.1 Motivation

Turbulence is one of the most important unresolved problems in engineering and science, especially for the complex geometries and fluid property variations occurring in the advanced reactor systems and their passive safety systems (McEligot et al., 2005). Improved computational techniques and supporting measurements are needed to assist the designs and system safety analyses for some operating conditions and hypothesized accident scenarios of these nuclear reactors. The geometries of the reactor cooling channels of some reactor concepts are illustrated in Fig. 1.1. Most of these geometries are more complex than those that have been used to generate the empirical correlations employed in the thermal hydraulic codes. These complex geometries may augement the heat transfer and pressure drop or they may cause stagnation regions with reduced velocities and thereby, increased thermal resistance leading to "hot spots". Computational thermal fluid mechanics is a very useful tool to provide detailed flow field analyses and help to understand the interacting phenomena induced by these geometries.

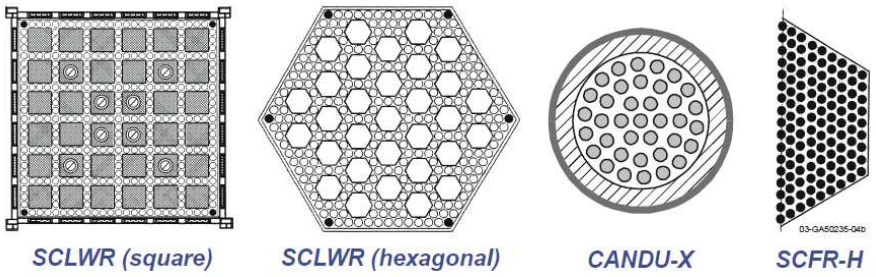

Figure 1.1 Some supercritical-pressure water reactor (SCWR) designs.

Direct numerical simulation (DNS), large eddy simulation (LES) and differential second

moment closures (DSM) are advanced computational techniques in turbulence modeling whose development has been extended to treat complex geometries and severe property variation for designs and safety analyses of supercritial-pressure water reactors (SCWRs).

• Direct numerical simulation (DNS), in which the Navier-Stokes equations are solved directly without any models and all scales of motion are resolved. To achieve such a resolution, the number of grid points in each direction is proportional to the ratio between the largest and smallest eddy in the flow, i.e., $Re_L^{3/4}$ (Pope, 2000), where Re_L is the Reynolds number based on the integral length scale of the flow. Thus the total number of points is $\propto Re_L^{9/4}$. Therefore, limited computer resources inhibit the resolution of flow characteristic of most applications by DNS.

• Reynolds-averaged method based on the Reynolds-averaged Navier-Stokes equations (RANS). The RANS equations are obtained by time or ensemble averaging of the Navier-Stokes equations. The effect of all the scales of motion is modeled. Although the RANS method has been a dominant approach of turbulent flow simulation, it appears that no model has emerged that gives accurate results in all flows without ad hoc adjustments of the model constants (Piomelli and Balaras, 2002). This may be due to the fact that, the large, energy-containing eddies are much affected by the boundary conditions, and universal models that account for the different dynamics of flow may be impossible to develop.

• Large eddy simulation (LES). The basic idea of this method is that only the large scale motions are computed explicitly while effects of the small scale motions are modeled. LES can be more accurate than the RANS approach because the small scales tend to be more isotropic and homogeneous than the large ones, and thus more ameanable to universal modeling. Furthermore, the subgrid scale stresses only contribute a small fraction of the total turbulent stresses. Compared to DNS, the computational cost is much less as the grid resolution is allowed to be coarser than the smallest scales.

• Combination of LES with wall models and detached eddy simulation (DES). DES employs the RANS method in the vicinity of solid walls while using LES away from the walls and into the main stream.

In the above four types of methods, DNS is regarded as the most accurate, and DNS results are usually used to verify and validate the other methods. However, since DNS has to use extremely fine grids to resolve all motion scales, it requires exceptionally large computational resources, especially for high Reynolds numbers, which severely limits its application. The RANS method is usually inexpensive, but its accuracy suffers much because of the uncertainty of the closure models. LES, which costs much less than DNS, but provides almost the same capability, can be thought of as an ideal compromise of accuracy and economy.

In LES, a spatial filtering (or averaging) operation is applied to the governing equations and the filtered quantities correspond to the motion of scales larger than the filter size (so called "large scales" or "large eddies"). Usually, the filter size is the same as the grid size. The filtered equations are solved in a time accurate manner. Since in turbulent flows, the turbulent fluctuations and viscous dissipation occur on a range of scales from the geometrical scale down to the Kolmogorov scale, which is much smaller than the grid size in LES, the information about the motions smaller than the grid size (so called "subgrid scale" or briefly, SGS) should be given. In the filtered equations, the effects of these subgrid scale motions are reflected in the so called subgrid scale stress and subgrid scale heat flux terms, which should be modeled. More details will be given in later chapters.

The main motivation for this research is to extend the LES capability to simulate complex geometry flows. It is hoped that the present research will provide certain perspectives in the application of non-body conformal grid method in engineering applications such as cooling flow surrounding irregular reactor core geometries or stirred-tank flow problems.

1.2 Objectives

The main objectives of this research are listed below and discussed in more detail subsequently.

- Incorporate the non-body conformal grid method into a large eddy simulation (LES) solver.
- Analyze the order of accuracy of the non-body formal grid method.

• Discuss the turbulent characteristics of duct sub-channel flows using LES combined with the non-body conformal grid method.

• Extend the non-body conformal grid method to simulate heat transfer problems.

• Study the capability of the non-body conformal grid method in simulation of compressible flows.

• Study the capability of the current non-body conformal grid method in simulation of flow over moving objects.

• Study particle laden turbulent flows.

1.3 Literature reviews

1.3.1 Complex geometry flow simulation

Traditionally, the typical simulation methods for complex flows are either based on body-fitted grid multi-block methods or unstructured grid methods. In the last decade, another alternative method, immersed boundary (IB) method, has been introduced and a series of complex flow computations have been tested with this method. The primary advantage of the IB method is that the task of grid generation is greatly simplified. Generating body-conformal structured or unstructured grids is usually very cumbersome. Even for simple geometries, generating a good-quality body-conformal grid can be an iterative process requiring repeated adjustment of grid parameters based on solution quality. As the geometry becomes more complicated, the task of generating an acceptable grid becomes increasingly difficult. In the structured grid method, complex geometries are often decomposed into multiblocks. Apart from the possible complexity introduced into the solution algorithm, grid smoothness on the interface between different blocks is another concern. The unstructured grid approach is inherently better suited for complex geometries due to its standardized grid generation process. However, grid quality can dereriorate with increasing comlexity of the geometry. When compared with unstructured grid methods, the Cartesian grid based IB method retains the advantage of powerful line-iterative techniques and geometric multigrid methods.

Another advantage of the Cartesian grid-based IB method is observed in the simulation

of flows with moving boundaries. Simulating such flows on body- conformal grids requires regeneration of the grid system at each time step and projection of the solution onto this new grid. This process inevitably introduces more complexity and computational cost to the solution procedure. In contrast, the moving boundary problem can be easily handled with the IB method since there is no need to regenerate the underlying grid system.

1.3.1.1 Turbulent flow simulation with immersed boundary methods

The immersed boundary method has been successfully incorporated into incompressible flow solvers to solve a series of turbulent flows problems such as flow in an impeller stirred tank mixer (Verzicco et al., 2004), flow around a road-vehicle (Moin, 2002), flow over a wavy boundary (Tseng and Ferziger, 2003) and tip-clearance flow of an axial turbomachine (You et al., 2004). Ovchinnikov et al. (2006) used DNS and LES to simulate the boundary layer transition behind a circular cylinder for Reynolds numbers $Re_D = 385, 1155$ and 3900. Rapid, bypass-like transition to turbulence is observed in the two highest Reynolds number cases. Qualitative similarities between wake-induced transition and bypass transition due to free-stream turbulence were discussed.

However, the implementation of this approach for compressible, viscous flows is limited. Ghias et al. (2007) has employed the "ghost cell" approach in a viscous compressible flow solver to solve a flow over a cylinder and an airfoil problem. Even though no turbulent flow case was solved, very good results were obtained by incoporating the IB method into a compressible flow solver. Palma et al. (2006) successfully employed the immersed boundary method and a $k - \omega$ turbulence model to simulate a compressible flow over a cylinder at Reynolds number $Re_\infty = 2 \times 10^5$ and Mach numbers $M_\infty = 1.3, 1.7$. Good agreement with experimental results for pressure coefficient and drag coefficient was observed.

1.3.2 Non-body conformal grid methods

Since the pioneering work of Peskin (1972), the terminology of "immersed boundary (IB) method" has been specifically used for the continuous forcing IB method. To compare a series of

numerical methods based on non-body conformal grids, we use the term "non-body conformal grid method" in this study to refer to a broader group which includes both continuous forcing and discrete forcing methods. The non-body conformal grid methods can be categorized into two major classes: a "sharp interface" approach and a "smooth/diffuse interface" approach (Gilmanov and Acharya, 2006). **Sharp interface** methods include: (i) Cartesian cut-cell method (Yang et al., 1997); (ii) Sharp interface Cartesian grid method (Udaykumar et al., 2001); (iii) Hybrid Cartesian immersed boundary method (Gilmanov and Acharya, 2006) and (iv) Embedded boundary method (Fadlun et al., 2000). **Diffuse interface** methods include: (i) Immersed boundary method (Peskin, 1972); (ii) Diffusive interface method (Anderson et al., 1998); (iii) Immersed interface method (Xu and Wang, 2006) and (iv) Smooth interface method (Yamamoto et al., 2004).

1.3.2.1 Immersed boundary (IB) method

The so-called immersed boundary method pioneered by Peskin (1972) was used to study fluid-structure interaction problems in cardiovascular circulation. In these computations the vascular boundary was modeled as a set of elements linked by springs. As a result the forces required to enforce boundary conditions could be evaluated with Hook's law. Since the force is incorporated into the govering equation before discretization, the advantage of this method is that it can be formulated independently of the underlying spatial discretization. The proposed IB method employed a mixture of Eulerian and Lagrangian variables, where the immersed boundary was represented by a set of discrete Lagrangian markers embedding in the Eulerian fluid domain. Those markers can be treated as force generators to the fluid, and move along with the fluid. The interaction between the Lagrangian markers and the fluid variables defined on the fixed Eulerian grid was linked by a well-chosen discretized delta function. The fundamental concept of the immersed boundary method is described next.

Suppose the immersed boundary is represented by a series of points defined by the parametric form $\mathbf{X}(s), \mathbf{X} \in \Gamma$, the force density acting on the fluid $\mathbf{f}(\mathbf{x}, t)$ and the boundary force

density on the immersed interface $\mathbf{F}(\mathbf{X}(s),t)$ are

$$\begin{aligned} \mathbf{f}(\mathbf{x},t) &= \int_\Gamma \mathbf{F}(\mathbf{X}(s),t)\delta(\mathbf{x}-\mathbf{X}(s))ds, \quad (1.1)\\ \mathbf{F}(\mathbf{X}(s),t) &= \mathbf{S}(\mathbf{X}(s),t), \quad (1.2)\end{aligned}$$

where function $\mathbf{S}$ satisfies a generalized Hook's law if the boundary is elastic. For rigid boundaries, $\mathbf{S}$ will represent a stiff passive force which tends to keep the boundary very close to the specified configuration (Lai and Peskin, 2000).

Mathematically, $\mathbf{f}$ can be viewed as a distribution function whose action on any test function $\mathbf{w}(\mathbf{x},t)$ is defined by

$$\begin{aligned} \langle \mathbf{f},\mathbf{w}\rangle &= \int_\Omega \mathbf{f}(\mathbf{x},t)\cdot\mathbf{w}(\mathbf{x},t)d\mathbf{x}\\ &= \int_\Omega\int_\Gamma \mathbf{F}(\mathbf{X}(s),t)\delta(\mathbf{x}-\mathbf{X}(s))ds\cdot\mathbf{w}(\mathbf{x},t)d\mathbf{x}\\ &= \int_\Gamma \mathbf{F}(\mathbf{X}(s),t)\cdot\int_\Omega \mathbf{w}(\mathbf{x},t)\delta(\mathbf{x}-\mathbf{X}(s))d\mathbf{x}ds\\ &= \int_\Gamma \mathbf{F}(\mathbf{X}(s),t)\cdot\mathbf{w}(\mathbf{X}(s),t)ds. \quad (1.3)\end{aligned}$$

Practically, if we choose $\mathbf{w}(\mathbf{x},t)$ to be the velocity $\mathbf{u}(\mathbf{x},t)$, then the above identity implies that the total work done by the immersed boundary is equal to the total work done on the fluid. However, the IB method is developed to handle mostly the fluid problem with elastic structures. For rigid boundaries or structures, Lai and Peskin (2000) suggested a formation

$$\mathbf{F}(\mathbf{X}(s),t) = \kappa(\mathbf{X}^e(s)-\mathbf{X}(s)), \quad (1.4)$$

where κ is a positive constant such that $\kappa >> 1$. The basic idea of this formation is to connect the boundary points $\mathbf{X}$ to a fixed equilibrium points $\mathbf{X}^e$ with a very stiff spring whose stiffness constant is κ. So if the boundary points fall away from the desired location, the force on the spring will pull these boundary points back.

It should be noted that the grid points generally do not coincide with the immersed interface so the force needs to be distributed over a band of cells around each Lagrangian point. Therefore the sharp Dirac delta function δ should be replaced by a smoother distribution function and this method belongs to the "diffuse interface" category.

1.3.2.2 Feedback forcing method

Also adopting the mixture of Eulerian and Lagrangian variables, Goldstein et al. (1993) proposed the feed-back forcing method to simulate the flow with the solid boundary within the spectral method framework. The solid boundary was treated as a force generator where the force field was calculated by a feedback method based on the difference between the predicted velocity and the actual velocity of the boundary. Supposing a Dirichlet boundary condition $\mathbf{U}(\mathbf{x}_s, t') = \mathbf{U}_s(\mathbf{x}_s, t')$ is imposed on the boundary, the forcing term, according to Goldstein et al. (1993) is

$$\mathbf{f}(\mathbf{x}_s, t) = \alpha \int_0^t [\mathbf{U}(\mathbf{x}_s, t') - \mathbf{U}_s(\mathbf{x}_s, t')]dt' + \beta[\mathbf{U}(\mathbf{x}_s, t) - \mathbf{U}_s(\mathbf{x}_s, t')], \tag{1.5}$$

where $\mathbf{x}_s$ is the boundary point, α and β are negative constants having dimension $\propto 1/(T^2)$ and $\propto 1/(T)$, respectively. The first term with integral feedback is to create a force field that will asymptotically reduce the differece $\mathbf{U}(\mathbf{x}_s, t) - \mathbf{U}_s(\mathbf{x}_s, t)$. Since this term decreases in time as the integrand increases, it tends to enforce $\mathbf{U}(\mathbf{x}_s, t) = \mathbf{U}_s(\mathbf{x}_s, t')$ on the immersed boundary. The second term can be interpreted as the resistance opposed by the surface element to assume a boundary value different from $\mathbf{U}_s$. In an unsteady flow, the magnitude of α must be large enough so that the restoring force can react with a frequency which is bigger than any frequency in the flow. However, the value of the constants is flow dependent and there is not a general rule for their determination.

The major drawback of this forcing is that big values of α and β make the Navier-Stokes equation stiff and its time integration requires very small time steps. Goldstein et al. (1993) performed a stability analysis and they found that, when all the forcing terms are computed explicitly, a one or two orders of magnitude decreases in the time step size was required to ensure stability. This is very challenging for large scale calculations of turbulent flows. Although it was found that implicit calculation of the second term can alleviate the severe time step limitation, the determination of constants of α and β are still problem dependent.

1.3.2.3 Immersed interface method (IIM)

One of the motivations of IIM (LeVeque and Li, 1994) is to improve the accuracy of the IB method by using a sharp interface method that accurately captures discontinuities of the solution and its derivatives without smearing. For a simple analytically integrable, one-dimensional model problem, it is possible to formally derive a forcing term that enforces a specific condition on a boundary (Beyer and LeVeque, 1992). However, the same is not usually practical for the Navier-Stokes equations because the equations cannot be integrated analytically to determine the forcing functions. Therefore, this method will not be discussed in detail in this study.

1.3.2.4 Cut cell method

The primary motivation of the cut cell method is that conservation of mass and momentum can be guaranteed with a finite-volume approach. This methodology was introduced into the Cartesian grid methods to solve a series of flow problems such as in Ye et al. (1999), Udaykumar et al. (2001) and Kirkpatrick et al. (2003). In this method, cells that were cut by the immersed boundary were identified, and those with centerlines located in the fluid field were reshaped by discarding the portion lying in the solid. For those cells with centerlines located in the solid field, the part in the flow field was absorbed by the neighboring cells. Then a polynomial function was used to evaluate the flux on the irregular surfaces. This method has been used to simulate various flows with stationary and moving boundaries including flow-induced vibrations (Mittal et al., 2003), flapping foils (Mittal et al., 2002) and objects in free fall through a fluid (Mittal et al., 2004). However, extending this approach to three dimensions is not trivial and an iterative technique may be required due to different shapes of the cutting cells. Also, very small grid cells near the boundary can cause extra stiffness for the problem.

1.3.2.5 Direct forcing method

Without adopting the Lagrangian markers, Mohd-Yusof (1998) proposed a direct forcing method within the spectral framework, where direct momentum forcing was applied to a set of points adjacent to the surface and interior to the body. Therefore, information regarding

the locations of the Eulerian grids either external or internal to the immersed boundary must be determined. In this approach, the governing equations are first discretized on a Cartesian grid without regard to the immersed boundary. Then the discretization in the cells near the boundary is adjusted to account for its presence. This allows direct control over the numerical accuracy, stability and conservative properties of the solver. Another advantage of this method is that since the force field is directly computed from the momentum equations, the time step can be larger than with the previous methods. However, since the immersed boundary in general does not coincide with the grid points, the determination of the forcing locations and their magnitude may not be straightforward on the Eulerian grids.

Due to different means to impose boundary condition on the immersed boundary, direct forcing methods can be further categorized into methods through indirect means (Mohd-Yusof, 1997; Verzicco et al., 2004; Balaras, 2004) and those that directly impose the boundary conditions on the IB (Ghias et al., 2007). Since the Navier-Stokes equations cannot be integrated analytically to determine the forcing function, Mohd-Yusof (1997) developed a method that extracted the forcing directly from the numerical solution for which an *a priori* estimate can be determined. Consider the incompressible Navier-Stokes equations for flow past a body,

$$\begin{aligned} \frac{\partial \mathbf{u}}{\partial t} + \mathbf{u}\cdot\nabla\mathbf{u} + \frac{1}{\rho}\nabla p - \frac{\mu}{\rho}\nabla^2\mathbf{u} &= 0 \\ \nabla\cdot\mathbf{u} &= 0 \quad \text{in } \Omega_f, \end{aligned} \tag{1.6}$$

with boundary condition

$$\mathbf{u} = \mathbf{u}_\Gamma \quad \text{on } \Gamma_b, \tag{1.7}$$

where Ω_f is the flow domain and Γ_b is the boundary of the immersed body. An operator L (Mittal and Iaccarino, 2005) can be used to simplify the the system equation as

$$\begin{aligned} L(\mathbf{U}) &= 0 \quad \text{in } \Omega_f, \\ \mathbf{U} &= \mathbf{U}_\Gamma \quad \text{on } \Gamma_b \end{aligned} \tag{1.8}$$

with $\mathbf{U} = (\mathbf{u}, p)$. Due to the presence of the immersed body, the discretized equation was adjusted to take into account the drag force on the fluid and resulted in a modified equation

$$[L']\mathbf{U} = \mathbf{r}, \tag{1.9}$$

where $[L']$ is the modified discrete operator and $\mathbf{r}$ represents terms associated with the boundary condition on Γ_b. The basic idea of the direct forcing method is to pre-solve the equation $[L]\mathbf{U}^* = 0$ at each time step where $\mathbf{U}^*$ represents a prediction of the velocity field. A forcing $\mathbf{f}'_{ib}$ is then calculated as

$$\mathbf{f}'_{ib} = \mathbf{r} + [L]\mathbf{U}^* - [L']\mathbf{U}^* = \mathbf{r} - [L']\mathbf{U}^*, \tag{1.10}$$

where $\mathbf{r} = \mathbf{U}_\Gamma \delta(\mathbf{X} - \mathbf{x})$ and

$$[L'] = [L] + ([I] - [L])\delta(\mathbf{X} - \mathbf{x}). \tag{1.11}$$

The major advantage of this method is the absence of user-specified parameters and the elimination of associated stability constraints. For instance, in Fadlun et al. (2000) and Balaras (2004), the solution was reconstructed at the fluid nodes closest to the immersed boundary (fluid points with at least one neighbor in the solid phase). In Fadlun et al. (2000), a one-dimensional interpolation scheme along an arbitrary grid line was used while in Balaras (2004) the reconstruction was performed along the well-defined line normal to the interface.

For high Reynolds number flows, the local accuracy is assumed to be very important and it is desired to reduce the spreading effect of the smooth force distribution function. Therefore, other approaches were also considered to modify the computational stencil near the interface to directly impose the boundary condition on the IB. The example applications are the "ghost-cell" approach (Majumdar et al., 2001; Tseng and Ferziger, 2003). In this method, ghost cells are defined as cells in the solid that have at least one neighbor in the fluid. For each ghost cell, an interpolation scheme that implicitly incorporated the boundary conditions on the IB is employed. For laminar flows or low Reynolds flows where the first gird is located within the viscous sublayer, a linear reconstruction such as $\phi = C_1 x_1 x_2 + C_2 x_1 + C_3 x_2 + C_4$ (two-dimensional) is acceptable. However, at high Reynolds numbers, linear reconstruction could lead to erroneous solutions. Majumdar et al. (2001) employed a higher order interpolant that is linear in the tangential direction and quadratic in the normal direction,

$$\phi = C_1 n^2 + C_2 nt + C_3 n + C_4 t + C_5, \tag{1.12}$$

where n and t are normal and tangent unit coordinates, respectively. Then the value of the flow variable at the ghost cell point ϕ_G can be expressed as

$$\phi_G = \sum^{i} \omega_i \phi_i, \tag{1.13}$$

where the summation extends over all the points in the stencil and ω_i are known geometry dependent coefficients.

1.3.2.6 Other methods

Recently, Su et al. (2007) combined the original immersed boundary method with the direct forcing method in order to overcome the time step limitation. This method also employs a mixture of Eulerian and Lagrangian variables, where the solid boundary is represented by discrete Lagrangian markers and exerts forces on the Eulerian fluid domain.

Finally, there are other categories of numerical methods to handle flow problems with immersed interfaces, such as the volume of fluid (VOF) approach and the level-set method. Typically, the former method was developed for the tracking of interfaces between different fluids (i.e., free surface flows) and the latter was used for the flame propogation problems in combustion modeling. These techniques might be adapted or combined with the immersed boundary method to deal with flow problems with immersed solid bodies.

1.3.2.7 Special treatment of boundary treatment for moving boundary problems

For moving boundary problems, the boundary determination and forcing calculation procedure introduces further complexity compared to stationary boundary problems. In cut-cell or direct forcing formulations, complications are encountered due to the fact that the Eulerian grid points near the interface changes from timestep to timestep, as the body moves through the fixed grid. As a result, the velocity and pressure for some points in the flow will assume non-physical values due to their previous association with the solid phase. In the case of "ghost cell" methods, as the body moves through the fixed grid some of the ghost cells will move into

the fluid and become fluid cells. Since they were previously in the solid they have no valid history in the fluid phase and no physically realizable values for the velocity and pressure. In the case where the solution is reconstructed at the fluid nodes closest to the boundary, the points that emerge from the solid become the boundary points that are central to the reconstruction procedure and therefore their history in the fluid phase is irrelevant. One approach suggested by Udaykumar et al. (1999) is to merge these cells with adjacent fluid cells for the first time step after a cell emerges from the body. Another one is to determine the flow velocity in this cell for each time step by interpolating from neighboring cells (Udaykumar et al., 2001). Yang and Balaras (2006) employed a method similar to the latter one and obtained very promising results. The issue of cell refreshing is not encountered in the immersed boundary method using continuous forcing since the force distribution has been spread on both sides of the boundary This removes the temporal discontinuity for cells merging into the fluid.

1.3.2.8 Other applications of the immersed boundary method

Pan et al. (2002) applied the IB methed to simulate the dynamics of premixed flames. Vitturi et al. (2007) used the immersed boundary method to simulate the dynamics of pyroclastic density currents, where the extension of the IB method to compressible multiphase flows is achieved through a flux correction term in the mass continuity equations of the immersed cells that accounts for density variations in the partial volumes.

1.3.3 Particle laden turbulent flow simulation

Transport of small particles in turbulent fluid flow occurs in many industrial processes such as aerosol transport and deposition, spray combustion and fluidized bed combustion. The developement of more accurate LES models such as dynamic modeling (Germano et al., 1991), approximate deconvolution models (Stolz et al., 2001) and variational multiscale model (Hughes et al., 2001; Vreman, 2003), provides the possibility to simulate particle-laden turbulent flows accurately with LES. However, due to the interaction between particles and turbulent eddies, new terms appear in the governing equations of the fluid and particle phases

that need to be modeled. Basically, the following effects need to be considered: (i) effects of subgrid scale fluctuations on the particle dispersion; (ii) effects of particles on the subgrid scales statistical propertities; (iii) effects of particles on the filtered scale fields; (iv) inter-particle collisions. Since the filtered fluid field can be solved directly, the new terms that need to be modeled often depend on the interaction of particles and subgrid scale eddies. When the particle relaxation time is large compared to the Kolmogrov time scale and the smallest time scale resolved in the LES, the disregard of the subgrid scale effect is justified (Uijttwaal and Oliemans, 1996; Armenio et al., 1999). In contrast, when the particle relaxation time is the same order as the Kolmogrov time, a substantial difference between the DNS and LES results remains (Kuerten, 2006), which indicates the neglect of subgrid scale effects can cause significant errors. In the literature, the subgrid scale field (Pozorski et al., 2004; Oesterle and Zaichik, 2004) and the particle dispersion (Pai and Subramaniam, 2007) are often modeled with a stochastic process governed by Langevin equations. In these models, an appropriate Lagrangian correlation time scale is necessary to prescribe the parameters of drift and diffusion coefficients.

Although there are various analytical and numerical methods for predicting turbulent flows laden with solid particles or liquid droplets, Mashayek and Pandya (2003) separated these methods into two major categories. The first category is refered to as the Lagrangian approach, which describes the motion of particles with a Lagrangian coordinates. Depending on the method used to simulate turbulent flows, it includes direct numerical simulation (DNS), large-eddy simulation (LES) and stochastic modeling. The second category is the Eulerian approach that treats the continuous and dispersed phases with an Eulerian approach and it includes Reynolds averaged Navier-Stokes (RANS) and probability density function (pdf) modeling. The mean field theory describes each phase with jump conditions formulated across interphase boundaries (Drew and Passman, 1999). The solution of these equations typically relies on an averaging procedure of some kind, e.g. time, space or ensemble. In this approach, phase-filtered equations can be formed based on spatial filtering with LES techniques. However, it was reported that one disadvantage of a phase-averaged approach is that moment closures

can not adequately capture the effects of physics at the small scales (Carrara and DesJardin, 2003). Carrara and DesJardin (2003) combined LES with a filtered density function (FDF) approach and they provided a new definition of the instantaneous interfacial area concentration to simplify phase-coupling terms. In their work, the full velocity-scalar FDF transport equation for a separated two-phase flow was derived in the context of LES filtering and they showed that the instantaneous form of the transport equations in the FDF formulation can be recovered directly from the phase- filtered field by shrinking the LES filter volume. They also showed that conditionally surface-filtered quantities arising in the two-phase FDF formulation are equal to phase-coupling terms in the phase-filtered LES equations. Under Lagrangian descriptions, since Wang and Squires (1996) performed a one-way couple LES of particle-laden turbulent channel flow, a significant amount of work was developed to study the two-way coulping effects and the influence of subgrid scale flutuaions on particles recently. Yuu et al. (2001) studied a particle-laden jet flow by taking consideration of the effect of particle existence on the subgrid-scale flow. A drag interaction term was included in the momentum equation and in their model for subgrid stress terms, the subgrid eddy viscosity ν_t is assumed to depend on subgrid kinetic energy k_{sgs}. A transport equation for k_{sgs} is formed and the interphase transfer terms are modeled through a gradient transport method.

Sankaran and Menon (2002) also solved a transport equation for subgrid kinetic energy k_{sgs} and the subgrid eddy viscosity was formed to be related to k_{sgs} and a model spectrum. Moreover, they considered the effect of turbulence on the droplet motion using the stochastic separated flow model, in which the subgrid velocity was modeled with subgrid kinetic energy and a random number sampled from a uniform distribution. Winkler et al. (2006) applied a similar approach to simulate the particle wall-deposition in a turbulent square duct flow and they observed that the deposition rate increased with the consideration of two-way coupling and collision. Vinkovic et al. (2006) simulated a droplet dispersion for inhomogeneous turbulent wall flow with LES. In their work, a three-dimensional Langevin equation was used to model the subgrid velocity and an appropriate Lagrangian correlation timescale was considered in order to include the influence of gravity and inertia. Yamamoto et al. (2001) simulated a

turbulent gas-particle flow in a vertical channel by considering inter-particle collisions. They claimed that the calculated turbulence attenuation by particles agreed well with experimental measurements for small Stokes number particles, but not for large Stokes number particles. By considering inter-particle collision the shape and scale of particle clouds observed in the channel-center region agreed well with experimental observation, unlike the LES results by Wang and Squires (1996). Nevertheless, in the above LES simulation of particle-laden flows, the importance of multiscale interaction between particles and turbulent eddies with a series of time and length scales is not fully addressed.

1.4 Dissertation Organization

The following chapters of this dissertation will be organized in this manner:

Chapter 2 describes the governing equations, the filtering procedure, the sub-grid scale (SGS) models and the finite volume formulations which were used in the current large eddy simulations (LES). This chapter highlights the different SGS models and boundary conditions. The details of the process of incorporating the immersed boundary method into the eddy viscosity type LES solver will be presented in Chapter 3. The validation of the current solver for laminar flow and turbulent flow simulations with different Reynolds numbers is demostrated in Chapter 4. The simulation results for a duct containing one cylindrical rod are also reported. Chapter 5 demonstrates the capability of the current solver in simulating laminar and turbulent flow with heat transfer. Chapter 6 reports the simulation results of more complex geometry cases. The transonic and supersonic flows over a circular cylinder are considered. Then turbulent subchannel flow in a duct surrounding two cylindrical rods is discussed. Chapter 7 shows the DNS simulation results of particle laden isotropic flows and the multi-timescale consideration between the dispersed phase and turbulent eddies. The conclusions of this research, as well as recommendations for future work can be found in Chapter 8.

CHAPTER 2. GOVERNING EQUATIONS AND NUMERICAL SCHEMES

The compressible filtered Navier-Stokes equations and large eddy simulation (LES) formation are presented in this chapter. The sub-grid scale models required to close the equations are described. The finite volume formulation and numerical schemes used to solve the equation are also discussed in this chapter.

2.1 Governing Equations

The compressible Navier-Stokes equations are based on the conservation equations of mass, momentum and energy.

$$\frac{\partial \rho^*}{\partial t^*} + \frac{\partial (\rho^* u_j^*)}{\partial x_j^*} = 0 \tag{2.1}$$

$$\frac{\partial (\rho^* u_i^*)}{\partial t^*} + \frac{\partial (\rho^* u_i^* u_j^*)}{\partial x_j^*} = \frac{\partial \sigma_{ij}^*}{\partial x_j^*} + S_i^* \tag{2.2}$$

$$\frac{\partial (\rho^* E^*)}{\partial t^*} + \frac{\partial (\rho^* E^* u_j^*)}{\partial x_j^*} = -\frac{\partial q_j^*}{\partial x_j^*} + \frac{\partial (\sigma_{ij}^* u_i^*)}{\partial x_j^*} + S_E^*, \tag{2.3}$$

where E^* is the total specific energy, which is the sum of the specific internal energy and the specific kinetic energy: $E^* = e^* + \frac{1}{2} u_j^* u_j^*$. The stress tensor is given as

$$\sigma_{ij}^* = -p^* \delta_{ij} + 2\mu^* (S_{ij}^* - \frac{1}{3} S_{kk}^* \delta_{ij}), \tag{2.4}$$

where δ is the Kronecker delta and S_{ij}^* is the strain rate tensor

$$S_{ij}^* = \frac{1}{2} (\frac{\partial u_i^*}{\partial x_j^*} + \frac{\partial u_j^*}{\partial x_i^*}). \tag{2.5}$$

The heat flux q_i^* is determined by Fourier's law:

$$q_i^* = -k^* \frac{\partial T^*}{\partial x_i^*}. \tag{2.6}$$

The source term S_i^*, S_E^* is 0 if there is no external force fields, otherwise it will contain the force terms such as in mixed convection or rotating flow simulations. In LES and DNS, it is very common to apply periodic boundary conditions to some dimensions of the computational domain. If such a boundary condition is used in the flow direction, a forcing function equivalent to the mean pressure force has to be employed in the source term to drive the flow.

The ideal gas model is used to close the above equations since air is the working fluid in the current study. The equation of state for the ideal gas model is

$$p^* = \rho^* R^* T^*, \tag{2.7}$$

where R^* is the gas constant. And for an ideal gas the specific internal energy is $e^* = c_v^* T^*$. The properties μ^* and k^* are the molecular dynamic viscosity and thermal conductivity, respectively. Both of them are functions of temperature that can be derived from molecular dynamics theory. In this study, the Sutherland's power law (Schlichting, 1979) was used to evaluate μ^* and k^*,

$$\frac{\mu^*}{\mu_{ref}} = \left(\frac{T^*}{T_{ref}}\right)^n, \quad \frac{k^*}{k_{ref}} = \left(\frac{T^*}{T_{ref}}\right)^n, \tag{2.8}$$

where $n = 0.71$.

The governing dimensional equations can be non-dimensionalized with respect to appropriate dimensional reference quantities as described below

$$\begin{array}{lll} x_i = \frac{x_i^*}{L_{ref}} & t = \frac{t^*}{L_{ref}/U_{ref}} & u_i = \frac{u_i^*}{U_{ref}} \\ p = \frac{p^*}{\rho_{ref} U_{ref}^2} & \rho = \frac{\rho^*}{\rho_{ref}} & T = \frac{T^*}{T_{ref}} \\ e = \frac{e^*}{U_{ref}^2} & \mu = \frac{\mu^*}{\mu_{ref}} & k = \frac{k^*}{k_{ref}} \\ c_v = \frac{c_v^*}{U_{ref}^2/T_{ref}} & c_p = \frac{c_p^*}{U_{ref}^2/T_{ref}} & R = \frac{R^*}{U_{ref}^2/T_{ref}}. \end{array} \tag{2.9}$$

In this research, the hydraulic diameter is chosen as the reference length L_{ref}. U_{ref}, T_{ref}, ρ_{ref} are the mean or freestream values and μ_{ref} and k_{ref} are the values of corresponding properties at T_{ref}.

Using the above definitions, the non-dimensional form of the governing equations is

$$\frac{\partial \rho}{\partial t} + \frac{\partial (\rho u_j)}{\partial x_j} = 0 \tag{2.10}$$

$$\frac{\partial \rho u_i}{\partial t} + \frac{\partial (\rho u_i u_j)}{\partial x_j} = \frac{\partial \sigma_{ij}}{\partial x_j} + S_i \tag{2.11}$$

$$\frac{\partial (\rho E)}{\partial t} + \frac{\partial (\rho E u_j)}{\partial x_j} = -\frac{\partial q_j}{\partial x_j} + \frac{\partial (\sigma_{ij} u_i)}{\partial x_j} + S_E. \tag{2.12}$$

The non-dimensional stress tensor, strain rate tensor and heat flux vector are

$$\begin{aligned} \sigma_{ij} &= -p\delta_{ij} + \frac{2\mu}{Re}(S_{ij} - \frac{1}{3}S_{kk}\delta_{ij}), \\ S_{ij} &= \frac{1}{2}(\frac{\partial u_i}{\partial x_j} + \frac{\partial u_j}{\partial x_i}), \\ q_i &= -\frac{c_p \mu}{PrRe}\frac{\partial T}{\partial x_i}. \end{aligned} \tag{2.13}$$

Re is the Reynolds number and Pr is the Prandtl number. Their definitions are

$$Re = \frac{\rho_{ref} U_{ref} L_{ref}}{\mu_{ref}}, \quad Pr = \frac{\mu^* c_p^*}{k^*}. \tag{2.14}$$

2.2 Filtering

In large eddy simulation, only the large scales are resolved and small scales are modeled. To separate the effects of the large-scale and small scale motions, a filtering operation should be applied to the Navier-Stokes equations. The filtering operation is defined as

$$\bar{f}(\mathbf{x}, t) = \int G(|\mathbf{r}|\,; \Delta) f(\mathbf{x} - \mathbf{r}, t) d\mathbf{r}, \tag{2.15}$$

where integration is over the entire flow domain, and the specified filter function G satisfies the normalization condition

$$\int G(|\mathbf{r}|\,; \Delta) d\mathbf{r} = 1. \tag{2.16}$$

In Fourier space, the most commonly used filters for LES are the spectral cut-off filter, Gaussian filter and top hat filter. The spectral cut-off filter can be easily applied in Fourier space but is not easily defined in physical space. The Gaussian filter is preferred by some researchers as it approximates the cut-off filter and has similar performance in both wavenumber space and physical space (Dailey, 1997). In the present study, the top-hat filter is used, which is defined as

$$G(|\mathbf{r}|; \Delta) = \begin{cases} 1/\Delta & \text{if } |\mathbf{r}| \le \Delta/2 \\ 0 & \text{if } |\mathbf{r}| > \Delta/2, \end{cases} \tag{2.17}$$

where Δ is the filter width. This filter is a very natural choice when finite-volume or finite-difference methods are used because by setting Δ the same as the grid resolution this filtering process reduces to an average over a control volume. In the present research, an anisotropic rectangular grid with grid spacings Δ_1, Δ_2, and Δ_3 in the three coordinate directions was used in most of the cases; then the filter width Δ was taken to be $\Delta = (\Delta_1\Delta_2\Delta_3)^{1/3}$ as suggested by Deardorff (1970).

As a result of the filtering operation, the flow field can be viewed as being decomposed into two components:

$$f = \bar{f} + f', \tag{2.18}$$

where $\bar{f}$ is the resolved scale and f' is the small subgrid scale component. The difference of the above decompostion from Reynolds decomposition is that LES uses a spatial average rather than a temporal average in the filtering procedure. As a result, the filtering operation and differentiating with respect to time commute, i.e.,

$$\frac{\partial \bar{f}}{\partial t} = \overline{\frac{\partial f}{\partial t}}. \tag{2.19}$$

However, the filtering operation and differentiation with respect to position do not commute in general unless the filter width is constant, and the commutation error is second order in filter width (Ghosal and Moin, 1995). To avoid this difficulty, one can filter only in the homogeneous directions. If the filtering operation is applied to the nondimensional governing equations Eq. (2.10), terms like $\overline{\rho u_i}$, $\overline{\rho u_i u_j}$ and $\overline{\rho u_i T}$ appear. To simplify the equations, Favre filtering (Favre, 1983) is introduced to give

$$\tilde{f} = \frac{\overline{\rho f}}{\bar{\rho}}. \tag{2.20}$$

Thus, the variables can be decomposed in another way,

$$f = \tilde{f} + f'', \tag{2.21}$$

where $\tilde{f}$ is the resolved component and f'' is the unresolved component. Using Favre filtering, we have

$$\overline{\rho u_i} = \bar{\rho}\tilde{u}_i; \quad \overline{\rho u_i u_j} = \bar{\rho}\widetilde{u_i u_j}; \quad \overline{\rho u_i T} = \bar{\rho}\widetilde{u_i T}. \tag{2.22}$$

The Favre filtered continuity and momentum equations can be easily derived (assuming the source term $S_i, S_E = 0$):

$$\begin{aligned} \frac{\partial \bar{\rho}}{\partial t} + \frac{\partial (\bar{\rho}\tilde{u}_j)}{\partial x_j} &= 0, \\ \frac{\partial (\bar{\rho}\tilde{u}_i)}{\partial t} + \frac{\partial (\bar{\rho}\tilde{u}_i\tilde{u}_j)}{\partial x_j} &= \frac{\partial \bar{\sigma}_{ij}}{\partial x_j} - \frac{\partial \tau_{ij}}{\partial x_j}, \end{aligned} \tag{2.23}$$

in which

$$\begin{aligned} \bar{\sigma}_{ij} &= \overline{-p\delta_{ij} + \frac{2\mu}{Re}(S_{ij} - \frac{1}{3}S_{kk}\delta_{ij})} = -\bar{p}\delta_{ij} + \overline{\frac{2\mu}{Re}(S_{ij} - \frac{1}{3}S_{kk}\delta_{ij})} \\ &\approx \hat{\sigma}_{ij} = -\bar{p}\delta_{ij} + \frac{2\bar{\mu}}{Re}(\tilde{S}_{ij} - \frac{1}{3}\tilde{S}_{kk}\delta_{ij}), \\ \tau_{ij} &= \bar{\rho}(\widetilde{u_i u_j} - \tilde{u}_i\tilde{u}_j). \end{aligned} \tag{2.24}$$

The approximation made in Eq. (2.24) is due to the weak correlation between μ and derivatives of velocity (Cebeci and Smith, 1974) Compared with the original momentum equations, the filtered form has one more term associated with the so-called subgrid scale (SGS) stress tensor τ_{ij} which represents the effect of the small-scale motions. The strain rate tensor is

$$\tilde{S}_{ij} = \frac{1}{2}(\frac{\partial \tilde{u}_i}{\partial x_j} + \frac{\partial \tilde{u}_j}{\partial x_i}). \tag{2.25}$$

The derivation of the filtered equation for conservation of total energy is derived following the work of Vreman et al. (1995). An alternate form of the energy equation is used by removing the mechanical energy from the total energy,

$$\frac{\partial (\rho c_v T)}{\partial t} + \frac{\partial (\rho c_v T u_j)}{\partial x_j} = \sigma_{ij}\frac{\partial u_i}{\partial x_j} - \frac{\partial q_j}{\partial x_j}. \tag{2.26}$$

Applying the filtering operation to the above equation leads to

$$\frac{\partial (\bar{\rho} c_v \tilde{T})}{\partial t} + \frac{\partial (\bar{\rho} c_v \tilde{T}\tilde{u}_j)}{\partial x_j} = \overline{\sigma_{ij}\frac{\partial u_i}{\partial x_j}} - \frac{\partial \bar{q}_j}{\partial x_j} - \frac{\partial Q_{tj}}{\partial x_j}, \tag{2.27}$$

in which $Q_{tj} = \bar{\rho} c_v(\widetilde{Tu_j} - \tilde{T}\tilde{u}_j)$ is the SGS heat flux. Notice the specific heat c_v is regarded as a constant since the ideal gas model is used. The filtered heat flux $\bar{q}_j$ can be approximated as

$$\bar{q}_j = -\overline{\frac{c_p \mu}{PrRe}\frac{\partial T}{\partial x_j}} \approx \hat{q}_j = -\frac{c_p \bar{\mu}}{PrRe}\frac{\partial \tilde{T}}{\partial x_j} \tag{2.28}$$

by assuming the correlation between viscosity and temperature derivative is weak. To obtain the equation for $\bar{\rho}\hat{E}$, the Favre filtered momentum equation is expanded as,

$$\bar{\rho}\frac{\partial \tilde{u}_i}{\partial t} + \tilde{u}_i\left[\frac{\partial \bar{\rho}}{\partial t} + \frac{\partial(\bar{\rho}\tilde{u}_j)}{\partial x_j}\right] + \bar{\rho}\tilde{u}_j\frac{\partial \tilde{u}_i}{\partial x_j} = \frac{\partial \bar{\sigma}_{ij}}{\partial x_j} - \frac{\partial \tau_{ij}}{\partial x_j}, \tag{2.29}$$

and the term inside the square brackets vanishes due to continuity. Multiplying Eq. (2.29) by $\tilde{u}_i$ and adding to the filtered internal energy equation, Eq. (2.27), gives

$$\begin{aligned}\frac{\partial(\bar{\rho}c_v\tilde{T})}{\partial t} &+ \frac{\partial(\bar{\rho}c_v\tilde{T}\tilde{u}_j)}{\partial x_j} + \bar{\rho}\frac{\partial(\frac{1}{2}\tilde{u}_i\tilde{u}_i)}{\partial t} + \bar{\rho}\tilde{u}_j\frac{\partial(\frac{1}{2}\tilde{u}_i\tilde{u}_i)}{\partial x_j} \\ &= \overline{\sigma_{ij}\frac{\partial u_i}{\partial x_j}} - \frac{\partial \bar{q}_j}{\partial x_j} - \frac{\partial Q_{tj}}{\partial x_j} + \tilde{u}_i\frac{\partial \bar{\sigma}_{ij}}{\partial x_j} - \tilde{u}_i\frac{\partial \tau_{ij}}{\partial x_j}.\end{aligned} \tag{2.30}$$

The filtered continuity equation, Eq. (2.23), is then multiplied by $\frac{1}{2}\tilde{u}_i\tilde{u}_i$ and added to Eq. (2.30) and results in

$$\begin{aligned}\frac{\partial(\bar{\rho}c_v\tilde{T})}{\partial t} &+ \bar{\rho}\frac{\partial(\frac{1}{2}\tilde{u}_i\tilde{u}_i)}{\partial t} + \frac{1}{2}\tilde{u}_i\tilde{u}_i\frac{\partial \bar{\rho}}{\partial t} + \frac{\partial(\bar{\rho}c_v\tilde{T}\tilde{u}_j)}{\partial x_j} + \bar{\rho}\tilde{u}_j\frac{\partial(\frac{1}{2}\tilde{u}_i\tilde{u}_i)}{\partial x_j} + \frac{1}{2}\tilde{u}_i\tilde{u}_i\frac{\partial(\bar{\rho}\tilde{u}_j)}{\partial x_j} \\ &= \overline{\sigma_{ij}\frac{\partial u_i}{\partial x_j}} - \frac{\partial \bar{q}_j}{\partial x_j} - \frac{\partial Q_{tj}}{\partial x_j} + \tilde{u}_i\frac{\partial \bar{\sigma}_{ij}}{\partial x_j} - \tilde{u}_i\frac{\partial \tau_{ij}}{\partial x_j}.\end{aligned} \tag{2.31}$$

The first three terms and last three terms on the left hand side of Eq. (2.31) are combined, giving

$$\frac{\partial(\bar{\rho}\hat{E})}{\partial t} + \frac{\partial(\bar{\rho}\hat{E}\tilde{u}_j)}{\partial x_j} = \overline{\sigma_{ij}\frac{\partial u_i}{\partial x_j}} - \frac{\partial \hat{q}_j}{\partial x_j} - \frac{\partial Q_{tj}}{\partial x_j} + \tilde{u}_i\frac{\partial \hat{\sigma}_{ij}}{\partial x_j} - \tilde{u}_i\frac{\partial \tau_{ij}}{\partial x_j}, \tag{2.32}$$

where $\hat{E} = \tilde{e} + \frac{1}{2}\tilde{u}_i\tilde{u}_i$ and $\bar{\sigma}_{ij}$ and $\bar{q}_j$ are replaced by their approximations $\hat{\sigma}_{ij}$ and $\hat{q}_j$ respectively. After combining the pressure term into the energy term, this equation can be rewritten as

$$\frac{\partial(\bar{\rho}\hat{E})}{\partial t} + \frac{\partial[(\bar{\rho}\hat{E} + \bar{p})\tilde{u}_j]}{\partial x_j} = \frac{\partial(\tilde{u}_i\hat{\sigma}_{a,ij})}{\partial x_j} - \frac{\partial \hat{q}_j}{\partial x_j} - \frac{\partial Q_{tj}}{\partial x_j} - \alpha - \pi - \epsilon, \tag{2.33}$$

where α is the turbulent stress on the scalar level, π is the pressure-dilatation term and ϵ is the subgrid scale turbulent dissipation rate. They are given as

$$\begin{aligned}\alpha &= \tilde{u}_i\frac{\partial \tau_{ij}}{\partial x_j}; \\ \pi &= \overline{p\frac{\partial u_j}{\partial x_j}} - \bar{p}\frac{\partial \tilde{u}_j}{\partial x_j} \\ \epsilon &= \overline{\sigma_{a,ij}\frac{\partial u_i}{\partial x_j}} - \hat{\sigma}_{a,ij}\frac{\partial \tilde{u}_i}{\partial x_j},\end{aligned}$$

where $\sigma_{a,ij}$ is the anisotropic component of the stress. For the present work, α, π and ϵ are neglected when Mach number is less than 0.2 (Vreman et al., 1995).

2.3 Subgrid Scale Model

The role of SGS models in LES is analogous to the turbulence models for the Reynolds averaged Navier-Stokes (RANS) equations. The advantage for LES is that the simulation should be much less sensitive to the modeling method, because in LES only the small scales are modeled that are mostly isotropic. While in RANS modeling, a wide range of scales and anisotropy must be modeled. The commonly used SGS models can be separated into the eddy viscosity type models and non-eddy viscosity dependent models. The former includes the Smagorinsky SGS model, the dynamic SGS model, the structure function model and the one-equation SGS model. The latter includes the scale similarity model.

Generally, the SGS stress tensor τ_{ij} can be decomposed into two parts, the anisotropic part and the isotropic part as

$$\tau_{ij} = \bar{\rho}(\widetilde{u_i u_j} - \tilde{u}_i \tilde{u}_j) = \tau_{ij}^a + \frac{1}{3}\tau_{kk}\delta_{ij}. \tag{2.34}$$

The eddy viscosity based methodology assumes the anisotropic part of the SGS stress tensor to be proportional to the filtered rate of strain:

$$\tau_{ij}^a = -2\mu_t(\tilde{S}_{ij} - \frac{1}{3}\tilde{S}_{kk}\delta_{ij}). \tag{2.35}$$

The filtered strain rate tensor is

$$\tilde{S}_{ij} = \frac{1}{2}(\frac{\partial \tilde{u}_i}{\partial x_j} + \frac{\partial \tilde{u}_j}{\partial x_i}), \tag{2.36}$$

and $\tilde{S}_{kk}$ is the isotropic component. The isotropic part τ_{kk} is negligible compared to the thermodynamic pressure as Moin et al. (1991) and Spyropoulos and Blaisdell (1995) indicated. Vreman et al. (1995) and Dailey (1997) observed that the calculation was unstable if the isotropic part was not neglected. In the present work, τ_{kk} is neglected.

2.3.1 Smagorinsky Model

The Smagorinsky model was derived by imposing equilibrium between the energy transfer from large-to-small scale structures and energy dissipation by the small scale motion (Dailey,

1997). By analogy to the Prandtl's mixing-length hypothesis, the eddy viscosity is modeled as

$$\mu_t = \bar{\rho}\mathcal{L}_s^2|\tilde{\mathcal{S}}| = \bar{\rho}C_s\Delta^2|\tilde{\mathcal{S}}|, \tag{2.37}$$

where $\mathcal{L}_s$ is the Smagorinsky length scale and C_s is the Smagorinsky coefficient which is a positive constant in this model. The magnitude of the filtered strain rate tensor is defined as

$$\tilde{\mathcal{S}} = (2\tilde{S}_{ij}\tilde{S}_{ij})^{1/2}. \tag{2.38}$$

The major shortcoming of this model is that the Smagorinsky coefficient should in fact depend on factors like flow regimes, distance to the walls and grid scales rather than being a constant. For example, in laminar flow or close to a solid wall, this coefficient should be zero. Although it is possible to modify the Smagorinsky coefficient formula to take these factors into account, the coefficient is usually problem dependent and it is difficult to generalize to other problems. Higher order models include solving individual transport equations for subgrid kinetic energy or each of the subgrid stresses, similar to the one-equation model and Reynolds stress model in RANS modeling, respectively. These models generally involve a series of empirical constants which usually work well for specific problems. On the other hand, the dynamic model calculates Smagorinsky coefficient dynamically without any *a priori* parameters.

2.3.2 Dynamic Smagorinsky Model

Germano et al. (1991) developed a dynamic model by introducing a dynamically calculated coefficient C_s as a function of space and time. The coefficient can be negative so as to account for the backscatter of energy from small scales to large scales. The SGS stresses obtained from this model vanish in laminar flow and at solid boundaries, and have the correct asymtotic behavior in the near wall region. The dynamic model proposed by Moin et al. (1991) and Lilly (1992) not only consider the variable eddy viscosity but allows the eddy thermal diffusivity to be calculated dynamically. The basic idea of dynamic model is to introduce a test filter with a larger filter width $\hat{\Delta}$ than the resolved grid filter width. The test filter width $\hat{\Delta}$ is defined in the same way as the grid filter width.

The subgrid stresses based on the grid filter and test filter scales are defined, respectively, as

$$\begin{aligned}\tau_{ij} &= \bar{\rho}\widetilde{u_i u_j} - \bar{\rho}\tilde{u}_i\tilde{u}_j = \overline{\rho u_i u_j} - \frac{\overline{\rho u_i}\,\overline{\rho u_j}}{\bar{\rho}};\\ T_{ij} &= \widehat{\overline{\rho u_i u_j}} - \frac{\widehat{\overline{\rho u_i}}\,\widehat{\overline{\rho u_j}}}{\hat{\bar{\rho}}} = \widehat{\bar{\rho}\widetilde{u_i u_j}} - \frac{\widehat{\bar{\rho}\tilde{u}_i}\widehat{\bar{\rho}\tilde{u}_j}}{\hat{\bar{\rho}}}.\end{aligned} \tag{2.39}$$

According to the Smagorinsky model, the anisotropic part of the SGS stress is determined by

$$\begin{aligned}\tau^a_{ij} &= \tau_{ij} - \frac{1}{3}\tau_{kk}\delta_{ij} = -2\mu_t(\tilde{S}_{ij} - \frac{1}{3}\tilde{S}_{kk}\delta_{ij})\\ &= -2\bar{\rho}C_s\Delta^2\tilde{\mathcal{S}}(\tilde{S}_{ij} - \frac{1}{3}\tilde{S}_{kk}\delta_{ij}) = C_s\alpha_{ij}.\end{aligned} \tag{2.40}$$

Similarly, the subgrid stress based on test filter scale is modeled as

$$\begin{aligned}T^a_{ij} &= T_{ij} - \frac{1}{3}T_{kk}\delta_{ij} = -2\hat{\mu}_t(\hat{\tilde{S}}_{ij} - \frac{1}{3}\hat{\tilde{S}}_{kk}\delta_{ij})\\ &= -2\hat{\bar{\rho}}C_s\hat{\Delta}^2\hat{\tilde{\mathcal{S}}}(\hat{\tilde{S}}_{ij} - \frac{1}{3}\hat{\tilde{S}}_{kk}\delta_{ij}) = C_s\beta_{ij},\end{aligned} \tag{2.41}$$

where

$$\hat{\tilde{S}}_{ij} = \frac{1}{2}(\frac{\partial\hat{\tilde{u}}_i}{\partial x_j} + \frac{\partial\hat{\tilde{u}}_j}{\partial x_i}). \tag{2.42}$$

An identity introduced by Germano (1992) is obtained by

$$\mathbf{L}_{ij} = T_{ij} - \hat{\tau}_{ij} = \widehat{\bar{\rho}\tilde{u}_i\tilde{u}_j} - \frac{\widehat{\bar{\rho}\tilde{u}_i}\widehat{\bar{\rho}\tilde{u}_j}}{\hat{\bar{\rho}}}. \tag{2.43}$$

Thus, we have

$$\mathbf{L}^a_{ij} = \mathbf{L}_{ij} - \frac{1}{3}\mathbf{L}_{kk}\delta_{ij} = C_s\beta_{ij} - \widehat{C_s\alpha_{ij}} \approx C_s(\beta_{ij} - \hat{\alpha}_{ij}). \tag{2.44}$$

As both $\mathbf{L}^a_{ij}$ and $\beta_{ij} - \hat{\alpha}_{ij}$ are known in terms of $\tilde{u}_i$ and $\tilde{u}_j$, the value of C_s can be determined from the above equation. Using the least square approach (Lilly, 1992), the sum of the squares of the error can be minimized by contracting both sides of Eq. (2.44) with $\beta_{ij} - \hat{\alpha}_{ij}$ to yield:

$$C_s = \frac{\left\langle \mathbf{L}^a_{ij}(\beta_{ij} - \hat{\alpha}_{ij})\right\rangle}{\langle(\beta_{mn} - \hat{\alpha}_{mn})(\beta_{mn} - \hat{\alpha}_{mn})\rangle}, \tag{2.45}$$

where $\langle\cdot\rangle$ denotes a spatial averaging procedure along the homogeneous directions of the flow. Such a procedure is necessary to ensure the stability of LES calculations.

The SGS heat flux vectors Q_{tj}, Q_j based on the grid filter and the test filter scales are defined following

$$\begin{aligned} Q_{tj} &= c_v(\widetilde{\bar{\rho}\tilde{T}\tilde{u}_j} - \bar{\rho}\tilde{T}\tilde{u}_j) = c_v(\overline{\rho T u_j} - \frac{\overline{\rho T}\,\overline{\rho u_j}}{\bar{\rho}}); \\ Q_j &= c_v(\widehat{\overline{\rho T u_j}} - \frac{\widehat{\overline{\rho T}}\,\widehat{\overline{\rho u_j}}}{\hat{\bar{\rho}}}) = \widehat{\bar{\rho}\tilde{T}\tilde{u}_j} - \frac{\widehat{\bar{\rho}\tilde{T}}\,\widehat{\bar{\rho}\tilde{u}_j}}{\hat{\bar{\rho}}}. \end{aligned} \tag{2.46}$$

Then the heat fluxes are modeled as

$$\begin{aligned} Q_{tj} &= -\frac{c_v\mu_t}{Pr_t}\frac{\partial\tilde{T}}{\partial x_j} = \frac{\zeta_j}{Pr_t}; \\ Q_j &= -\frac{c_v\hat{\mu}_t}{Pr_t}\frac{\partial\hat{\tilde{T}}}{\partial x_j} = \frac{\eta_j}{Pr_t}, \end{aligned} \tag{2.47}$$

where Pr_t is the turbulent Prandtl number to be determined dynamically. μ_t and $\hat{\mu}_t$ are the same as those defined in Eqs. (2.40) and (2.41). The identity relating the two heat fluxes is

$$\mathbf{M}_j = Q_j - \hat{Q}_{tj} = c_v(\widehat{\bar{\rho}\tilde{T}\tilde{u}_j} - \frac{\widehat{\bar{\rho}\tilde{T}}\,\widehat{\bar{\rho}\tilde{u}_j}}{\hat{\bar{\rho}}}) = \frac{\eta_j - \hat{\zeta}_j}{Pr_t}. \tag{2.48}$$

Thus, we have

$$Pr_t = \frac{\left\langle(\eta_j - \hat{\zeta}_j)(\eta_j - \hat{\zeta}_j)\right\rangle}{\left\langle\mathbf{M}_n(\eta_n - \hat{\zeta}_n)\right\rangle}, \tag{2.49}$$

where $\langle\cdot\rangle$ still denotes a spatial averaging along the homogeneous directions of the flow. This dynamic model was successfully used by Wang and Pletcher (1996), Xu et al. (2004) and many other authors.

If there is no homogeneous direction in the flow field, the localized dynamic model developed by Ghosal et al. (1995) or Piomelli and Liu (1995) can be applied. Equation (2.44) is recast in the form

$$\mathbf{L}^a_{ij} = C_s\beta_{ij} - C^*_s\widehat{\alpha}_{ij}, \tag{2.50}$$

where C^*_s is an estimate of the coefficient. In the present research, the value at the previous time-step is used as C^*_s. The initial value of C_s is set to the Smagorinsky constant. Since C^*_s is known, C_s can be obtained by

$$C_s = \left\langle\frac{(\mathbf{L}^a_{ij} + C^*_s\widehat{\alpha}_{ij})\beta_{ij}}{\beta_{mn}\beta_{mn}}\right\rangle, \tag{2.51}$$

where $\langle\cdot\rangle$ is an averaging performed locally over the test filter volume. The turbulent Prandtl number is determined similarly:

$$Pr_t = \left\langle \frac{\eta_n \eta_n}{(\mathbf{M}_j + \zeta_j \widehat{/Pr_t^*})\eta_j} \right\rangle. \tag{2.52}$$

2.3.3 Structure Function Model (SFM)

Instead of modeling the subgrid scale eddy viscosity based on the filtered strain rate tensor, the eddy viscosity is expressed as a function of the SGS energy q_{SGS}^2,

$$\nu_T \sim \Delta(q_{SGS}^2(x))^{1/2} = C\Delta(F(\Delta x))^{1/2}, \tag{2.53}$$

where F is the second order structure function defined as

$$F(r) = \overline{||\mathbf{u}(\mathbf{x}) - \mathbf{u}(\mathbf{x}+\mathbf{r})||^2} \tag{2.54}$$

and it was hypothesized that the subgrid energy is proportional to the square of the velocity gradient at the smallest resolved scales,

$$q_{SGS}^2 = \frac{1}{2}\overline{(u_i(\mathbf{x},t) - \tilde{u}_i(\mathbf{x},t))^2} \sim F(r). \tag{2.55}$$

2.3.4 Scale Similarity Model

In the scale similarity model, it is assumed that the largest subgrid scales and the smallest resolved scales have a similar structure. Therefore,

$$\tau_{ij} = \bar{\rho}(\widetilde{u_i u_j} - \tilde{u}_i\tilde{u}_j) \sim \bar{\bar{\rho}}\widetilde{\tilde{u}_i\tilde{u}_j} - \bar{\bar{\rho}}\tilde{\tilde{u}}_i\tilde{\tilde{u}}_j. \tag{2.56}$$

The advantage of the scale similarity model compared to the Smagorinsky model is that it accounts for the energy transfer from small resolved scales to large resolved scales. Also the definition correlates well with a priori analysis. However, this model is not dissipative, i.e., it does not dissipate energy automatically as the Smagorinsky model.

2.4 Finite Volume Based Numerical Scheme

2.4.1 Integral Form of Equations

The nondimensional Favre filtered equations (2.23), (2.23) and (2.32) can be written in terms of primitive variables $\mathbf{W} = (\bar{p}, \tilde{u}_1, \tilde{u}_2, \tilde{u}_3, \tilde{T})^T$

$$\frac{\partial \mathbf{U}}{\partial \mathbf{W}} \frac{\partial \mathbf{W}}{\partial t} + \frac{\partial \mathbf{F}_i}{\partial x_i} = \mathbf{S}. \tag{2.57}$$

The use of primitive variables is advantageous because higher order construction and gradients are usually based on the primitive variables. By replacing density with pressure and temperature and then multiplying by the gas constant, the terms in the above equation become

$$\mathbf{U} = \begin{bmatrix} \bar{p}/\tilde{T} \\ \bar{p}\tilde{u}_1/\tilde{T} \\ \bar{p}\tilde{u}_2/\tilde{T} \\ \bar{p}\tilde{u}_3/\tilde{T} \\ \bar{p}\hat{E}/\tilde{T} \end{bmatrix}; \quad \mathbf{F}_i = \begin{bmatrix} \bar{p}\tilde{u}_i/\tilde{T} \\ \bar{p}\tilde{u}_i\tilde{u}_1/\tilde{T} - R\hat{\sigma}_{i1} + R\tau_{i1} \\ \bar{p}\tilde{u}_i\tilde{u}_2/\tilde{T} - R\hat{\sigma}_{i2} + R\tau_{i2} \\ \bar{p}\tilde{u}_i\tilde{u}_3/\tilde{T} - R\hat{\sigma}_{i3} + R\tau_{i3} \\ \bar{p}\tilde{u}_i\hat{H}/\tilde{T} - R\tilde{u}_j\hat{\sigma}_{a,ij} + R\hat{q}_i + RQ_{ti} \end{bmatrix}, \tag{2.58}$$

where

$$\begin{aligned} \hat{E} &= c_v\tilde{T} + \frac{1}{2}(\tilde{u}_k\tilde{u}_k); \\ \hat{\sigma}_{ij} &= -\bar{p}\delta_{ij} + \frac{2\bar{\mu}}{Re}(\tilde{S}_{ij} - \frac{1}{3}\tilde{S}_{kk}\delta_{ij}); \\ \tilde{S}_{ij} &= \frac{1}{2}(\frac{\partial \tilde{u}_i}{\partial x_j} + \frac{\partial \tilde{u}_j}{\partial x_i}); \\ \tau_{ij} &= -2\mu_t(\tilde{S}_{ij} - \frac{1}{3}\tilde{S}_{kk}\delta_{ij}); \\ \hat{q}_i &= -\frac{c_p\bar{\mu}}{PrRe}\frac{\partial \tilde{T}}{\partial x_i}; \\ Q_{ti} &= -\frac{c_v\mu_t}{Pr_t}\frac{\partial \tilde{T}}{\partial x_i}. \end{aligned} \tag{2.59}$$

The flux vector $\mathbf{F}_i$ is usually split into into three parts, the inviscid part $\mathbf{F}_{i,inv}$, the viscous part $\mathbf{F}_{i,vis}$ and the subgrid-scale part $\mathbf{F}_{i,sgs}$. They are defined as

$$\mathbf{F}_i = \mathbf{F}_{i,inv} - \mathbf{F}_{i,vis} + \mathbf{F}_{i,sgs}. \tag{2.60}$$

$$\mathbf{F}_{i,inv} = \begin{bmatrix} \bar{p}\tilde{u}_i/\tilde{T} \\ \bar{p}\tilde{u}_i\tilde{u}_1/\tilde{T} + R\bar{p}\delta_{i1} \\ \bar{p}\tilde{u}_i\tilde{u}_2/\tilde{T} + R\bar{p}\delta_{i2} \\ \bar{p}\tilde{u}_i\tilde{u}_3/\tilde{T} + R\bar{p}\delta_{i3} \\ \bar{p}\tilde{u}_i\hat{H}/\tilde{T} \end{bmatrix}; \quad \mathbf{F}_{i,vis} = \begin{bmatrix} 0 \\ R\hat{\sigma}_{a,i1} \\ R\hat{\sigma}_{a,i2} \\ R\hat{\sigma}_{a,i3} \\ R\tilde{u}_j\hat{\sigma}_{a,ij} - R\hat{q}_i \end{bmatrix}; \quad \mathbf{F}_{i,sgs} = \begin{bmatrix} 0 \\ R\tau_{i1} \\ R\tau_{i2} \\ R\tau_{i3} \\ RQ_{ti} \end{bmatrix}, \quad (2.61)$$

in which the stress tensor $\hat{\sigma}_{ij}$ is decomposed into the isotropic part $-\bar{p}\delta_{ij}$ and the anisotropic component $\hat{\sigma}_{a,ij} = \frac{2\bar{\mu}}{Re}(\tilde{S}_{ij} - \frac{1}{3}\tilde{S}_{kk}\delta_{ij})$. The contribution of pressure is included in the inviscid flux. And the specific total enthalpy $\hat{H}$ is

$$\hat{H} = \hat{E} + R\tilde{T} = c_p\tilde{T} + \frac{1}{2}(\tilde{u}_k\tilde{u}_k). \quad (2.62)$$

Eq. (2.57) can be integrated within a control volume Ω as

$$\int_\Omega [T]\frac{\partial \mathbf{W}}{\partial t}d\Omega + \oint_{\partial\Omega} \mathbf{F}_i\vec{e}_i \cdot d\vec{S} = \int_\Omega \mathbf{S}d\Omega, \quad (2.63)$$

where $[T] = \frac{\partial \mathbf{U}}{\partial \mathbf{W}}$ is the time derivative Jacobian matrix listed in Appendix A, $\partial\Omega$ is the bounding surface of the control volume Ω, $\vec{e}_i$ is the unit vector in the ith direction and $\vec{S}$ is the surface area vector. In the rest of the current study , the overmarks denoting the filtered variables such as $\overline{(\cdot)}$, $\tilde{(\cdot)}$, $\hat{(\cdot)}$ will be dropped for simplicity.

2.4.2 Finite Volume Method and Integral Approximation

The integral form of the governing equations are discretized and solved in a finite volume framework that has the advantage that it can be easily implemented in complex geometries. With the Cartesian coordinates system, the solution domain can be divided into rectangular control volumes (Fig. 2.1). The conserved equations and conservation principles are applied to each control volume and the solution variables are stored at the geometric centers of the control volumes. Every control volume has six surfaces that are labeled by numbers from one to six denoting the east, north, west, south, up and down surfaces correspondingly.

The volume integrals in Eq. (2.63) are then approximated using the mean value theorm as

$$\begin{aligned} \int_\Omega [T]\frac{\partial \mathbf{W}}{\partial t}d\Omega &\approx \left([T]\frac{\partial \mathbf{W}}{\partial t}\right)_{i,j,k}\Omega_{i,j,k}, \\ \int_\Omega \mathbf{S}d\Omega &\approx \mathbf{S}_{i,j,k}\Omega_{i,j,k}. \end{aligned} \quad (2.64)$$

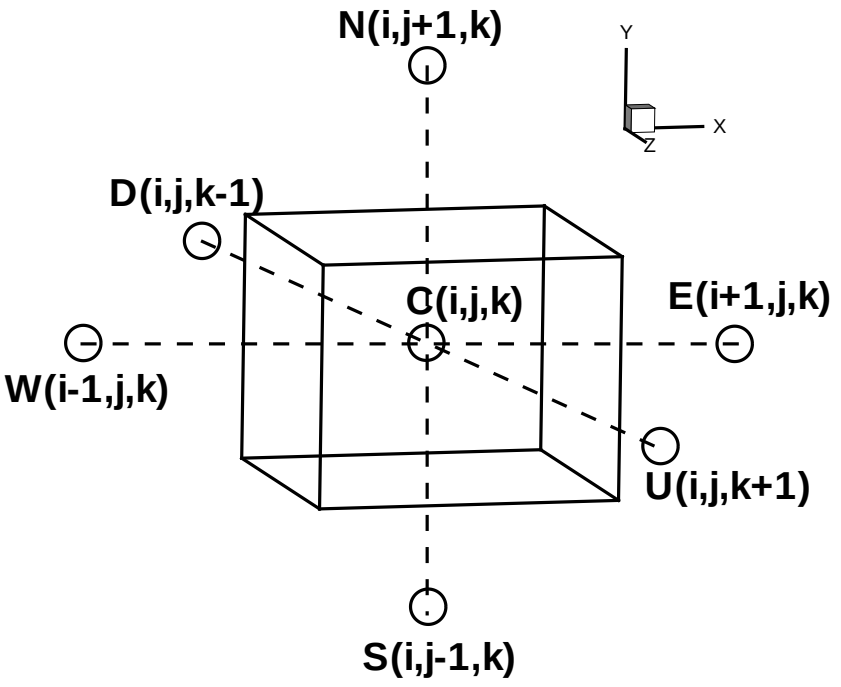

Figure 2.1 Main control volume (i,j,k) with its six neighboring control volumes.

The surface integral is approximated as

$$\oint_{\partial\Omega} \mathbf{F}_l \vec{e}_l \cdot d\vec{S} = \oint_{\partial\Omega} [\mathbf{F}_1 \vec{e}_1 + \mathbf{F}_2 \vec{e}_2 + \mathbf{F}_3 \vec{e}_3] \cdot d\vec{S} = \sum_{\beta=1}^{6} [(\mathbf{F}_1 \vec{e}_1 + \mathbf{F}_2 \vec{e}_2 + \mathbf{F}_3 \vec{e}_3) S]_\beta \approx \mathbf{C}(\mathbf{W}), \quad (2.65)$$

where S is the magnitude of the projected area of each surface onto a plane perpendicular to $(\vec{e}_1, \vec{e}_2, \vec{e}_3)$.

The inviscid flux vector on a surface between two control volumes, e.g., the east/west (E/W) surface between (i, j, k) and $(i + 1, j, k)$, is evaluated as

$$\mathbf{F}_{l1} = \mathbf{F}_l \left(\mathbf{W}_{i+1/2,j,k} \right), \quad (2.66)$$

where $\mathbf{W}_{i+1/2,j,k}$ is the value of solution variables on the E/W surface which can be obtained through interpolation between the two center values. To compute the viscous and subgrid-scale fluxes, the gradients of $\mathbf{W}$ at the control volume surfaces have to be calculated. With above

approximations, Eq. (2.63) becomes

$$[T]\frac{d\mathbf{W}}{dt}\Omega + \mathbf{C}(\mathbf{W}) = \mathbf{S}\Omega, \tag{2.67}$$

which is an algebraic equation and every function in it depends solely on $\mathbf{W}$ of the main control volume and its six neighboring volumes.

2.4.3 Gradients

The gradients of a scalar ϕ are calculated with the Gauss divergence theorem on an auxiliary control volume Ω' as

$$\int_{\Omega'} \nabla\phi d\Omega' = \int_{\partial\Omega'} \phi d\vec{S}'. \tag{2.68}$$

For the Cartesian coordinates, $\nabla\phi = \phi_1\vec{e}_1 + \phi_2\vec{e}_2 + \phi_3\vec{e}_3$, then the gradient can be approximated as

$$(\nabla\phi)\Omega' \approx \sum_{\beta'=1}^{6} \left(\phi\vec{S}'\right)_{\beta'}, \tag{2.69}$$

where β' denotes the six surfaces of the auxiliary control volume.

The auxiliary control volume is constructed such that its faces coincide with the volume centers of the two main control volumes whose interface stores the gradients. For example, the auxiliary control volume used to calculate the gradients on the east/west (E/W) faces of the main control volume (i, j, k) and $(i+1, j, k)$ is shown in Fig. 2.2. Therefore the volume of the auxiliary control volume is given by

$$\Omega' = \frac{1}{2}(\Omega_{i,j,k} + \Omega_{i+1,j,k}). \tag{2.70}$$

The solution variables on the auxiliary control surface can be evaluated as

$$\phi_{E'} = \phi_{i+1,j,k} \tag{2.71}$$

$$\phi_{W'} = \phi_{i,j,k} \tag{2.72}$$

$$\phi_{N'} = \frac{1}{2}\left[\alpha_y^+\phi_{i+1,j+1,k} + (1-\alpha_y^+)\phi_{i+1,j,k}\right] + \frac{1}{2}\left[\alpha_y^+\phi_{i,j+1,k} + (1-\alpha_y^+)\phi_{i,j,k}\right] \tag{2.73}$$

$$\phi_{S'} = \frac{1}{2}\left[\alpha_y^-\phi_{i+1,j-1,k} + (1-\alpha_y^-)\phi_{i+1,j,k}\right] + \frac{1}{2}\left[\alpha_y^-\phi_{i,j-1,k} + (1-\alpha_y^-)\phi_{i,j,k}\right] \tag{2.74}$$

$$\phi_{U'} = \frac{1}{2}\left[\alpha_z^+\phi_{i+1,j,k+1} + (1-\alpha_z^+)\phi_{i+1,j,k}\right] + \frac{1}{2}\left[\alpha_z^+\phi_{i,j,k+1} + (1-\alpha_z^+)\phi_{i,j,k}\right] \tag{2.75}$$

$$\phi_{D'} = \frac{1}{2}\left[\alpha_z^-\phi_{i+1,j,k-1} + (1-\alpha_z^-)\phi_{i+1,j,k}\right] + \frac{1}{2}\left[\alpha_z^-\phi_{i,j,k-1} + (1-\alpha_z^-)\phi_{i,j,k}\right]. \tag{2.76}$$

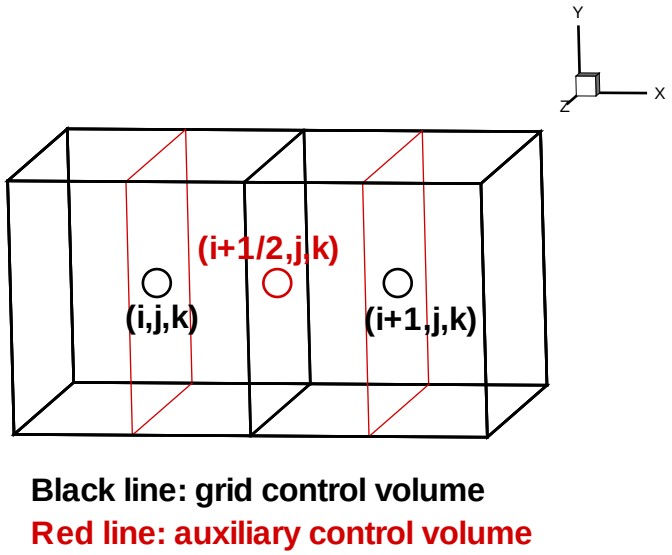

Figure 2.2 Auxiliary control volume for calculation of gradients on east/west (E/W) surfaces of main control volumes

where the coefficients are

$$\alpha_y^+ = \frac{\Delta y'/2}{y_{i,j+1,k} - y_{i,j,k}}; \alpha_y^- = \frac{\Delta y'/2}{y_{i,j,k} - y_{i,j-1,k}}; \tag{2.77}$$

$$\alpha_z^+ = \frac{\Delta z'/2}{z_{i,j,k+1} - z_{i,j,k}}; \alpha_z^- = \frac{\Delta z'/2}{z_{i,j,k} - z_{i,j,k-1}}, \tag{2.78}$$

where $\Delta y'$ and $\Delta z'$ are the dimensions of the auxialiary control volume in the y and z direction, respectively. The surface areas are

$$S'_{EW} = S_{EW} \tag{2.79}$$

$$S'_{NS} = \frac{1}{2}(S_{NS}(i,j,k) + S_{NS}(i+1,j,k)) \tag{2.80}$$

$$S'_{UD} = \frac{1}{2}(S_{UD}(i,j,k) + S_{UD}(i+1,j,k)). \tag{2.81}$$

In the same manner, the gradients on the north/south and up/down faces can be evaluated.

2.4.4 Time Derivative Preconditioning

Eq. (2.67) can be solved by common compressible solvers using time marching. A problem related with the solving procedure is that the convergence speed of the compressible solvers becomes very slow at low Mach numbers. This is due to the large differences in the magnitude of system eigenvalues. For instance, the flux Jacobian matrix in $x-$direction is

$$[A] = \frac{\partial \mathbf{F}_{1,inv}}{\partial \mathbf{W}} \tag{2.82}$$

and the five eigenvalues of matrix $[T]^{-1}[A]$ are $(u+c, u-c, u, u, u)$ where u is the convective speed and c is the local sound speed. As the Mach number tends to zero, the sound speed goes to infinity and the system is singular. In the current research, the preconditioning method developed by Pletcher and Chen (1993) is used to solve above problem when Mach number is very small. The basic idea is to add a pseudo-time derivative to the governing equation Eq. (2.67):

$$[\Gamma]\frac{\partial \mathbf{W}}{\partial \tau}\Omega + [T]\frac{d\mathbf{W}}{dt}\Omega + \mathbf{C}(\mathbf{W}) = \mathbf{S}\Omega, \tag{2.83}$$

in which $[\Gamma]$ is the preconditioning matrix and τ is the pseudo time. $[\Gamma]$ is obtained by multiplying the first column of $[T]$ by the gas constant, as shown in Appendix A. Then the characteristics of the system are controlled by the eigenvalues of the new flux Jacobian matrix $[\Gamma]^{-1}[A]$ and the eigenvalues become much closer to each other so that the condition number

$$\kappa = \frac{\lambda_{max}}{\lambda_{min}} \tag{2.84}$$

becomes close to 1 and therefore the convergence speed is improved dramatically. The addition of the pseudo time derivative is the so-called dual time step approach and involves iterating in pseudo time for each physical time step. The original unsteady governing equations are satisfied when the iteration is converged in pseudo time.

2.4.5 LU-SGS Scheme

In the current study, time integration was performed using the implicit lower-upper symmetric Gauss-Seidel (LU-SGS) scheme. The physical time derivative was discretized with a

second-order three point backward difference,

$$[T]\frac{3\mathbf{W}^{n+1}-4\mathbf{W}^{n}+\mathbf{W}^{n-1}}{2\Delta t}\Omega+\mathbf{C}(\mathbf{W}^{n+1})=\mathbf{S}^{n}\Omega, \tag{2.85}$$

To solve the nonlinear equations, the inviscid flux vectors were linearized about the physical time step as

$$\mathbf{F}_{1,inv}^{n+1} \approx \mathbf{F}_{1,inv}^{n}+[A]^{n}\Delta\mathbf{W}; \quad [A]=\left(\frac{\partial\mathbf{F}_{1,inv}^{n}}{\partial\mathbf{W}}\right)^{n} \tag{2.86}$$

$$\mathbf{F}_{2,inv}^{n+1} \approx \mathbf{F}_{2,inv}^{n}+[B]^{n}\Delta\mathbf{W}; \quad [B]=\left(\frac{\partial\mathbf{F}_{2,inv}^{n}}{\partial\mathbf{W}}\right)^{n} \tag{2.87}$$

$$\mathbf{F}_{3,inv}^{n+1} \approx \mathbf{F}_{3,inv}^{n}+[C]^{n}\Delta\mathbf{W}; \quad [C]=\left(\frac{\partial\mathbf{F}_{3,inv}^{n}}{\partial\mathbf{W}}\right)^{n}. \tag{2.88}$$

The viscous flux vectors and subgrid scale flux vectors were lagged as the values of the previous pseudo time step. Therefore the final equation is written in a "delta" form as

$$[T]\frac{3\Omega}{2\Delta t}\Delta\mathbf{W}+\sum_{\beta=1}^{6}([A]_{\beta}n_{\beta x}+[B]_{\beta}n_{\beta y}+[C]_{\beta}n_{\beta z})S_{\beta}\Delta\mathbf{W}_{\beta}=-\mathbf{R}^{n}, \tag{2.89}$$

where

$$\begin{aligned}\Delta\mathbf{W} &= \mathbf{W}^{n+1}-\mathbf{W}^{n};\\ \mathbf{R}^{n} &= \mathbf{S}^{n}\Omega-\mathbf{C}(\mathbf{W}^{n})-[T]\frac{-\mathbf{W}^{n}+\mathbf{W}^{n-1}}{\Delta t}\Omega.\end{aligned} \tag{2.90}$$

Multiplying the above equation with $[T]^{-1}$ results in

$$\begin{aligned}&\frac{3\Omega}{2\Delta t}\Delta\mathbf{W}+[T]^{-1}[([A]\Delta\mathbf{W}S)_{1}-([A]\Delta\mathbf{W}S)_{3}\\ &+([B]\Delta\mathbf{W}S)_{2}-([B]\Delta\mathbf{W}S)_{4}+([C]\Delta\mathbf{W}S)_{5}-([C]\Delta\mathbf{W}S)_{6}]=-\mathcal{R}^{n},\end{aligned} \tag{2.91}$$

where $\mathcal{R}=[T]^{-1}\mathbf{R}$. The Jacobian matrices can be modified as

$$[A]=[T][\tilde{A}]; \quad [B]=[T][\tilde{B}]; \quad [C]=[T][\tilde{C}]. \tag{2.92}$$

The terms on the surfaces can be approximated as

$$\begin{aligned}([A]\Delta\mathbf{W})_{1} &= ([T][\tilde{A}]\Delta\mathbf{W})_{1}\approx([T][\tilde{A}]^{+}\Delta\mathbf{W})_{i,j,k}+([T][\tilde{A}]^{-}\Delta\mathbf{W})_{i+1,j,k};\\ ([A]\Delta\mathbf{W})_{3} &= ([T][\tilde{A}]\Delta\mathbf{W})_{3}\approx([T][\tilde{A}]^{+}\Delta\mathbf{W})_{i-1,j,k}+([T][\tilde{A}]^{-}\Delta\mathbf{W})_{i,j,k};\end{aligned}$$

$$
\begin{aligned}
([B]\Delta\mathbf{W})_2 &= ([T][\tilde{B}]\Delta\mathbf{W})_2 \approx ([T][\tilde{B}]^{+}\Delta\mathbf{W})_{i,j,k} + ([T][\tilde{B}]^{-}\Delta\mathbf{W})_{i,j+1,k};\\
([B]\Delta\mathbf{W})_4 &= ([T][\tilde{B}]\Delta\mathbf{W})_4 \approx ([T][\tilde{B}]^{+}\Delta\mathbf{W})_{i,j-1,k} + ([T][\tilde{B}]^{-}\Delta\mathbf{W})_{i,j,k};\\
([C]\Delta\mathbf{W})_5 &= ([T][\tilde{C}]\Delta\mathbf{W})_5 \approx ([T][\tilde{C}]^{+}\Delta\mathbf{W})_{i,j,k} + ([T][\tilde{C}]^{-}\Delta\mathbf{W})_{i,j,k+1};\\
([C]\Delta\mathbf{W})_6 &= ([T][\tilde{C}]\Delta\mathbf{W})_6 \approx ([T][\tilde{C}]^{+}\Delta\mathbf{W})_{i,j,k-1} + ([T][\tilde{C}]^{-}\Delta\mathbf{W})_{i,j,k},
\end{aligned}
\tag{2.93}
$$

where

$$
\begin{aligned}
[\tilde{A}]^{\pm} &= \frac{1}{2}([\tilde{A}] \pm \left|\lambda_{[\tilde{A}]}\right|[I]);\\
[\tilde{B}]^{\pm} &= \frac{1}{2}([\tilde{B}] \pm \left|\lambda_{[\tilde{B}]}\right|[I]);\\
[\tilde{C}]^{\pm} &= \frac{1}{2}([\tilde{C}] \pm \left|\lambda_{[\tilde{C}]}\right|[I]).
\end{aligned}
\tag{2.94}
$$

λ is the maximum eigenvalues of the corresponding flux Jacobian matrix and $[I]$ is the identity matrix. From the above equations, it is obvious that

$$
\begin{aligned}
[T][\tilde{A}]^{+} - [T][\tilde{A}]^{-} &= \left|\lambda_{[\tilde{A}]}\right|[T];\\
[T][\tilde{B}]^{+} - [T][\tilde{B}]^{-} &= \left|\lambda_{[\tilde{B}]}\right|[T];\\
[T][\tilde{C}]^{+} - [T][\tilde{C}]^{-} &= \left|\lambda_{[\tilde{C}]}\right|[T].
\end{aligned}
\tag{2.95}
$$

The above equations are substituted into Eq. (2.91) giving

$$
([L] + [D] + [U])\Delta\mathbf{W} = -\mathcal{R}, \tag{2.96}
$$

where

$$
\begin{aligned}
[L] &= -[T]^{-1}\left[([T][\tilde{A}]^{+})_{i-1,j,k}S_3 + ([T][\tilde{B}]^{+})_{i,j-1,k}S_4 + ([T][\tilde{C}]^{+})_{i,j,k-1}S_6\right];\\
[D] &= \frac{3\Omega}{2\Delta t} + [T]^{-1}\left[([T][\tilde{A}]^{+})_{i,j,k}S_1 - ([T][\tilde{A}]^{-})_{i,j,k}S_3\right.\\
&\quad \left. +([T][\tilde{B}]^{+})_{i,j,k}S_2 - ([T][\tilde{B}]^{-})_{i,j,k}S_4 + ([T][\tilde{C}]^{+})_{i,j,k}S_5 - ([T][\tilde{C}]^{-})_{i,j,k}S_6\right];\\
[U] &= -[T]^{-1}\left[([T][\tilde{A}]^{-})_{i+1,j,k}S_1 + ([T][\tilde{B}]^{-})_{i,j+1,k}S_2 + ([T][\tilde{C}]^{-})_{i,j,k+1}S_5\right].
\end{aligned}
\tag{2.97}
$$

For hexagonal control volumes,

$$
S_1 = S_3 = S_{13}; \quad S_2 = S_4 = S_{24}; \quad S_5 = S_6 = S_{56}, \tag{2.98}
$$

we have

$$[D] = \left[\frac{3\Omega}{2\Delta t} + (|\lambda_{[\tilde{A}]}|)_{i,j,k}S_{13} + (|\lambda_{[\tilde{B}]}|)_{i,j,k}S_{24} + (|\lambda_{[\tilde{C}]}|)_{i,j,k}S_{56}\right][I]. \tag{2.99}$$

As shown above, matrix $[D]$ is diagonal.

For preconditioning systems, a pseudo time step was introduced in Eq. (2.85) and the pseudo time derivative was discretized with a first-order Euler backward difference,

$$[\Gamma]\frac{\mathbf{W}^{m+1} - \mathbf{W}^{m}}{\Delta\tau}\Omega + [T]\frac{3\mathbf{W}^{n+1} - 4\mathbf{W}^{n} + \mathbf{W}^{n-1}}{2\Delta t}\Omega + \mathbf{C}(\mathbf{W}^{n+1}) = \mathbf{S}^{m}\Omega \tag{2.100}$$

where m denotes the pseudo time step and n the physical time step. As mentioned above, the solution at physical time step $n+1$ can be regarded as being obtained if the pseudo time iterations converge. Thus, $\mathbf{W}^{n+1}$ can be substituted by $\mathbf{W}^{m+1}$ in the iterations. Multiplying above equation with $[\Gamma]^{-1}$ results in

$$\frac{\Omega}{\Delta\tau}\Delta\mathbf{W} + +[\Gamma]^{-1}[T]\frac{3\Omega}{2\Delta t}\Delta\mathbf{W} + [\Gamma]^{-1}\sum_{\beta=1}^{6}([A]_{\beta}n_{\beta x} + [B]_{\beta}n_{\beta y} + [C]_{\beta}n_{\beta z})S_{\beta}\Delta\mathbf{W}_{\beta} = -\mathcal{R}^{m}, \tag{2.101}$$

where

$$\begin{aligned} \Delta\mathbf{W} &= \mathbf{W}^{m+1} - \mathbf{W}^{m}; \quad \mathcal{R}^{m} = [\Gamma]^{-1}\mathbf{R}^{m}; \\ \mathbf{R}^{m} &= \mathbf{S}^{m}\Omega - \mathbf{C}(\mathbf{W}^{m}) - [T]\frac{3\mathbf{W}^{m} - 4\mathbf{W}^{n} + \mathbf{W}^{n-1}}{2\Delta t}\Omega. \end{aligned} \tag{2.102}$$

For hexagonal control volumes used in the current study, the above equation can be simplified as

$$\begin{aligned} &[\Gamma]^{-1}[T]\frac{3\Omega}{2\Delta t}\Delta\mathbf{W} + [\Gamma]^{-1}[([A]\Delta\mathbf{W}S)_1 - ([A]\Delta\mathbf{W}S)_3 \\ &+([B]\Delta\mathbf{W}S)_2 - ([B]\Delta\mathbf{W}S)_4 + ([C]\Delta\mathbf{W}S)_5 - ([C]\Delta\mathbf{W}S)_6] = -\mathcal{R}^{m}. \end{aligned} \tag{2.103}$$

The Jacobian matrices can be modified as

$$[A] = [\Gamma][\tilde{A}]; \quad [B] = [\Gamma][\tilde{B}]; \quad [C] = [\Gamma][\tilde{C}]. \tag{2.104}$$

The terms on the surfaces can be approximated as

$$([A]\Delta\mathbf{W})_1 = ([\Gamma][\tilde{A}]\Delta\mathbf{W})_1 \approx ([\Gamma][\tilde{A}]^{+}\Delta\mathbf{W})_{i,j,k} + ([\Gamma][\tilde{A}]^{-}\Delta\mathbf{W})_{i+1,j,k};$$

$$
\begin{aligned}
([A]\Delta\mathbf{W})_3 &= ([\Gamma][\tilde{A}]\Delta\mathbf{W})_3 \approx ([\Gamma][\tilde{A}]^+\Delta\mathbf{W})_{i-1,j,k} + ([\Gamma][\tilde{A}]^-\Delta\mathbf{W})_{i,j,k};\\
([B]\Delta\mathbf{W})_2 &= ([\Gamma][\tilde{B}]\Delta\mathbf{W})_2 \approx ([\Gamma][\tilde{B}]^+\Delta\mathbf{W})_{i,j,k} + ([\Gamma][\tilde{B}]^-\Delta\mathbf{W})_{i,j+1,k};\\
([B]\Delta\mathbf{W})_4 &= ([\Gamma][\tilde{B}]\Delta\mathbf{W})_4 \approx ([\Gamma][\tilde{B}]^+\Delta\mathbf{W})_{i,j-1,k} + ([\Gamma][\tilde{B}]^-\Delta\mathbf{W})_{i,j,k};\\
([C]\Delta\mathbf{W})_5 &= ([\Gamma][\tilde{C}]\Delta\mathbf{W})_5 \approx ([\Gamma][\tilde{C}]^+\Delta\mathbf{W})_{i,j,k} + ([\Gamma][\tilde{C}]^-\Delta\mathbf{W})_{i,j,k+1};\\
([C]\Delta\mathbf{W})_6 &= ([\Gamma][\tilde{C}]\Delta\mathbf{W})_6 \approx ([\Gamma][\tilde{C}]^+\Delta\mathbf{W})_{i,j,k-1} + ([\Gamma][\tilde{C}]^-\Delta\mathbf{W})_{i,j,k},
\end{aligned}
\tag{2.105}
$$

where

$$
\begin{aligned}
[\tilde{A}]^{\pm} &= \frac{1}{2}([\tilde{A}] \pm \left|\lambda_{[\tilde{A}]}\right|[I]);\\
[\tilde{B}]^{\pm} &= \frac{1}{2}([\tilde{B}] \pm \left|\lambda_{[\tilde{B}]}\right|[I]);\\
[\tilde{C}]^{\pm} &= \frac{1}{2}([\tilde{C}] \pm \left|\lambda_{[\tilde{C}]}\right|[I]).
\end{aligned}
\tag{2.106}
$$

Substituting the above equation into Eq. 2.103 gives

$$
([L] + [D] + [U])\Delta\mathbf{W} = -\mathcal{R}, \tag{2.107}
$$

where

$$
\begin{aligned}
[L] &= -[\Gamma]^{-1}_{i,j,k}\left[([\Gamma][\tilde{A}]^+)_{i-1,j,k}S_3 + ([\Gamma][\tilde{B}]^+)_{i,j-1,k}S_4 + ([\Gamma][\tilde{C}]^+)_{i,j,k-1}S_6\right];\\
[D] &= ([\Gamma]^{-1}[T])_{i,j,k}\frac{3\Omega}{2\Delta t} + [\Gamma]^{-1}_{i,j,k}\left[([\Gamma][\tilde{A}]^+)_{i,j,k}S_1 - ([\Gamma][\tilde{A}]^-)_{i,j,k}S_3\right.\\
&\quad \left. +([\Gamma][\tilde{B}]^+)_{i,j,k}S_2 - ([\Gamma][\tilde{B}]^-)_{i,j,k}S_4 + ([\Gamma][\tilde{C}]^+)_{i,j,k}S_5 - ([\Gamma][\tilde{C}]^-)_{i,j,k}S_6\right];\\
[U] &= -[\Gamma]^{-1}_{i,j,k}\left[([\Gamma][\tilde{A}]^-)_{i+1,j,k}S_1 + ([\Gamma][\tilde{B}]^-)_{i,j+1,k}S_2 + ([\Gamma][\tilde{C}]^-)_{i,j,k+1}S_5\right].
\end{aligned}
\tag{2.108}
$$

For hexagonal control volumes under Cartesian coordinates,

$$
S_1 = S_3 = S_{13}; \quad S_2 = S_4 = S_{24}; \quad S_5 = S_6 = S_{56}, \tag{2.109}
$$

then we have

$$
[D] = ([\Gamma]^{-1}[T])_{i,j,k}\frac{3\Omega}{2\Delta t} + \left[(\left|\lambda_{[\tilde{A}]}\right|)_{i,j,k}S_{13} + (\left|\lambda_{[\tilde{B}]}\right|)_{i,j,k}S_{24} + (\left|\lambda_{[\tilde{C}]}\right|)_{i,j,k}S_{56}\right][I]. \tag{2.110}
$$

Due to the nature of the preconditioning matrix we chose, the product $[\Gamma]^{-1}[T]$ is a diagonal matrix so the matrix $[D]$ is also diagonal. To efficiently solve Eq. (2.107), it can be approximated as

$$
([L] + [D])[D]^{-1}([D] + [U])\Delta\mathbf{W} = -\mathcal{R}, \tag{2.111}
$$

and solved in three steps as follows:

$$\text{Step 1:} \qquad ([L]+[D])\Delta\mathbf{W}^* = -\mathcal{R} \tag{2.112}$$

$$\Delta\mathbf{W}^* = [D]^{-1}(-\mathcal{R} - [L]\Delta\mathbf{W}^*);$$

$$\text{Step 2 :} \qquad ([D]+[U])\Delta\mathbf{W} = [D]\Delta\mathbf{W}^*, \tag{2.113}$$

$$\Delta\mathbf{W} = \Delta\mathbf{W}^* - [D]^{-1}[U]\Delta\mathbf{W};$$

$$\text{Step 3 :} \qquad \mathbf{W}^{m+1} = \mathbf{W}^m + \Delta\mathbf{W}.$$

In step 1, the calculation is carried out on $i+j+k = constant$ planes from the lower corner, $(i,j,k) = (1,1,1)$, to the upper corner, $(i,j,k) = (ni, nj, nk)$, of the grid, where ni, nj, nk are the number of control volumes in the x, y, and z directions, respectively. Through this procedure, $[L]\mathbf{W}^*$ are always known during the process and thus it can be put on the right hand side of the equation. Similarly, $[U]\Delta\mathbf{W}$ is also always known during the sweeping from upper corner to lower corner in step 2 and is moved to the right hand side. Since $[D]$ is diagonal, the inversion of $[D]$ in the above steps requires only a trivial amount of work.

2.5 Boundary Conditions

In this study, boundary conditions are generally enforced by using "ghost" volumes except where immersed boundary treatment is imposed. The ghost volumes are images of the corresponding near boundary control volumes. For instance,

$$\phi_b = \frac{1}{2}(\phi_{nb} + \phi_g), \tag{2.114}$$

where ϕ_b is the value of variable ϕ at the boundary, ϕ_{nb} the value at the near boundary control volume and ϕ_g the value at the ghost volume. Since ϕ_{nb} is updated in each iteration, ϕ_g can be set up at the beginning of the next iteration according to ϕ_{nb} so that a certain boundary value ϕ_b can be enforced. Sometimes it is the normal derivative which is enforced at the boundary. In such cases, the ghost volume values is determined as

$$\phi_g = \phi_{nb} + \left(\frac{\partial\phi}{\partial n}\right)_b \Delta l, \tag{2.115}$$

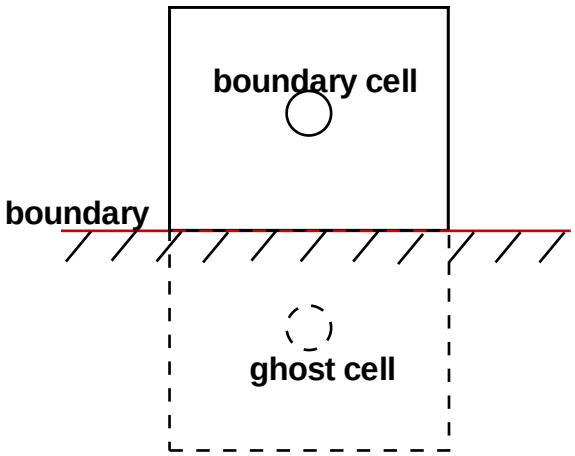

Figure 2.3 Ghost volumes for boundary conditions

where Δl is the distance between the volume centers. Some of the most commonly used boundary conditions in DNS and LES are described next.

2.5.1 Solid Wall Boundary Conditions

On solid walls, the no slip condition has to be enforced for all velocity components as

$$u_g = -u_{nb}; \quad v_g = -v_{nb}; \quad w_g = -w_{nb}. \tag{2.116}$$

The pressure condition at a solid wall is set as $p_g = p_{nb}$ to fulfill the approximate boundary condition $\partial p/\partial n = 0$. For cases involving heat transfer, two different temperature conditions can be applied at a solid wall: fixed wall temperature or fixed wall heat flux. A desired wall temperature, T_w, is enforced by setting $T_g = 2T_w - T_{nb}$. To enforce a fixed non-dimensional wall heat flux, q_w, at the wall, the temperature at the ghost volume is given by

$$T_g = T_{nb} + \frac{q_w RePr}{\mu_w}\Delta l. \tag{2.117}$$

Here the definition of q_w is different from that of Eq. (2.13). The non-dimensional wall heat flux q_w is given in terms of the dimensional quantities as

$$q_w = \frac{q_w^*}{\rho_{ref} U_{ref} T_{ref} c_p^*}. \tag{2.118}$$

2.5.2 Periodic Boundary Conditions

Periodic boundary conditions have been extensively used in DNS and LES of incompressible or constant property flows. This condition is especially suitable for fully developed homogeneous flow since the flow fields at inflow and outflow are considered as statistically the same provided they are apart from each other far enough. For periodic boundary conditions, the computational domain can be thought of as repeating itself infinitely. With the method of ghost volumes, this can be done by copying values of the variables of the near outflow/inflow boundary control volume to the ghost volume at the inflow/outflow boundary. The periodicity suggests that at inflow

$$\begin{aligned} (\rho u)_g &= (\rho u)_{0,j,k} = (\rho u)_{ni,j,k}; \\ v_g &= v_{0,j,k} = v_{ni,j,k}; \\ w_g &= w_{0,j,k} = w_{ni,j,k}; \\ T_g &= T_{0,j,k} = T_{ni,j,k}. \end{aligned} \tag{2.119}$$

However, the pressure is not periodic in the flow direction due to the negative, linear streamwise pressure gradient which drives the flow. A common practice is to decompose the pressure into pressure gradient term and periodic pressure term as

$$p(x, y, z, t) = \beta x + p_p(x, y, z, t), \tag{2.120}$$

where β is the streamwise pressure gradient. Since the pressure gradient term is much smaller than the periodic pressure term for moderate Reynolds numbers, the pressure p may be replaced with p_p in the governing equations and at the same time the pressure gradient enters the right hand side of the u-momentum equation as a "forcing function". This forcing function is determined by requiring that the mean mass flow rate reach a desired constant $\left(\frac{\dot{m}}{A_c}\right)^0$.

Following the approach of Benocci and Pinelli (1990), β is calculated dynamically at each physical time step as

$$\beta^{n+1} = \beta^n - \frac{1}{\Delta t}\left[\left(\frac{\dot{m}}{A_c}\right)^0 - 2\left(\frac{\dot{m}}{A_c}\right)^n + \left(\frac{\dot{m}}{A_c}\right)^{n-1}\right], \tag{2.121}$$

where A_c is the cross-flow area. However, periodic boundary conditions cannot be used for developing flows, heat transfer cases with property variations and very complex geometry flows.

2.5.3 Step-periodic Boundary Conditions

For the heat transfer cases with property variations, the periodicity assumptions were not valid for pressure, temperature and streamwise velocity. Dailey (1997) proposed a step-periodic boundary condition to approximate the problem,

$$\begin{aligned} (\rho u)(0,y) &= (\rho u)(L_x,y); \\ v(0,y) &= v(L_x,y); \\ w(0,y) &= w(L_x,y); \\ p_p(0,y) &= p_p(L_x,y); \\ T(0,y) &= T(L_x,y) - \Delta T_x, \end{aligned} \tag{2.122}$$

where L_x is the length of the channel in the streamwise direction and the temperature difference ΔT_x is given by integrating the energy equation.

2.5.4 N-S Characteristic Boundary Conditions

A large number of direct and large eddy simulations have used periodic boundary conditions in one or more directions. With the assumption of periodicity, the computational domain is thought of as being repeated infinitely. However, the periodicity assumption cannot be justified in a wide range of situations, such as situations include the developing flows, heat transfer cases with large property variations, non-uniform geometries, free shear or jet flows. Also, it is known that imposing the pressure on a subsonic compressible outflow gives rise to strong reflections in the flow which can cause the numerical solution to oscillate or even blow up (Anderson, 1995).

For compressible flow systems, the classical method of charateristics solution (Hedstrom, 1979) is usually used. It is based on the fact that a hyperbolic system can be decomposed into wave modes propagating along the characteristic directions, which can be going into or out of the computational domain. The outgoing waves are completely determined by the interior solution and no boundary condition can be applied to them. It is waves entering the domain from outside its boundary, together with the state in the interior, that determines the time evolution of the system. For the case of one-dimensional flow, it is possible to locally identify and decouple the outgoing and incoming waves. Then, we can enforce the boundary condition we wish on the incoming waves. Boundary conditions obtained this way are named characteristic boundary conditions (CBC). In this study the NSCBC method proposed by Thompson (1990), Poinsot and Lele (1992) and Kim and Lee (2000) was used for non-periodic flow cases. For fully developed flows, the regular periodic boundary condition was imposed. The basic formulation of NSCBC is described in Appendix C and the detailed derivation and implementation procedure can be found in the work of Qin (2007).

CHAPTER 3. NON-BODY CONFORMAL GRID TREATMENT

In this chapter, details of the non-body conformal grid method are described. And the possibility to extend it to moving boundary problems is also discussed.

3.1 Introduction

The conventional approach to simulate flows with complex boundaries is to use either a curvilinear body-fitted grid that conforms to the boundaries or an unstructured grid which offers more flexibility in grid generation. For body-fitted grids, the imposition of boundary conditions is straightforward and the solver can be easily designed to maintain accuracy and conservation properties. However, grid generation and grid quality can be an issue for very complex geometries. For unstructured grids, since the powerful line/block iteration techniques are not easy to implement and due to lack of general orthogonality, the performance of the simulation is in general slower than with structured grid methods. In this study, a different approach, the immersed boundary method, is used which retains most of the favorable properties of structured grids and also provides more flexibility in grid generation. However, the main challenge of the immersed boundary method is the boundary treatment since the immersed boundary can cut through the underlying grid lines. It is crucial to maintain the expected accuracy and conservation property of the solver near the boundary.

Generally, immersed boundary methods can be categorized into two main groups (Mittal and Iaccarino, 2005): (a) "Continuous forcing": a forcing term is added to the continuous Navier-Stokes equations before the discretization. The original method of Peskin (1972), and the so-called virtual boundary method applied to rigid boundaries by Goldstein et al. (1993) and Saiki and Biringen (1996) belong to this category. (b) "Discrete forcing": forcing terms

are added to the discretized Navier-Stokes equations. These include methods of Ye et al. (1999), Fadlun et al. (2000), Kim et al. (2001), You et al. (2003), Balaras (2004), Yang and Balaras (2006), Ghias et al. (2007) and others. The major difference in the two categories is that the continuous forcing can be added into the governing equation independent of the grid generation, while the discrete forcing largely depends on the spatial discretiztion scheme. The feature of discrete forcing method allows the "sharp" representation of the immeresed boundary, in contrast to the "diffuse" boundary treatment in the first category, where the boundary condition is not satisfied precisely at its actual location but within a localized region near the boundary (Ghias et al., 2007). However, a major challenge of the discrete forcing method is that, with the increase of Reynolds number, the accuracy requirement near the boundary may cause a rapid increase of grid resolution. Therefore, for very complex geometry flows, the local grid refinement method may be combined with the immersed boundary method to achieve a more efficient solution.

3.2 Non-body conformal grid methods

In this dissertation, two non-body conformal grid methods have been studied: direct forcing method and ghost cell method.

3.2.1 Direct forcing method

The main steps in applying the direct forcing method are discussed in the following sections.

3.2.1.1 Interface description

A two-dimensional immersed interface ψ is represented by a series of interfacial marker points, which are defined by arc length coordinates $\mathbf{X}(s,t)$. The marker points are uniformly distributed on the interface with a spacing approximately equal to the local grid size. The direction of the interface boundary is defined such that the fluid is always to the left of the observer as one moves along the direction of the increasing coordinates. The coordinates of

marker points can be written as

$$\begin{aligned} x(s,t) &= a_x s^2 + b_x s + c_x, \\ y(s,t) &= a_y s^2 + b_y s + c_y. \end{aligned} \tag{3.1}$$

The coefficients $a_{x(y)}, b_{x(y)}, c_{x(y)}$ are obtained by fitting the quadratic polynomials to the marker point and its two neighbors. The normal vector at each marker point is then calculated as

$$n_x = \frac{-y_s}{\sqrt{x_s^2 + y_s^2}}, \quad n_y = \frac{x_s}{\sqrt{x_s^2 + y_s^2}}, \tag{3.2}$$

where the derivatives x_s, y_s are

$$x_s(s,t) = 2a_x s + b_x s, \quad y_s(s,t) = 2a_y s + b_y s. \tag{3.3}$$

For the three dimensional interfaces a B-spline fitting method can be used.

3.2.1.2 Forcing points identification

Having parameterized the immersed interface with a series of marker points, the forcing points can be identified by evaluating a signed distance function defined at each grid point. First a search process is employed to locate a surface marker point closest to each grid point. Then a signed distance function (Choi et al. (2007)) from each grid point $\mathbf{x}_k \in \Omega$ to the nearest surface point $\mathbf{X}_l(s) \in \Gamma$ is defined as

$$\phi(\mathbf{x}_k, t) = \text{sgn}\left[(\mathbf{x}_k - \mathbf{X}_l) \cdot \mathbf{n}_l\right] \times ||\mathbf{x}_k - \mathbf{X}_l||. \tag{3.4}$$

The above function $\phi(\mathbf{x}_k, t)$ returns a positive value for the points that belong to the fluid phase and a negative value for the points that belong to the solid phase. Then the forcing points are identified as the grid points in the fluid phase with $\phi(\mathbf{x}_k, t) > 0$ and having at least one solid neighbor point. Also, the value of the signed distance function at these points is reset to zero. Figure 3.1 presents the basic topology of the three categories of grid points in a two-dimensional case.

For a stationary boundary problem the above tagging process is done only at the beginning of the computation and remains unchanged thereafter. For moving boundary problems, this

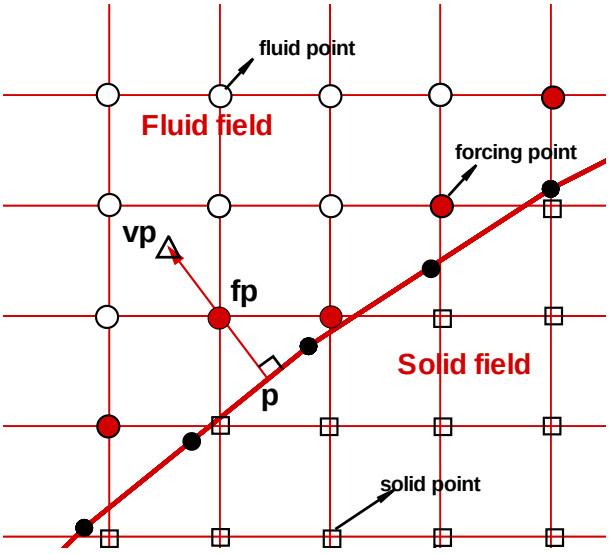

Figure 3.1 Schematic diagram of immersed boundary notation.

search and tagging process is repeated at each time step. Also, the projection point (x_p, y_p) of the forcing point on the immersed interface will be determined by combining the normal vector function and the parametric function of the interface.

3.2.1.3 Forcing function calculation

The basic idea of the immersed boundary method is to satisfy the desired boundary condition on the immersed interface through adding forcing terms to the Navier-Stokes equation. In the current study both Dirichlet and Neumann boundary conditions have been considered. The Robin condition can be applied in a similar fashion. For the Dirichlet boundary condition, the simplest case is the no-slip boundary condition. The idea is that the velocity of the fluid must be equal to the velocity of the immersed interface. This is achieved by applying a momentum forcing such that the desired velocity on the boundary is recovered at each time step. Similarly, an energy forcing term can be applied to achieve the desired temperature boundary condition. Considering the simplest case that a Cartesian grid point coincides with the immersed boundary, the forcing function can be obtained by setting $\mathbf{W}^{k+1} = \mathbf{W}_{fp}$, and

solving for $\mathbf{f}_{fp}^{k+1}$,

$$\mathbf{f}_{fp}^{k+1} = [T]\frac{\mathbf{W}_{fp} - \mathbf{W}_i^k}{\Delta t}\Omega + \sum_{j=1}^{6} \mathbf{F}_{ij}^k n_{ji} S_j, \tag{3.5}$$

where the forcing function is denoted by $\mathbf{f}_{fp} = (0, f_u, f_v, f_w, f_e)^T$ and $\mathbf{W}_{fp}$ is the desired value satisfying the boundary condition on the forcing points. It should be pointed out that in the absence of an immersed body, the sub-iteration of the dual time step procedure serves to eliminate time linearization errors and preconditioning errors. When an immersed body is included, the subiteration also serves to adjust the velocity and pressure fields to the desired solution.

However, generally the solid interface does not coincide with the Cartesian grid nodes and the desired value $\mathbf{W}_{fb}$ is typically unknown. In this case, an interpolation procedure is needed to reconstruct the appropriate primitive variables $\mathbf{W}_{fb}$ on the forcing points. In the current solver, the Navier-Stokes equations are not solved for the forcing and interior points. The flow properties at these points are determined by the solutions in neighboring cells and the surface points. For interior points, the forcing velocities are set to that of the nearest surface point, and the pressure is set to the free stream value. At the forcing points, a linear interpolation method similar to that of Balaras (2004) was implemented. This method assumes that the forcing points are very close to the solid interface such that the velocity profile can be considered to be linear. This assumption is appropriate for some low Reynolds flows. For higher Reynolds number flows, a higher order interpolation method discussed in the subsequent section can be used.

To implement the linear interpolation, a line through the forcing point and normal to the surface was drawn and the projection point on the boundary was determined. Then the distance between the forcing point fp and the projection point p shown in Fig. 3.1 can be calculated. Along the direction of the vector $\mathbf{x}_{fp} - \mathbf{x}_p$, a virtual point vp satisfying condition $\mathbf{x}_{vp} - \mathbf{x}_{fp} = \mathbf{x}_{fp} - \mathbf{x}_p$ can be identified. The desired value of any scalar ϕ at the forcing point can be calculated as

$$\phi_{fp} = \frac{1}{2}(\phi_{vp} + \phi_p), \tag{3.6}$$

where ϕ_{vp} is calculated with a bilinear(2D) or trilinear(3D) interpolation method by employing

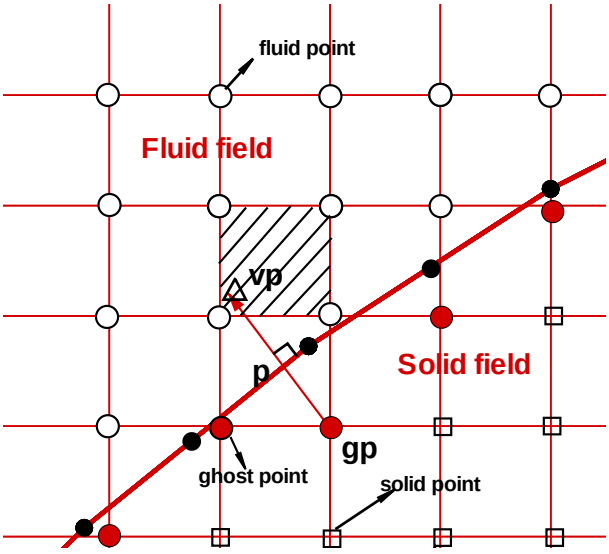

Figure 3.2 Schematic diagram of ghost cell method (case 1).

a stencil composed of all of the neighbor fluid field points of *vp*.

3.2.2 Ghost cell method

Another popular non-body conformal grid method used in immersed boundary problems is the so called ghost cell method. Applications of Tseng and Ferziger (2003), Ghias et al. (2007) belong to this category. Instead of the definition of forcing points in the fluid field, a series of ghost cells located within the solid field are identified. As defined in Tseng and Ferziger (2003), ghost cells are those cells lying just inside the solid body adjacent to computational nodes in the flow domain. The boundary condition on the immersed interface is satisfied by constructing a stencil around the interface and evaluating the flow variables or forcing functions at the ghost cell. Similar to the direct forcing method, a virtual point along the outward normal direction is defined such that $||\mathbf{x}_{vp} - \mathbf{x}_p|| = ||\mathbf{x}_p - \mathbf{x}_{gp}||$. After the flow variables at the virtual node are obtained from construction, the flow variable at ghost node *gp* is obtained by linear interpolation between surface point p and virtual point *vp*.

As shown in Fig. 3.2, a stencil surrounding the immersed interface was constructed to evaluated the flow variables at the ghost points.

The boundary condition on the immersed boundary can be either the Dirichlet type,

$$\phi_p = \psi, \tag{3.7}$$

or the Neumann type

$$(\mathbf{n} \cdot \nabla\phi)_p = \psi. \tag{3.8}$$

In the two-dimensional case, the value of any scalar variable at the virtual point can be expressed in terms of a bi-linear interpolant of the form,

$$\phi = C_1 xy + C_2 x + C_3 y + C_4, \tag{3.9}$$

where the coefficients $C_i, i = 1, ..., 4$ can be expressed in terms of the value of the variable at the four surrounding nodes. Based on the location of the ghost node, three different situations can be encountered and these have to be handled in a well-posed and consistent manner.

The simplest situation is that all surrounding nodes of the virtual point are in the fluid. To determine the coefficients, the above approximate equation can be expanded within the stencil surrounding the virtual point as:

$$\Phi = [Y]C, \tag{3.10}$$

where

$$\Phi = \begin{Bmatrix} \phi_1 \\ \phi_2 \\ \phi_3 \\ \phi_4 \end{Bmatrix} \tag{3.11}$$

are the values of the variable at the four surrounding points and

$$[Y] = \begin{bmatrix} x_1 y_1 & x_1 & y_1 & 1 \\ x_2 y_2 & x_2 & y_2 & 1 \\ x_3 y_3 & x_3 & y_3 & 1 \\ x_4 y_4 & x_4 & y_4 & 1 \end{bmatrix} \tag{3.12}$$

is the coordinates matrix and

$$C = \begin{Bmatrix} C_1 \\ C_2 \\ C_3 \\ C_4 \end{Bmatrix} \tag{3.13}$$

are the coefficients to be determined. Since these four coefficients depend upon the coordinates and the values of scalar variables at the surrounding points, the value ϕ at the virtual point can be finally written as

$$\phi_{vp} = \sum_{i=1}^{4} a_i \phi_i, \tag{3.14}$$

where a_is are functions of the coordinates of the virtual point and the surrounding points.

The second situation occurs when one of the surrounding points is the forcing point itself (Fig. 3.3). The use of the forcing point value in the interpolation scheme is not well-posed. In this case, the boundary condition at the projection point can be used along with the other three surrounding points to close the interpolation. When a Dirichlet boundary condition is specified, it is straightforward to use the coordinates and value at the projection point directly in Eq. (3.10). On the other hand, if a Neumann boundary condition is imposed, e.g.

$$(\mathbf{n} \cdot \nabla \phi)_p = \psi, \tag{3.15}$$

the interpolation formulation needs to be changed. The gradient $\nabla\phi$ can be evaluated through the assumed interpolation formulation so the above equation can be rewritten as

$$n_x(C_1 y + C_2)_p + n_y(C_1 x + C_3)_p = \psi. \tag{3.16}$$

The the corresponding coordinate matrix can be written as

$$[Y] = \begin{bmatrix} x_1 y_1 & x_1 & y_1 & 1 \\ x_2 y_2 & x_2 & y_2 & 1 \\ x_3 y_3 & x_3 & y_3 & 1 \\ n_x y_p + n_y x_p & n_x & n_y & 0 \end{bmatrix} \tag{3.17}$$

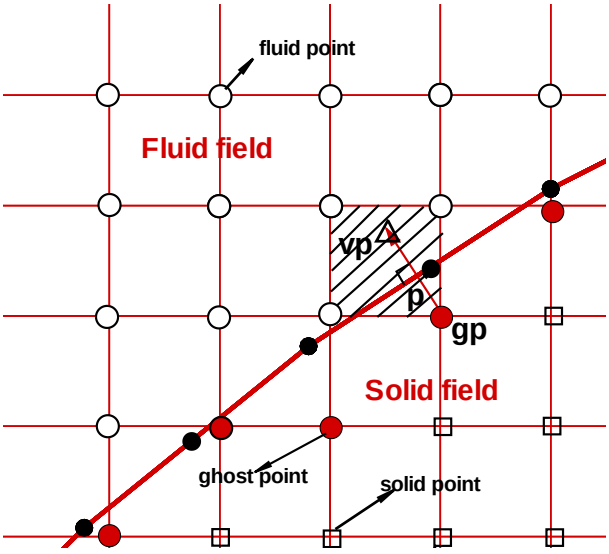

Figure 3.3 Schematic diagram of ghost cell method (case 2).

and the vector Φ is written as

$$\phi = \left\{ \begin{array}{c} \phi_1 \\ \phi_2 \\ \phi_3 \\ \psi \end{array} \right\}. \tag{3.18}$$

The third case is when the interpolation stencil of the current forcing point contains a forcing point other than itself (Fig. 3.4). In the current context, since the dual time step approach is utilized, the inner iteration would update the value of all forcing points iteratively until convergence. It was found that the use of the value at other forcing points is well-posed and therefore no special treatment is needed for this situation.

With the value at the virtual points expressed in terms of the surrounding points and boundary values, the value at ghost node can be obtained as

$$\phi_{gp} = \alpha \phi_{vp} + \beta, \tag{3.19}$$

where $\alpha = -1$ and $\beta = 2\phi_p$ for a Dirichlet boundary condition, $\alpha = 1$ and $\beta = \psi \cdot (\mathbf{x}_{gp} - \mathbf{x}_{vp})$ for a Neumann boundary condition. By combining Eqs. (3.14) and (3.19), the final expression

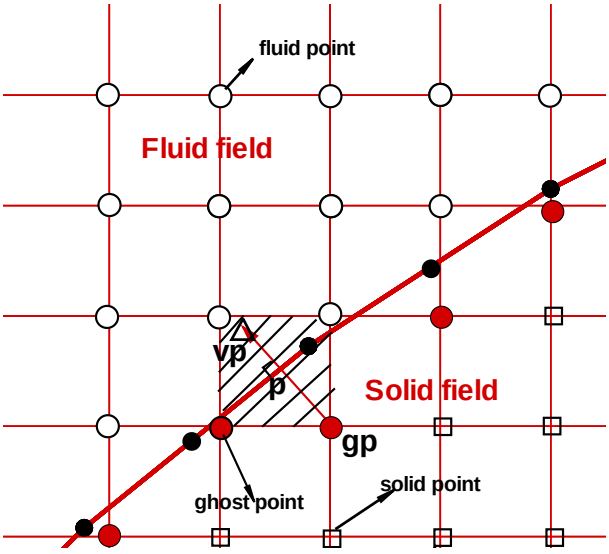

Figure 3.4 Schematic diagram of ghost cell method (case 3).

for the forcing point can be written as

$$\phi_{gp} = \alpha \sum_{i=1}^{4} a_i \phi_i + \beta. \tag{3.20}$$

For the pressure boundary condition near the interface, consider the projection of the momentum equation in the direction normal to the interface:

$$\frac{D\mathbf{u}}{Dt} \cdot \mathbf{n} = -\nabla p \cdot \mathbf{n} + \frac{1}{Re} \nabla^2 \mathbf{u} \cdot \mathbf{n}, \tag{3.21}$$

If the velocities are linearized at the immersed interface the above equation reduces to:

$$\frac{\partial p}{\partial n} = -\frac{D\mathbf{u}}{Dt} \cdot \mathbf{n}. \tag{3.22}$$

For a stationary boundary, due to the no-slip boundary condition, the right-hand side also disappears. Therefore the pressure satisfies a Neumann boundary condition $\frac{\partial p}{\partial n} = 0$. To satisfy this pressure boundary condition, the pressure at the forcing points are determined based on the method described above.

For large eddy simulation, the subgrid scale turbulent viscosity ν_t is required in the computation of diffusion fluxes near the interface and is determined by a dynamic procedure that involves filtering at two different length scales. The first filtering operation is implicit and

corresponds to a filter width that is equal to the local grid spacing. The second filter (test filter) corresponds to a filter width of twice the local grid spacing, which may involve points from the interior of the solid body. To avoid the contamination of non-physical calculation with these solid points, a linear reconstruction procedure similar to the primitive variables can be applied, where the value of ν_t on the boundary is set to be $(\nu_t)_p = 0$.

3.2.3 Other interpolation methods

For higher Reynolds number flows, if the grid resolution is not fine enough such that the forcing points are not located within the viscous sublayer, the velocity distribution at the forcing points can not be assumed to be linear. Choi et al. (2007) suggested another interpoloation method to obtain the appropriate value for velocity and pressure.

In this method, the velocity distribution along the outward normal to the solid interface is defined in terms of three components,

$$\mathbf{U}_{fp}(n) = \mathbf{u}_{fp,t}(n) + \mathbf{u}_{fp,n}(n) + \mathbf{u}_p, \tag{3.23}$$

where $\mathbf{u}_{fp,t}(n)$ and $\mathbf{u}_{fp,n}(n)$ the tangential and normal component of $\mathbf{u}_{fp}(n)$, respectively. $\mathbf{u}_p$ is the velocity at the immersed surface. To conserve momentum, the second derivative of the wall normal velocity should vanish at the surface. Also $\mathbf{u}_{fp,n}(n) = 0$ at $n = 0$. Therefore, a cubic function can be assumed for $u_{fp,n}$ as

$$u_{fp,n} = (a + bn^2)\left(\frac{n}{d_{vp}}\right), \tag{3.24}$$

where vp is the virtual point along the normal direction. The distance from point vp to the immersed interface can be determined either the same as in the linear interpolation method or through another procedure described in the next section. The boundary condition for the above equation is

$$u_{fp,n}|_{n=d_{vp}} = a + bd_{vp}^2 = u_{vp,n} \tag{3.25}$$

$$\frac{du_{fp,n}}{dn}|_{n=d_{vp}} = \left[\frac{2bn^2}{d_{vp}} + (a + bn^2)\frac{1}{d_{vp}}\right]_{n=d_{vp}} = \left[2bd_{vp}^2 + u_{vp,n}\right]\frac{1}{d_{vp}}. \tag{3.26}$$

The coefficients a and b can be determined in terms of $u_{vp,n}$ and $\frac{du_{fp,n}}{dn}|_{n=d_{vp}}$. Then $u_{fp,n}$ can be expressed as

$$u_{fp,n} = \left[u_{vp,n} + \frac{1}{2}\left(d_{vp}\frac{du_{fp,n}}{dn}|_{n=d_{vp}} - u_{vp,n}\right)\left((\frac{n}{d_{vp}})^2 - 1\right)\right]\left(\frac{n}{d_{vp}}\right), \tag{3.27}$$

where the velocity is evaluated as $u_{vp,n} = (\mathbf{U}_{vp} - \mathbf{u}_p)\cdot\mathbf{n}$. The tangential component is written in terms of a general power law $\approx n^k$ with $k = 1/7$ or $k = 1/9$ to approximate the logarithmic distribution near the wall. Also, since $u_{fp,t}(n) = 0$ at $n = 0$, $u_{fp,t}(n)$ is assumed to be

$$u_{fp,t} = (a + bn)\left(\frac{n}{d_{vp}}\right)^k, \tag{3.28}$$

and the boundary condition is

$$\begin{aligned} u_{fp,t}|_{n=d_{vp}} &= a + bd_{vp} = u_{vp,t} && (3.29)\\ \frac{du_{fp,t}}{dn}|_{n=d_{vp}} &= \left[b(\frac{n}{d_{vp}})^k + \frac{k(a+bn)}{n}(\frac{n}{d_{vp}})^k\right]_{n=d_{vp}} = \left[b + \frac{ku_{vp,t}}{d_{vp}}\right]. && (3.30)\end{aligned}$$

After solving for the coefficients a and b in terms of $u_{vp,t}$ and $du_{fp,t}/dn|_{n=d_{vp}}$, the final expression for $u_{fp,t}$ is

$$u_{fp,t} = \left[u_{vp,t} + \left(d_{vp}\frac{du_{fp,t}}{dn}|_{n=d_{vp}} - ku_{vp,t}\right)\left((\frac{n}{d_{vp}}) - 1\right)\right]\left(\frac{n}{d_{vp}}\right)^k, \tag{3.31}$$

with $u_{vp,t} = (\mathbf{U}_{vp} - \mathbf{u}_p)\cdot\mathbf{t}$.

Furthermore, a general procedure for pressure interpolation can be expressed in terms of a second order polynomial as

$$p(n) - p_\infty = (a + bn + cn^2), \tag{3.32}$$

with boundary condition

$$\begin{aligned} (p(n) - p_\infty)|_{n=0} &= a,\\ \frac{dp}{dn}|_{n=0} &= b \end{aligned} \tag{3.33}$$

and

$$\begin{aligned} (p(n) - p_\infty)|_{n=d_{vp}} &= a + bd_{vp} + cd_{vp}^2 = p(d_{vp}),\\ \frac{dp}{dn}|_{n=d_{vp}} &= b + 2cd_{vp}. \end{aligned} \tag{3.34}$$

By assuming the pressure gradient at the wall $b = \frac{dp}{dn}|_{n=0} = 0$, the pressure distribution along the normal direction can be expressed in terms of $p(n)|_{n=d_{vp}}$ and $\frac{dp}{dn}|_{n=d_{vp}}$ as

$$p(n) = p(d_{vp}) + \frac{1}{2} d_{vp} (\frac{dp}{dn}|_{n=d_{vp}}) \left((\frac{n}{d_{vp}})^2 - 1 \right). \tag{3.35}$$

Therefore, the pressure at the immersed interface is

$$p(n) = p(d_{vp}) - \frac{1}{2} d_{vp} (\frac{dp}{dn}|_{n=d_{vp}}). \tag{3.36}$$

3.2.3.1 Virtual point determination

To obtain the values at forcing points, the flow variables at virtual points need to be determined first. In the linear interpolation method, the virtual point is obtained by extending the outward normal from the forcing point an equal distance $d = ||\mathbf{x}_{fp} - \mathbf{x}_p||$ such that $d = ||\mathbf{x}_{vp} - \mathbf{x}_{fp}||$. In the higher order interpolation method, it is well known that high order polynomial interpolations are prone to introduce wiggles and spurious extrema (Iaccarino and Verzicco, 2003). Therefore, an inverse distance weighted method used by Choi et al. (2007) can be employed for the purpose of preserving local maxima and producing a smooth reconstruction. Given the location of a forcing point and a list of its nearest neighbors as shown in Fig. 3.5, a weighting function w_l can be calculated as

$$w_l = \xi_l / \sum_i \xi_i, \tag{3.37}$$

where the merit function ξ_l is calculated as

$$\xi_l = \begin{cases} \frac{1}{\sqrt{||\mathbf{x}_l - \mathbf{x}_{fp}||^2 - [(\mathbf{x}_l - \mathbf{x}_{fp}) \cdot \mathbf{n}]^2 + \epsilon}}, & \text{if } (\mathbf{x}_l - \mathbf{x}_{fp}) \cdot \mathbf{n} > 0 \\ 0 & \text{otherwise.} \end{cases} \tag{3.38}$$

In above equation, $(\mathbf{x}_l - \mathbf{x}_{fp}) \cdot \mathbf{n}$ is the projection of the distance d_{vp} from $\mathbf{x}_{fp}$ to $\mathbf{x}_l$ in the direction of the outward normal and $||\mathbf{x}_l - \mathbf{x}_{fp}||$ is the distance magnitude. ϵ is taken to be a very small number (e.g. 10^{-10}) such that ξ_l is very large when point x_l is located along the normal line. Then the distance d_{vp} is calculated as

$$d_{vp} = \sum_l w_l d_l = \sum_l w_l (\mathbf{x}_l - \mathbf{x}_{fp}) \cdot \mathbf{n}. \tag{3.39}$$

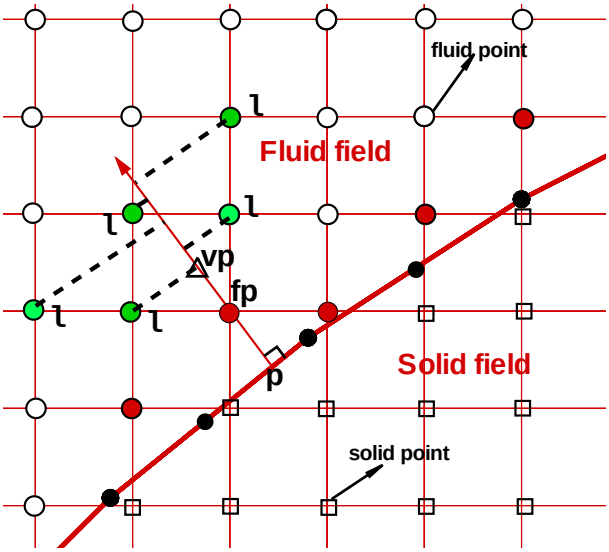

Figure 3.5 Higher order interpolation scheme.

With the location of the virtual point is determined, the flow properties at this point are calculated as

$$\phi_{vp} = \sum_l w_l \phi_l, \quad \left(\frac{d\phi_{vp}}{dn}\right)_{n=d_l} = \sum_l w_l \left(\frac{\partial \phi_{vp}}{\partial x_j}\right)_l n_j. \tag{3.40}$$

3.3 Treatment of moving immersed boundaries

As discussed in Yang and Balaras (2006), the boundary treatment in the moving boundary problem can become more complicated since the role of the grid points near the interface changes with the moving direction of the body. The evaluation of the terms in the governing equation requires physical values of the velocity, pressure and their derivatives from the previous time step at all fluid grid points. Due to the location change of the interface, it is possible that some of the values of the points near the interface are not physical.

Generally, there are two scenarios in terms of the relation between the moving interface and the underlying grid points in the close-up view. In the first case, the solid interface approaches the flow field such that flow grid points become solid grid points. Due to the CFL number restriction, the interface cannot move by more than one grid cell in each time step. Therefore there are two possibilities associated with this scenario, either flow points become forcing points or forcing points turn into solid points. In either situation, the solution for forcing points or

solid points at time $t+1$ will be reconstructed from the flow field and does not depend on their history. In the second case, the solid interface withdraws from the flow field such that solid grid points become flow grid points. Similarly, two possibilities exist where either solid points become forcing points or forcing points turn into flow points. In the former situation, the solution of the newly defined forcing points will be reconstructed and does not depend on the history value from the solid field. However, in the latter situation, the solution of new flow grid points will be solved with the Navier-Stokes equations and the terms associated with the value from previous time steps may not be correct. The reason is that these points were forcing points at time step t and the spatial derivatives were not physical since they evolved with the value from the solid field even though the velocity or pressure value was correct. To avoid contamination of the solution at these points, the field extension procedure suggested by Yang and Balaras (2006) is used. The basic idea is to extend the velocity and pressure fields to the solid field at the end of each substep. Practically, a series of pseudo fluid points in the solid field are defined to store the extended velocity and pressure field values. Similar to the procedure used to reconstruct the solution at the forcing points, the solution at the pseudo points is obtained through interpolation with surface points and virtual points along the outward normal (Fig. 3.6).

3.4 Surface force calculation

The accurate calculation of forces on the solid surface with non-body conformal grids is challenging since the lift and drag forces on the boundary depend strongly on the boundary conditions. However, the method discussed in Lai and Peskin (2000) and Balaras (2004) solves this problem in an alternative way and was shown to give very good results for the surface force. Therefore, this method was used in this study. The drag force on the immersed body arises from two components, the shear stress and pressure force. The dimensionless drag coefficient is defined as

$$C_d = \frac{F_D}{1/2\rho u_\infty^2 D}, \tag{3.41}$$

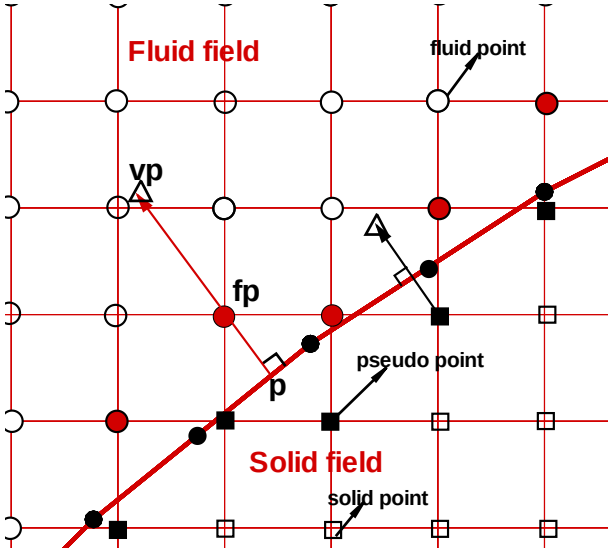

Figure 3.6 Schematic diagram of immersed boundary notation in two dimensions.

and the lift coefficient is

$$C_L = \frac{F_L}{1/2\rho u_\infty^2 D}, \tag{3.42}$$

where F_D and F_L are the drag and lift forces, respectively. D is the characteristic length of the immersed object. The drag force can be calculated by integrating the $x-$component of the force density $\mathbf{f}$ and the lift force is the result of integrating the $y-$component. As shown in Fig. 3.7, the integral form of the momentum equation on any arbitrary flow domain Ω_0 can be described by

$$\int_{\Omega_0} \frac{\partial(\rho u_i)}{\partial t} d\mathbf{x} + \int_S \rho u_i \mathbf{u} \cdot \mathbf{n} ds = -\int_{\Omega_0} p n_i d\mathbf{x} + \int_S \mu \left(\frac{\partial u_i}{\partial x_j} + \frac{\partial u_j}{\partial x_j} \right) n_j ds \tag{3.43}$$

The corresponding surface is bounded by $S = \partial\Omega_0 \cup \Gamma$, where $\partial\Omega_0$ is the outward boundary of the control volume and Γ is the surface of the immersed body. Then the force can be calculated as

$$F_i = \int_{\Omega_0} \frac{\partial(\rho u_i)}{\partial t} d\mathbf{x} + \int_{\partial\Omega_0} \left[\rho u_i u_j + p\delta_{ij} - \mu \left(\frac{\partial u_i}{\partial x_j} + \frac{\partial u_j}{\partial x_j} \right) \right] n_j ds. \tag{3.44}$$

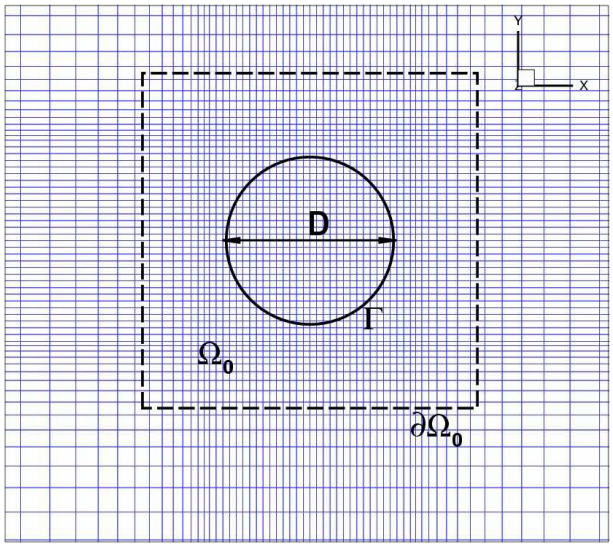

Figure 3.7 Schematic diagram of force calculation.

3.5 Parallelization

In the current code, the implicit LU-SGS scheme was implemented in each block independently. The code was parallelized by incorporating the message passing interface (MPI) libraries. The parallelization was achieved with domain decomposition utilizing the multiblock features of the code. One processor starts up initially and becomes the *parent* task. The *parent* then spawns the desired number of *child* tasks. Two approaches can be employed for message passing between blocks at the end of each iteration. For method A, or *neighbor-to-host-neighbor* message passing, each child sends data to the parent processor. Then after receiving the data, the parent processor does postprocessing of the data and sends appropriate data to each child processor. This method minimizes the number of calls to MPI routines. For method B, or *neighbor-to-neighbor* message passing, each child processor sends the appropriate data directly to other child processors that need the data. This method requires more calls to the MPI routines but minimizes the data being transmitted. For this study, the boundary data for each domain were exchanged between child processors directly with method B. The statistical data were collected in the parent processor and then scattered to each child processor.

CHAPTER 4. LARGE EDDY SIMULATION OF DUCT SUB-CHANNEL FLOWS WITH NON-BODY CONFORMAL GRIDS

4.1 Introduction

Turbulent mixing studies of complex geometry flows are critical to many engineering applications such as heat exchanger design, rod bundle flows in nuclear reactors or even turbine blade cooling. Application of large eddy simulation to industrial problems aims to capture the large turbulent structures, which often requires sufficient near wall grid resolution and good subgrid scale models (Moin, 2002). The conventional body-fitted curvilinear and unstructured grid LES solvers have been successfully applied to various flow cases such as gas-turbine combustors and asymmetric diffusers. However, the increasing geometrical complexity makes the body-fitted grid generation more challenging and proper domain decompositon is often required. The non-body conformal grid methods have been gaining popularity recently and are combined with LES solvers to solve a variety of complex turbulent flows (Balaras, 2004; Ghias et al., 2007; Tyagi and Acharya, 2005; Ikeno and Kajishima, 2006). The most prevalent approaches include the Cartesian grid method (Ye et al., 1999) and the immersed boundary method (Mohd-Yusof, 1998). Although various succssessful results have been achieved, most of them are based on incompressible flow assumptions and very few results for compressible turbulent flows have been reported.

High Reynolds number and high heat transfer rate turbulent flow in narrow gap regions can often be found in rod bundle sub-channel coolant flows of nuclear reactors. Accurate prediction of flow distribution and turbulent stresses in the coolant flow is critical for the design of safe and reliable nuclear reactors. In the literature, the general numerical simulations of turbulent flow in rod-bundle geometries often utilized Reynolds-averaged Navier-Stokes (RANS) equa-

tions and the results are observed to have limited agreement with experiments. For example, Wu (1994) performed a simulation of flow in a rod bundle contained in a trapezoidal channel with an algebraic stress model along with the $k-\epsilon$ model and found that the model was limited in predicting anisotropic turbulent structures. Lee and Jang (1997) performed numerical simulations of rod bundle flows using a nonlinear $k-\epsilon$ model and found that the model could not predict large-scale flow pulsations across the gap, in contrast with the experimental results of Hooper (1980).

Due to the limitations of RANS type simulations, large eddy simulation, which employs locally spatial averages rather than time averaging, is expected to capture the coherent turbulent structures and provide better agreement with experimental data. Biemuller et al. (1996) conducted a large eddy simulation of flow in a channel consisting of two rectangular subchannels connected by a narrow passage and their predictions of turbulent intensities were in qualitative agreement with their experiment. In a recent study (Ikeno and Kajishima, 2007), an immersed boundary method was combined with an incompressible flow solver, using a modified pressure equation based on the interpolated pressure to achieve better mass conservation near the immersed boundary. The example simulation of flow in the sub-channel with six rods equipped with spacers was conducted and the instantaneous velocity field showed that the swirling flow patterns produced by the mixing-vane arragement were reasonably captured. Although this study demonstrated the capability of the immersed boundary method in the simulation of rod bundle flows, no detailed comparisons with experimental data or other simulations were shown.

In this study, we combine a non-body conformal grid method with a compressible large eddy simulation solver (denoted as LES-IB) and simulate a rod-bundle-like flow in a duct subchannel. The ultimate goal is to simulate more complex rod bundle flows at high Reynolds numbers and high heating rates and predict the complex turbulent structures in the irregular subchannels. The computational domain is the same as that employed in Chang and Tavoularis (2005) and Guellouz and Tavoularis (2000), except that the computational domain is reduced to $L/D = 12$. To validate the code, flow over a circular cylinder is simulated for different Reynolds numbers and the results are compared with the results obtained by experiments and

simulations by body-fitted grid methods. The detailed accuracy analysis will show that the current scheme is capable of capturing the steady and unsteady features of flow over a cylinder with second-order accuracy. Then results from an LES study of a turbulent pipe flow with a moderate Reynolds number are presented and show good agreement with DNS and body-fitted grid LES data. Finally, simulation results for a high Reynolds number turbulent duct flow containing one cylindrical rod are presented. The current LES-IB simulation data provide quantitatively good agreement with experimental data especially for streamwise mean velocity and turbulent intensities.

4.1.1 Immersed boundary treatment

The basic procedure of the immersed boundary treatment is based on that stated in Chapter 3.

4.2 Results

To demonstrate the accuracy of the current non-body conformal grid method, a grid convergence study will be presented for a steady flow over a circular cylinder with $Re_D = 40$. Then the simulated results for steady and unsteady flow over cylinder with Re_D ranging from 20 to 200 will be presented and compared with experimental and simulation results obtained with body-fitted grids. To demonstrate the applicability of the current method in turbulent flow simulations, a turbulent pipe flow was simulated and the statistical results will be compared to experimental data and body-fitted grid results. Finally, the turbulent duct flow containing a cylindrical rod was simulated with the current LES-IB method. The instantaneous and statistical data will be presented and compared with experimental results (Guellouz and Tavoularis, 2000) and unsteady RANS simulation (URANS) results (Chang and Tavoularis, 2005).

4.2.1 Laminar flow over circular cylinder

4.2.1.1 Grid convergence study

To validate the overall accuracy of the current non-body conformal grid method, a grid convergence study for a steady flow over a circular cylinder with $Re_D = 40$ was carried out with different grid resolutions. It is well known that steady flow over a circular cylinder can persist up to $Re_D \approx 47$ and typically two-dimensional grids were used to simulate the steady flows. To compare with the results in the literature, a three-dimensional mesh was generated with a very thin layer in the spanwise z direction which contains only two cells. The computational domain was $[-20D, 40D]$ in the x direction and $[-20D, 20D]$ in the y direction. The center of the cylinder was located at $(x, y) = (0, 0)$. The mesh size in the z direction was set to be the same as the smallest grid size in y direction. To compare the characteristic flow parameters with those from incompressible flow solvers in the literature, the Mach number was set to be a small value, $Ma = 0.03$.

The Navier-Stokes characteristic boundary condition proposed by Thompson (1990) and Poinsot and Lele (1992) was employed at the inlet and outlet, while adiabatic free-shear wall boundary conditions were imposed at the vertical boundaries. Periodic boundary conditions were enforced in the spanwise direction. Computations were carried out on the following grids: $115 \times 75 \times 2$, $143 \times 96 \times 2$, $184 \times 120 \times 2$ and $345 \times 225 \times 2$. A hyperbolic tangent stretching function was employed in both streamwise and transverse directions to ensure that the grids were clustered toward the cylinder boundary. Figure 4.1 shows the local grid distribution near the cylinder boundary. The solutions on the coarse grids were compared with those from the finest grid and the L_2 and L_∞ norm of the error were computed in the following manner:

$$\begin{aligned} L_2 &= \left[\frac{1}{N_x N_y} \sum_{i=1}^{N_x} \sum_{j=1}^{N_y} (\phi_{i,j}^{N_x \times N_y} - \phi_{i,j}^{345 \times 225})^2 \right]^{1/2}, \\ L_\infty &= max|\phi_{i,j}^{N_x \times N_y} - \phi_{i,j}^{345 \times 225}|, \end{aligned} \tag{4.1}$$

where N_x and N_y are the total number of grid cells in x and y directions, respectively. For our analysis the error norms were computed for the x and y component of the velocity and

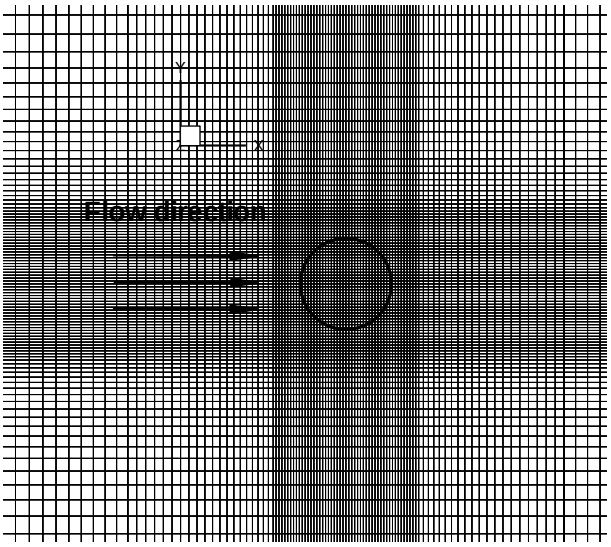

Figure 4.1 Grid distribution close to the cylinder.

Table 4.1 Drag Coefficient Comparison with Different Grid Resolutions

Grid resolution	C_d
$345 \times 225 \times 2$ (D resolved 46 points)	1.515
$184 \times 120 \times 2$ (D resolved 26 points)	1.489
$143 \times 96 \times 2$ (D resolved 20 points)	1.480
$115 \times 75 \times 2$ (D resolved 15 points)	1.463
Kim et al. (2001)	1.51
Dennis and Chang (1970)	1.52
Fornberg (1980)	1.498
Tritton (1959)(exp.)	1.49

the results are plotted with log scales in Fig. 4.2. As shown in the figure, the current scheme exhibits almost second-order convergence globally and locally.

The drag coefficient $C_d = F_d/(1/2\rho U_\infty^2 A)$ calculated from each grid resolution is compared with experimental and simulation data with body-fitted grids, as shown in Table 4.1. It is clear that as the grid is refined the drag coefficient becomes closer to the body-fitted grid results. Therefore, the convergence of the current numerical method is verified.

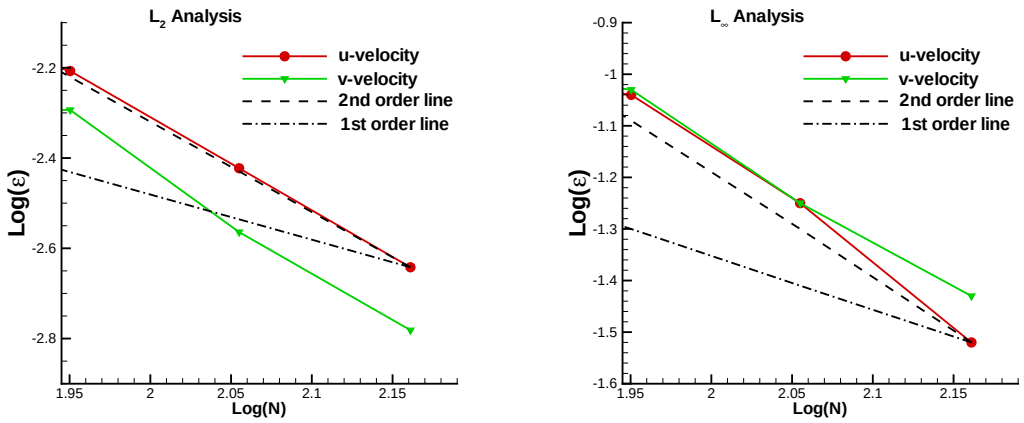

Figure 4.2 L_2 and L_∞ norm of the error for u and v velocity components (Re=40).

Table 4.2 Drag coefficient at different Reynolds numbers

C_d	Re=20	Re=40	Re=100	Re=150	Re=200
Fornberg (1980)	2.00	1.50	-	-	-
Dennis and Chang (1970)	2.05	1.52	-	-	-
Linnick and Fasel (2003)	2.06	1.54	1.34±0.009	-	1.34± 0.044
Belov et al. (1995)	-	-	-	-	1.19 ± 0.042
Rogers and Kwak, reported in (Belov et al., 1995)	-	-	-	-	1.23 ± 0.050
Palma et al. (2006)	2.05	1.55	1.32±0.01	-	1.34± 0.045
Current	2.00	1.51	1.305± 0.01	1.27± 0.02	1.25± 0.04

4.2.1.2 Steady and unsteady flows over a circular cylinder

To further validate the consistency and applicability of the current method for steady and unsteady flows, a series of cases with Reynolds number ranging from 20 to 200 were studied. All of the current computations were performed on the grid resolution $230 \times 150 \times 2$. The simulated results of drag coefficient C_d with different Re are shown in Table 4.2 and good agreement with the values reported in the literature is achieved. Figure 4.3 presents the streamline and vorticity contours for $Re = 40$. As expected from the literature, the flow is symmetric with respect to the axis of the cylinder and two shedding vortices appear downstream of the cylinder.

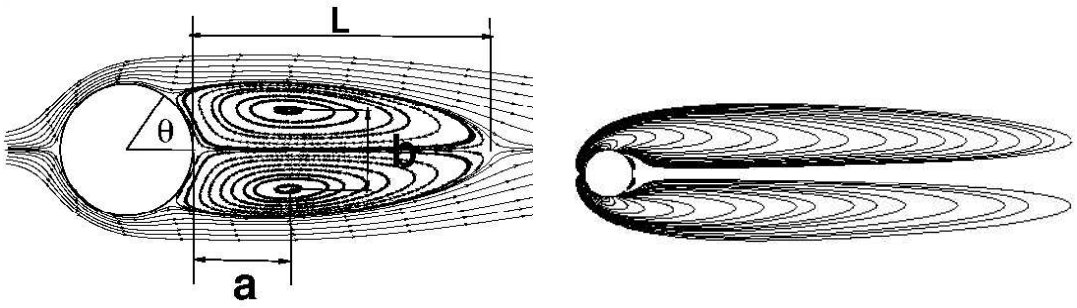

Figure 4.3 Streamlines and vorticity contours for Re=40.

Table 4.3 Geometric properties of the wake behind the cylinder($Re = 40$)

Case	L	a	b	θ	C_D
Fornberg (1980)	2.24	-	-	55.6°	1.50
Palma et al. (2006)	2.28	0.72	0.60	53.8°	1.55
Present	2.25	0.73	0.59	53.8°	1.51

The geometrical properties of the vortices behind the cylinder (Fig. 4.3) for $Re = 40$ are shown in Table 4.3, together with those obtained from body-fitted grid methods and other simulations. The current simulation results for wake length, vortex core locations and flow separation angle agree very well with other simulation results.

The pressure coefficient distribution along the cylinder surface from the finest grid resolution is presented in Fig. 4.4, together with the numerical results obtained by a body-fitted grid method. Since the grid lines do not coincide with the cylinder surface, the pressure at the surface is approximated with the cell center value of the fluid cell closest to the body. The comparison is satisfactory, within five percent difference.

For unsteady cases, $Re = 100, 150, 200$, the flow field becomes asymmetric behind the cylinder and the vortex shedding causes periodic fluctuating behavior of the drag coefficient C_d and lift coefficient C_L. Figure 4.5 presents the drag coefficients history for different Reynolds numbers. As expected from the literature, the drag coefficient decreases with respect to the increase of Reynolds number. When Reynolds number is larger than 40, the periodic fluctuating behavior of the drag coefficient is observed for all of the unsteady cases.

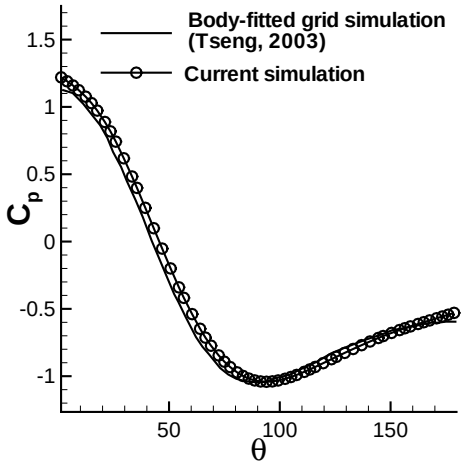

Figure 4.4 Pressure coefficient for Re=40.

Figure 4.6 shows the lift coefficient history for these different Reynolds numbers. As shown in the figure, the amplitude of the fluctuating lift coefficient and the fluctuation frequency increase with increasing Re. The Strouhal numbers $St = fd/U_\infty$ are shown in Table 4.4 and it is clear that the results of the current simulation agree with those reported in the literature very well for the several Reynolds numbers.

Table 4.4 Strouhal number comparison

Re	Silva et al. (2003)	Williamson (1996)	Current
100	0.16	0.166	0.166
150	0.18	0.183	0.182
200	-	0.193	0.196

Finally, Fig. 4.7 presents the normalized pressure contours $2(p - p_\infty)/(\rho_\infty U_\infty^2)$ for different Reynolds numbers. As expected, the pressure reaches maximum values at the stagnation point on the cylinder and minimum values in the wake region. The periodic behaviors of the pressure contours for the unsteady cases are consistent with those observed in the drag and lift coefficients history. Therefore, the major characteristics of steady and unsteady flow over a circular cylinder are well captured with the current numerical method.

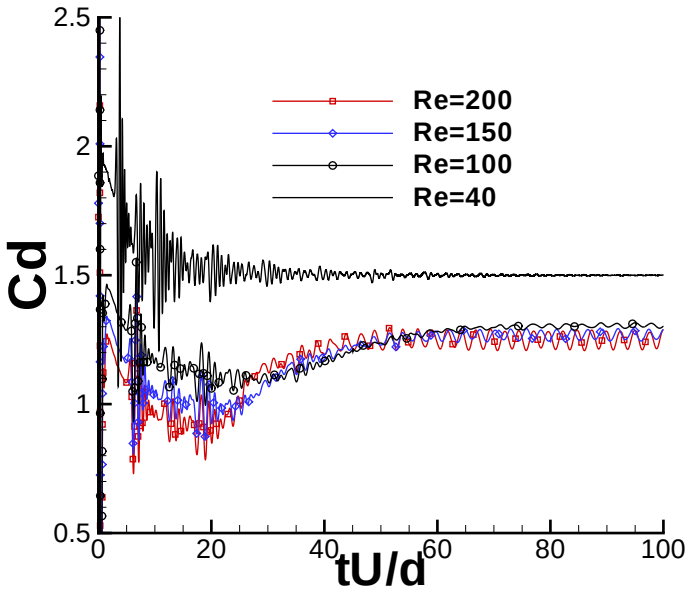

Figure 4.5 Drag coefficient history for $Re = 40, 100, 150, 200$.

4.2.2 Turbulent pipe flow

The simulation of turbulent pipe flow was designed to validate the performance of the current numerical method for turbulent flow computations. The results of the current LES-IB simulations are compared with DNS data (Eggles et al., 1994) and an LES simulation (Xu and Pletcher, 2005) with body-fitted grids.

4.2.2.1 Simulation details

A fully developed turbulent pipe flow was simulated and the computational domain was set as $L = 5D$, same as that in Eggles et al. (1994) and Xu and Pletcher (2005). The target bulk Reynolds number $Re_b = \frac{\rho_b u_b D}{\mu_b}$ was 5300. The boundary condition along the immersed pipe wall was no-slip, isothermal. Step periodic boundary condition were used in the streamwise direction. The initial flow field was constructed by superimposing random velocity fluctuations on a parabolic velocity profile. The magnitude of the fluctuation was around 10% of the mean velocity. The Mach number was 0.001 and the non-dimensional physical time step was set as

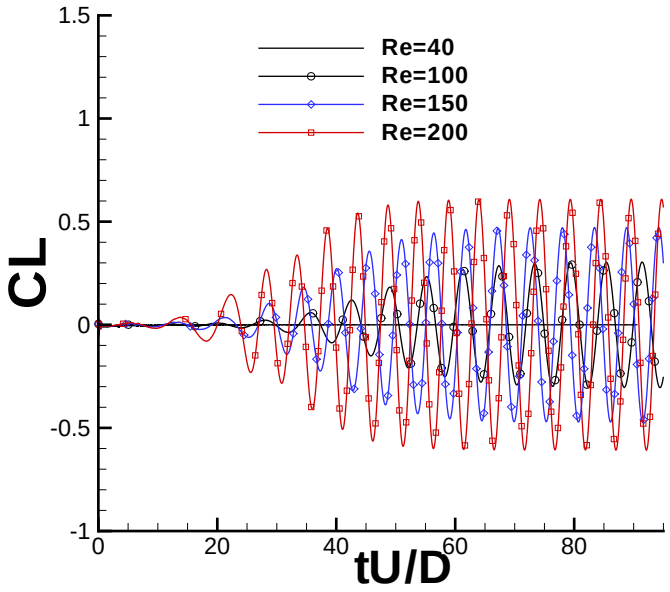

Figure 4.6 Lift coefficient for $Re = 40, 100, 150, 200$.

0.01 to satisfy the CFL stability condition. Two smaller time steps, 0.005 and 0.001, were also tested, in which the time-averaged statistical results were essentially the same as those with time step 0.01.

Grid independent studies were conducted on grid resolutions $60 \times 80 \times 80$ (case 1), $100 \times 108 \times 108$ (case 2), $128 \times 136 \times 136$ (case 3) and $160 \times 170 \times 170$ (case 4). A hyperbolic stretching function was employed for all cases so that the grids were clustered towards the wall boundary. It was shown that the velocity profile in wall units predicted by the $128 \times 136 \times 136$ grid was in good agreement with the universal law of the wall within the viscous sublayer and logarithmic layer. Also the mean friction coefficient predicted with the $128 \times 136 \times 136$ grid agreed well with DNS and experimental data, while the results from coarser grids were underpredicted. Therefore, the $128 \times 136 \times 136$ grid was adopted for the computations and compared with the DNS and experimental data.

The computational domain and grid topology are shown in Fig. 4.8. As shown in the figure, grids were uniform in the streamwise direction and stretched in the y and z directions. The grid resolution in terms of wall units is listed in Table 4.5, where the definition of wall

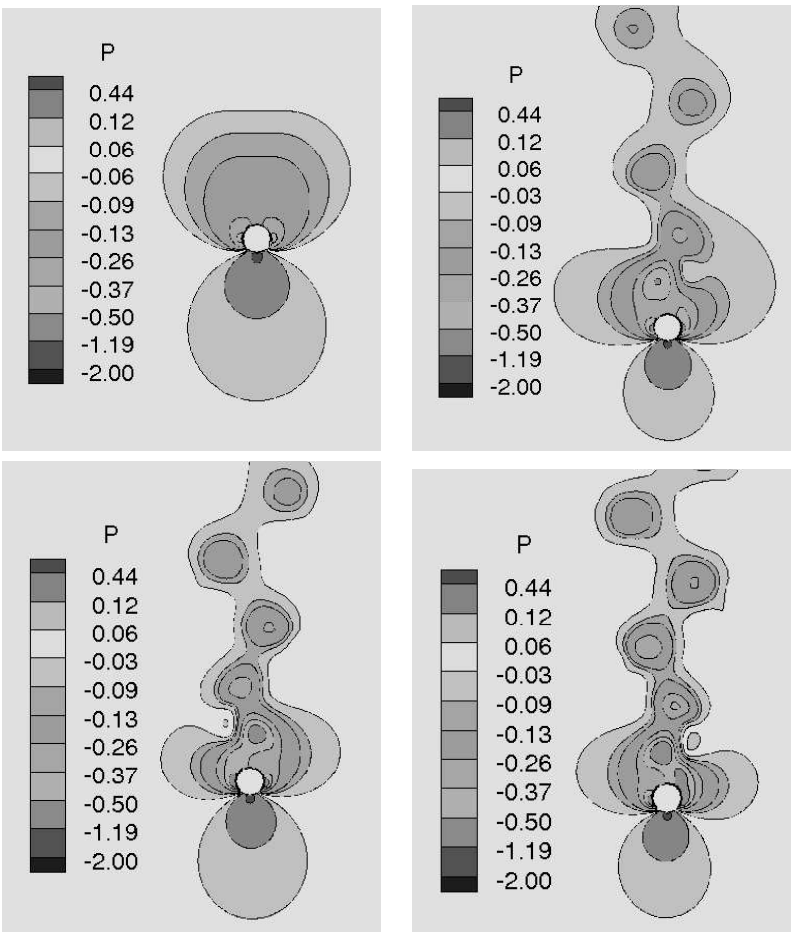

Figure 4.7 Pressure contours for $Re = 40, 100, 150, 200$, where flow direction is from bottom to top.

coordinates is: $x^+ = u_\tau x/\nu_w$ and $y^+ = u_\tau y/\nu_w$. Mean flow properties of the current LES-IB simulation are compared with those from LES of body-fitted grids (denoted as "LES"), DNS and PIV in Table 4.6.

As shown in the table, the friction velocity, u_τ, from two coarse grids is underpredicted, while the agreement between the result of the fine grid LES-IB and that from LES, DNS and PIV is within a few percent.

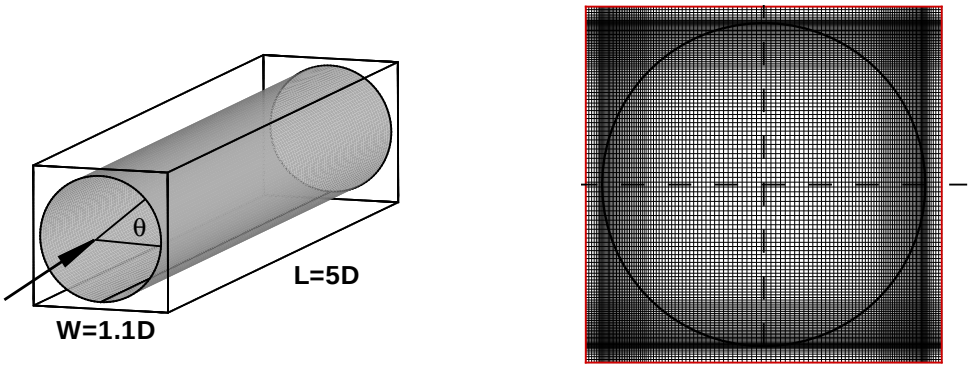

(a) (b)

Figure 4.8 (a) computational domain; (b) cross section grid distribution with $128 \times 136 \times 136$.

Table 4.5 Pipe flow: grid resolution in wall units

Grid	Streamwise		Normal to the wall $\theta = 0°$ or $\theta = 90°$			
	Δx	Δx^+	Δy_{min}	Δy^+_{min}	Δy_{max}	Δy^+_{max}
case 1	0.125	24.20	0.0055	1.065	0.0335	6.487
case 2	0.1	21.61	0.0033	0.713	0.0268	5.790
case 3	0.075	14.79	0.00323	0.637	0.0234	4.618

4.2.2.2 Mean flow and velocity statistics

To validate the turbulent statistical results obtained with the current LES-IB method, the simulation results are compared with those from LES, DNS and PIV experiments. The mean quantities $\langle \cdot \rangle$ were obtained by averaging in the homogeneous directions (streamwise direction here) and in time for $4t^* = 4D/u_\tau$ after the flow was fully developed. Figure 4.9 shows the mean streamwise velocity normalized by the friction velocity along the directions with $\theta = 0°$, $90°$, $45°$ and $135°$. The mean velocity profile was normalized by the friction velocity as $U^+ = U/u_\tau$. In all four directions, the velocity profiles show good agreement with the DNS data (Eggles et al., 1994) as well as the universal law of the wall in both viscous sublayer and log-law layer. The slight difference between the profile in the direction perpendicular to the grid with that

Table 4.6 Pipe mean flow properties

	LES-IB (case 1)	LES-IB (case 2)	LES-IB (case 3)	LES	DNS	PIV
$Re_\tau = \frac{u_\tau D}{\nu}$	345	353	365	356	360	366
$\frac{u_b}{u_\tau}$	16.3	15.56	14.50	14.86	14.73	14.88
$\frac{u_c}{u_\tau}$	20.02	19.58	18.98	19.14	19.31	19.38

in the diagonal direction indicates the effect of the current grid. In the directions $\theta = 0°$ and $\theta = 90°$, the grids are aligned with the wall normal direction and the smallest grid element near the wall has the property $y^+_{(1)} < 1$. Therefore, there are around eight points located within the region with $y^+ < 10$. On the other hand, in the directions $\theta = 45°$ and $\theta = 135°$, since the grids are not aligned with wall normal direction, the grid stretching function has a less significant effect. As shown in Fig. 4.9, the first grid away from the wall is $y^+_{(1)} \approx 2.2$ and there are only around three grid points within the region with $y^+ < 10$.

The turbulent intensity plots in each direction are shown in Fig. 4.10, together with the DNS results. The root mean square(rms) values were obtained by operations such as $u_{rms} = \sqrt{\langle u'u' \rangle}$, where $u' = u - \langle u \rangle$ and $\langle \cdot \rangle$ denotes the ensemble average in the homogeneous $x-$direction and in time. Then the rms values were normalized with u_τ. As the figure shows, the three components of turbulent intensities u_{rms}, u_{rrms} and $u_{\theta rms}$ reach a maximum at a location near the pipe wall and a minimum in the central region of the pipe. Although the u_{rrms} and $u_{\theta rms}$ components of the turbulent intensities are slightly different from the DNS value, the streamwise component agrees well with the DNS data. Specifically, by taking the circumferential average for each component, the magnitude and location of these maximum and minimum values for each component are well captured as shown in Fig. 4.11.

4.2.2.3 Friction coefficient

In Table 4.7, the average friction coefficients calculated from the three grid resolutions are compared to DNS results, experimental data and empirical correlations. The friction coefficient is defined as

$$C_f = f = \frac{\tau_w}{1/2\rho_b U_b^2}. \tag{4.2}$$

In the table, the difference between LES-IB simulation results and DNS, experimental data or correlations, $Diff$, is defined as

$$Diff = \frac{\text{DNS simulation result} - \text{Comparison data}}{\text{DNS simulation result}}. \tag{4.3}$$

It can be observed that both coarse grids resulted in underprediction of the friction coefficient. Excellent agreement with DNS and experimental data is obtained for the fine grid case, and also good agreement is observed when compared with the correlation.

Table 4.7 Pipe flow: friction factor comparison

Correlation	C_f	Diff.(%)
Present simulation $60 \times 80 \times 80$	0.0084	-8.89
Present simulation $100 \times 108 \times 108$	0.0089	-3.47
Present simulation $128 \times 136 \times 136$	0.00925	+0.33
DNS (Eggles et al., 1994)	0.00922	-
Blasius Law $C_f = 0.079 Re_D^{-1/4}$	0.00926	+0.43
PIV	0.00903	-2.06

4.2.3 Turbulent duct flow containing a cylindrical rod

To evaluate the performance of the current LES-IB method in the simulation of turbulent flows in complex geometries, flow through the subchannel of a rectangular duct containing a cylindrical rod was simulated and compared with existing experimental and unsteady RANS data. As shown by Guellouz and Tavoularis (2000), with the pitch to diameter ratio $W/D = 1.1$ used in the current study, the two-point velocity fluctuation correlations for streamwise and spanwise component are close to zero for $x/D \approx 6$. Therefore, it is reasonable to use $L = 12D$ as the computational domain. Similar to Guellouz and Tavoularis (2000), the diameter of the rod D is chosen to be the reference length scale, and the computational domain is $12D \times 2D \times 3D$ in the streamwise, transverse and spanwise directions, respectively. As shown in Fig. 4.12, the rod is placed close to the bottom wall with the gap region $\delta = 0.1D$.

The bulk Reynolds number, based on the hydraulic diameter D_h is 108,000, where $D_h \approx 1.59D$. Grid independence studies were carried out with four meshes, $110 \times 126 \times 170$ (case 1), $135 \times 150 \times 220$ (case 2), $165 \times 186 \times 272$ (case 3) and $165 \times 220 \times 324$ (case 4) in the

streamwise, transverse and spanwise directions, respectively. Similar to the turbulent pipe flow simulations, all grids were uniformly spaced in the x direction and stretched towards the duct wall boundaries with a hyperbolic tangent stretching function. It was shown that the average friction coefficient predicted with the $165 \times 186 \times 272$ grid was essentially very close to that calculated with the $165 \times 220 \times 324$ grid. Therefore the $165 \times 186 \times 272$ grid was adopted for the further computations. The grid properties in wall units are shown in Table 4.8.

Table 4.8 Duct flow with one rod: grid resolution in wall units

Grid	Streamwise		Transverse				Spanwise			
	Δx	Δx^+	Δy_{min}	Δy^+_{min}	Δy_{max}	Δy^+_{max}	Δz_{min}	Δz^+_{min}	Δz_{max}	Δz^+_{max}
case 1	0.1	241.06	0.000962	2.319	0.0186	44.99	0.00067	1.624	0.0177	42.755
case 2	0.081	205.45	0.000343	0.870	0.0143	36.45	0.00049	1.262	0.0142	36.158
case 3	0.067	174.00	0.00034	0.883	0.0126	32.49	0.00029	0.758	0.0125	32.289

The wall unit is defined as $x^+ = \frac{xu_\tau}{\nu_w}$, where the friction velocity is $u_\tau = \sqrt{\tau_w/\rho_w}$. The initial flow field was constructed with a laminar Poiseuille profile sheared along the $y-$ and $z-$ directions respectively. A white noise of amplitude $A \sim 5\%U_b$ was superimposed on the mean velocity. A uniform pressure and temperature distribution was applied. The boundary conditions at the duct walls were no-slip, isothermal. Step periodic boundary conditions were used in the streamwise direction. The statistics was collected when a fully developed turbulent flow was obtained.

4.2.3.1 Velocity statistics

The velocity statistics are compared to unsteady RANS (URANS) results (Chang and Tavoularis, 2005) and the experimental results (Guellouz and Tavoularis, 2000). In the current LES-IB simulation, the flow statistics were collected over 30 time units t^* ($t^* = D_h/U_b$). Figure 4.13 presents axial mean velocities at the middle plane of the duct $z/D = 0$ near the top and bottom walls. In Fig. 4.13(a) the mean velocity is normalized by the average friction velocity along all duct walls, while in Fig. 4.13(b) it is normalized by the local friction velocity u^{loc}_τ. The dashed line represents the empirical viscous linear sublayer $U^+ = y^+$ and the solid line is the log-law profile $U^+ = \frac{1}{\kappa}\ln y^+ + 5.5$ with von Kármán constant $\kappa = 0.4$. As shown in Fig.

4.13(a), the resulting value normalized by average friction velocity is underpredicted for the velocity near the bottom wall, while overpredicted for the velocity near the top wall. With the normalization factor changed to the local friction velocity, the mean profile near both the top and bottom walls becomes much closer to the log-law line. The significantly different mean profiles between (a) and (b) demonstrate that for the current geometry, where the flow near the bottom duct wall has been significantly modified by the rod, the local wall unit should be used for normalization. In Fig. 4.13(b), the different velocity distribution near the bottom and top walls indicates that the friction velocity at the center of the bottom wall is significantly smaller than that at the top wall. This is reasonable since at the narrow gap between the rod and the bottom wall, the mean velocity becomes significantly smaller than that in the open channel center and the flow tends to be laminarized in the gap region.

Figure 4.14 shows the time-averaged streamwise velocity contours in a cross section of the duct, together with the results obtained from experiment (Guellouz and Tavoularis, 2000). It can be observed from both experiment and the current LES-IB simulation that two maxima are located in the two open subchannels, half way between the symmetry plane and the side walls. While in the URANS simulation the maximum velocity is located on the symmetry plane above the rod (Chang and Tavoularis, 2005). It was also observed from the current simulation that, before a fully developed flow was achieved, the maximum velocity appeared on the symmetry plane above the rod, similar to the the patterns in the URANS simulation.

4.2.3.2 Turbulent intensities and Reynolds stresses

The LES-IB results of the turbulent intensity and turbulent kinetic energy contour plots are presented in Figs. 4.15, 4.16, 4.17 and Fig. 4.18, respectively, and compared with experiments. The root mean square (rms) values were obtained by operations such as $u_{rms} = \sqrt{\langle u'u' \rangle}$, where $u' = u - \langle u \rangle$ and $\langle \cdot \rangle$ denotes the ensemble average in the homogeneous direction and in time. Then the rms values were normalized with U_b and turbulent kinetic energy was normzlized with U_b^2.

As shown in the figure, the increasing magnitudes towards the corners of the isocontours

of the three rms velocity fluctuations and turbulent kinetic energy was quite pronounced and consistent with the formation of secondary flows near the corners such as those in the duct flows. However, the intensities and kinetic energy isocontour shapes in the lower section of the duct are significantly different from those observed in duct flows due to the existence of a narrow gap region.

Figure 4.19 presents isocontours of the axial u' and azimuthal u'_φ turbulent intensities in the gap region together with the experimental results. It can be observed that the axial turbulent intensity reaches high levels near both duct and rod walls. However, the local maxima of axial turbulent intensity between the bottom wall and the rod, shown in the experimental results, is not observed in the current LES-IB simulation. The possible reason for this difference is that the grid resolution near the rod wall is too coarse. On the other hand, the local distribution of azimuthal turbulent intensity u'_φ in the gap region shows good agreement with the experimental result. As shown in Fig. 4.19, u'_φ reaches the maxima on the plane of symmetry, approximately the center of the gap region.

The turbulent shear stresses, isocontours and the corresponding correlation coefficients are presented in Fig. 4.20, together with the experimental results (Guellouz and Tavoularis, 2000). All stresses are normalized by U_b^2. Near the plane walls and away from the gap, the three turbulent shear stresses have variations that are compatible with wall turbulence. In particular, the magnitudes of $\overline{uv}$ and $\overline{uw}$ increase towards the wall and their contours become nearly parallel to, respectively, the top and side walls of the channel, following the direction of the mean velocity gradient in the corresponding wall regions. The signs of these stresses are opposite to the sign of the local mean velocity gradient, consistent with the "gradient transport" concept.

Midway in the region between the duct wall and rod wall, the magnitude of the stresses $\overline{uv}$ and $\overline{uw}$ become significantly small and switch signs as they pass the midway region and move towards the walls. Near the gap region, both the stresses $\overline{uv}$ and $\overline{uw}$ show local maxima but the local maxima are slightly less than those at the location near the top and side wall, respectively. The contour plot of $\overline{vw}$ is slightly different from the experimental results but

has good agreement with the URANS simulation results (Chang and Tavoularis, 2005). In both LES-IB and URANS simulations, the $\overline{vw}$ contours have an approximately antisymmetric behavior with respect to the horizontal axis of the rod with opposite signs. The contours of the three shear stress correlation coefficients are similar to the contours of the corresponding turbulent shear stresses.

4.2.3.3 Wall shear stresses and friction factor

The variations of the mean skin friction coefficient, $C_f = \tau_w/(1/2\rho U_b^2)$ is not easy to evaluate for the current complex geometry flow. Based on the author's knowledge, there are no universal correlations for the calculation of friction coefficients in rod sub-channel flows. In the current study, the averaged friction coefficient along the four duct walls was computed and compared with an empirical correlation for duct flows obtained by Jones (1976):

$$\frac{1}{C_f^{1/2}} = 4\log_{10}(2.25Re_b C_f{}^{\frac{1}{2}}) - 1.6. \tag{4.4}$$

The C_f value calculated from the correlation is 0.00432, which is close to the LES-IB simulated result 0.00429.

The local wall shear stress is normalized by the averaged wall shear stress τ_a and it exhibits local maxima around $z/D_h = 0.2$ and $z/D_h = 0.5$. The maximum located at the wall midpoint can be easily understood since the velocity gradient is large there. The other local maximum appears at the position of the secondary flow impingment, which can be explained by the fact that the impingement brings high-speed fluid from the duct center to the wall which results in a higher velocity gradient. The local minima located between these two maxima can be explained as due to the secondary flow ejection, which brings fluid away from the wall. It can be observed that the results are very sensitive to the Reynolds number. For the low Reynolds number case, the difference between the local maximum and the local minimum in between is larger than that observed for the high Reynolds number case.

4.2.3.4 Comparison with turbulence in pipes or ducts

Away from the rod, the mean isocontours follow patterns comparable to those in square duct flows (Qin, 2007). This was also the case for the rms axial turbulent velocity. In the present case, the values of the transverse rms velocity close to the top duct wall are comparable to the values of the spanwise rms velocity close to the side wall, and vice versa. Away from the top corner, the shapes of the contours are measurably different. These differences can be attributed to the asymmetry of the rectangular duct with respect to the corner bisector, and also to the presence of the rod, which introduces additional geometrical asymmetry. This effect is more significant near the gap region, which was influenced more by the presence of the rod.

Prefect symmetry requires that the $\overline{uv}$ and $\overline{uw}$ turbulent shear stresses should be equal in magnitude and opposite in sign at points symmetrically located with respect to the corner bisector. Close to the top and side walls of the duct, isocontours of the three turbulent shear stresses are similar to those in square ducts. The effects of secondary flows are clearly noticable in the contour plots with increasing values toward the corners of the duct. Similar to the experimental results, the corresponding correlation coefficients have magnitudes comparable to those in circular pipe flows, i.e., near 0.4 for $\overline{uv}/u'v'$ and $\overline{uw}/u'w'$ in the vicinity of, respectively, the top and side walls. The third correlation coefficient, $\overline{vw}/v'w'$ is essentially zero close to the duct walls. However, towards the rod wall, the magnitude of $\overline{vw}/v'w'$ reaches a maxima, around 0.55 near the bottom half wall and -0.3 near the top half wall. A similar distribution was also observed in the experimental results (Guellouz and Tavoularis, 2000).

In the vicinity of the rod-wall gap, the local maximum of the turbulent intensity isocontours near the rod wall was also observed in the experiments of subchannels of rod bundles (Rehme, 1989). Away from the gap, the rather open aspect of the present duct results in a distribution similar to those found in duct flows. In the gap region, in contrast to the remainder of the duct, the partition of the turbulent kinetic energy to its components $\overline{u^2}, \overline{v^2}, \overline{w^2}$ is significantly different from that in duct flows. For the normal duct or pipe flows away from the walls, the axial normal stress contains approximately half of the total energy, while the other two components account for approximately one quarter each. With the presence of the rod, the $\overline{u^2}$

and $\overline{w^2}$ stresses at the gap center have comparable contributions, while $\overline{v^2}$ almost vanished. The time averaged values at $z/D = 0$ is $\overline{u^2}/2k = 0.447$, $\overline{v^2}/2k = 0.055$ and $\overline{w^2}/2k = 0.498$. These values match those measured by Guellouz and Tavoularis (2000): $\overline{u^2}/2k = 0.44$, $\overline{v^2}/2k = 0.07$ and $\overline{w^2}/2k = 0.49$.

4.3 Conclusions

A non-body conformal grid method was incorporated into a large eddy simulation solver to simulate geometrically complex turbulent flows. The scheme was developed based on the fixed Cartesian grids which significantly simplifies the grid generation procedure. Flow over a cylinder with different Reynolds numbers was simulated using the methodology developed to validate the numerical scheme. The accuracy study showed that the current scheme is second order accurate. The drag coefficient study with $Re = 40$ showed the convergence of the current scheme and the drag and lift coefficients study with different Reynolds numbers showed the consistency of the current scheme in simulating unsteady flow. Also, the pressure contours and pressure coefficients show good agreement with the results in the literature.

The turbulent pipe flow simulation with the current LES-IB method demonstrated its capability for simulating turbulent flows with non-body conformal grids. The mean axial velocity profiles along $\theta = 0°, 90°, 45°, 135°$ directions agree very well with the DNS data and empirical laws of the wall. The turbulent intensites along each direction display a reasonably good agreement with the DNS profiles. Specifically, after further averaging in the azimuthal direction, the turbulent intensities show a better agreement with the DNS data. It is expected that the turbulent intensity simulation results can be improved by refining the mesh and decreasing the skewness of the grids.

For the first time, a turbulent duct flow containing a cylindrical rod was simulated with the current non-body conformal grid method. The turbulent statistical results show good agreement with the experimental data. It was shown that the current LES-IB simulation provides better axial mean velocity and turbulent intensity distributions, compared to URANS simulation results. The possible reason is that the LES simulation is able to capture the

turbulent structures better than RANS type simulations. Also, the other turbulent statistics such as Reynolds stresses and stress correlation coefficients displayed a qualitatively good agreement with experimental data. Since the current simulation represents a simplified rod-bundle-like flow, the outlook is very promising for the extension of the LES-IB method to simulate more complex rod-bundles flows. Also, the current simulation can be extended to cases with significant heat transfer as in practical nuclear reactor cooling flows around rod bundles.

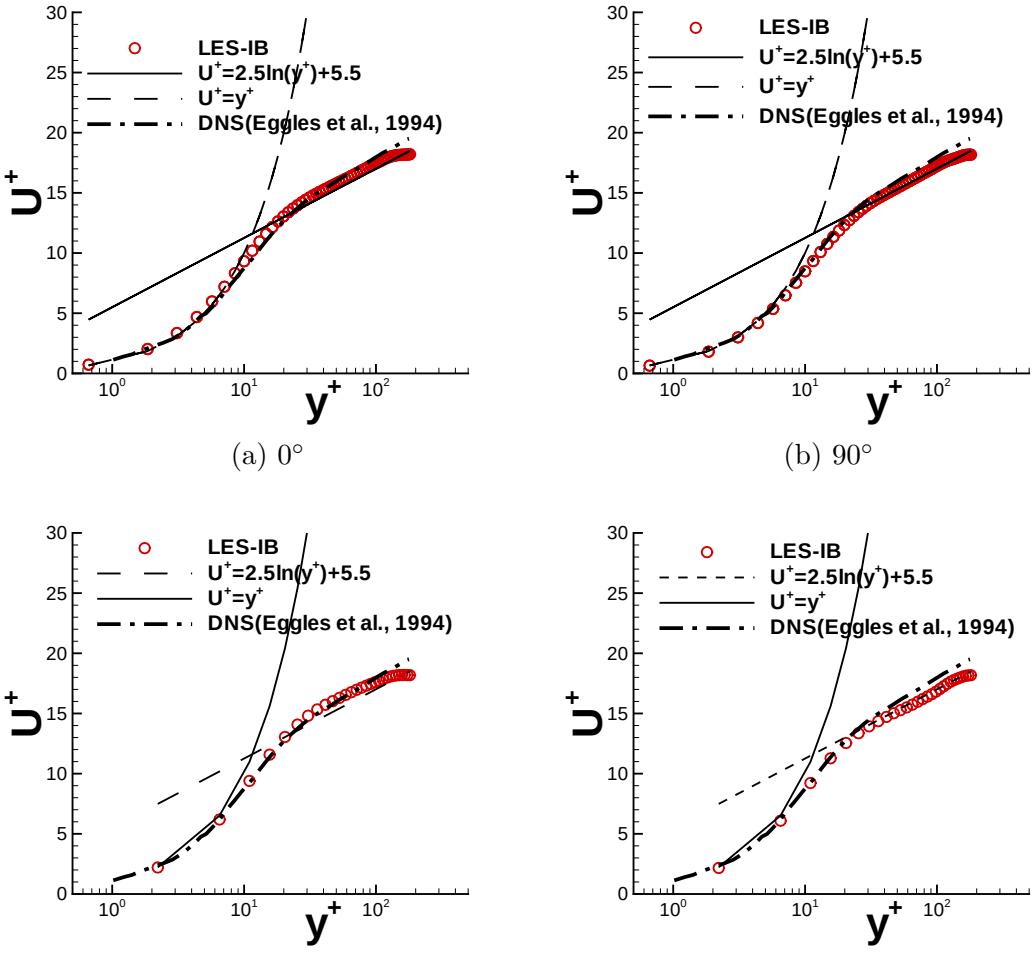

(a) 0° (b) 90°

(c) 45° (d) 135°

Figure 4.9 Streamwise mean velocity at each direction: comparison with DNS.

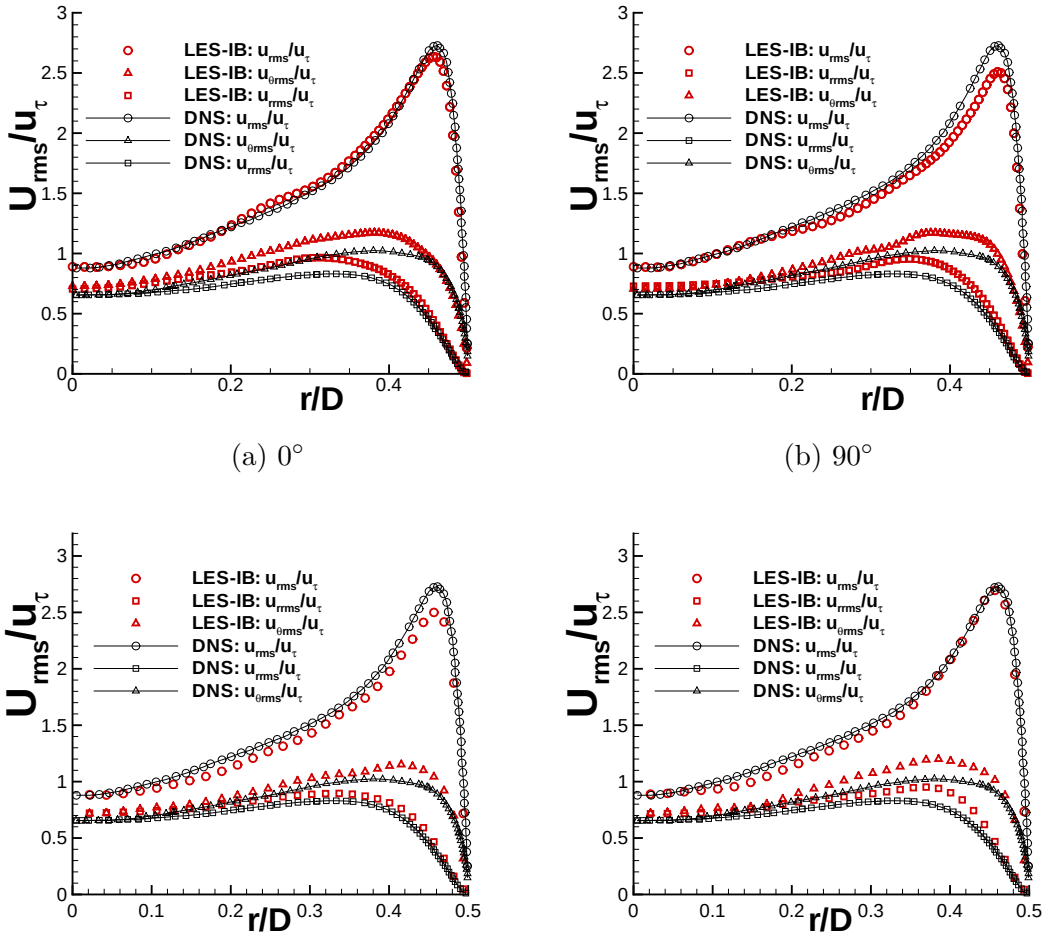

(a) 0°

(b) 90°

(c) 45°

(d) 135°

Figure 4.10 Turbulent intensities in each directions: comparison with DNS.

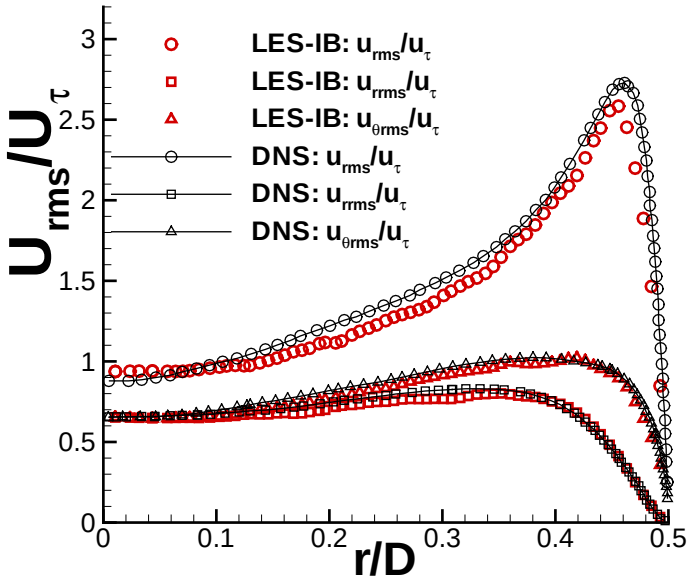

Figure 4.11 Averaged turbulent intensities: comparison with DNS.

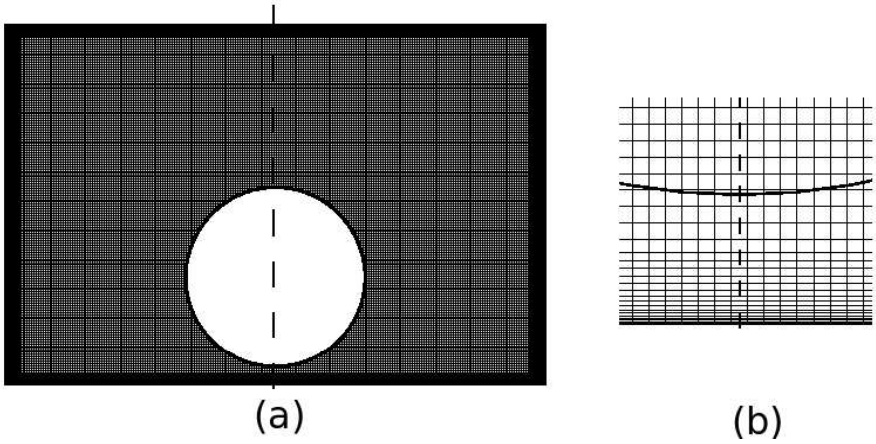

Figure 4.12 (a) Computational domain and grids, flow direction is towards the paper; (b) Local grid resolution within the gap region.

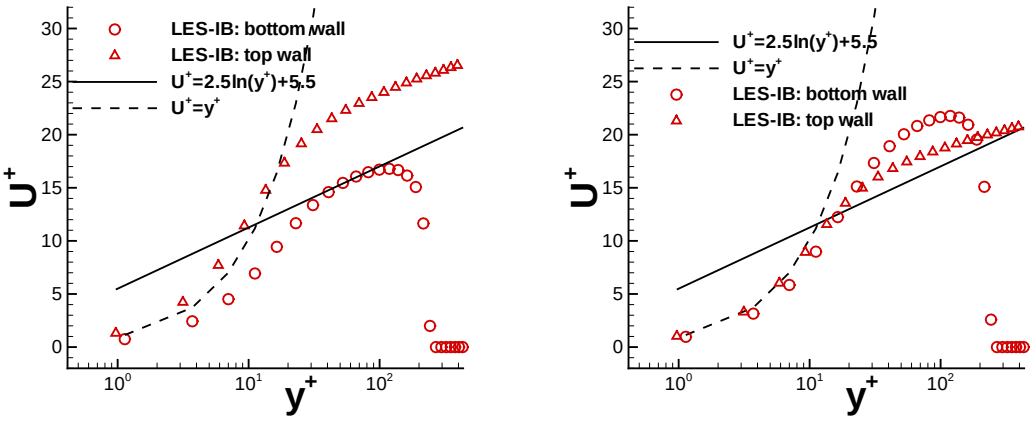

Figure 4.13 (a) Axial mean velocity in wall units with average $u_\tau(z/D = 0)$; (b) Axial mean velocity in wall units with u_τ^{loc} $(z/D = 0)$.

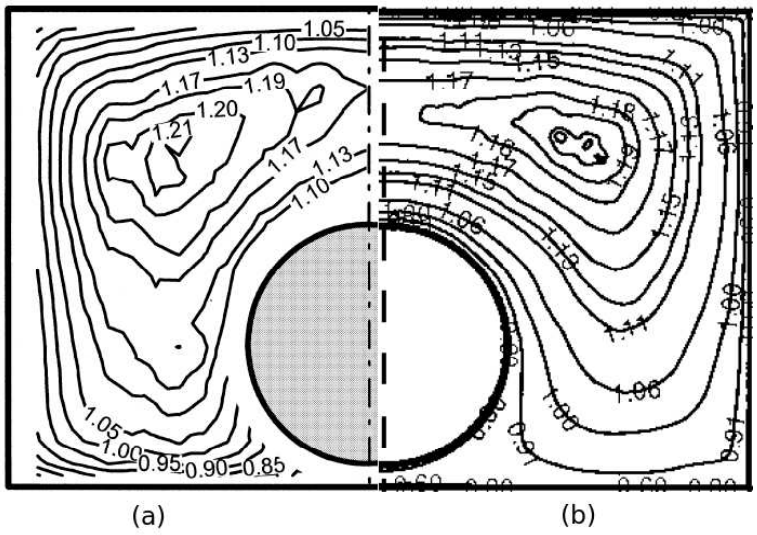

Figure 4.14 Streamwise mean velocity contours: (a) Experimental results (Guellouz and Tavoularis, 2000); (b) Current simulation results.

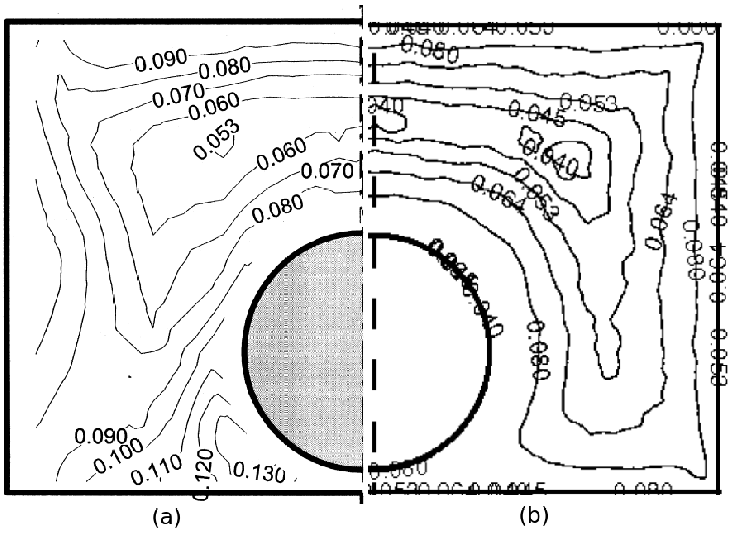

Figure 4.15 Turbulent intensities: (a) Experimental (Guellouz and Tavoularis, 2000): u_{rms}/U_b; (b) LES-IB: u_{rms}/U_b.

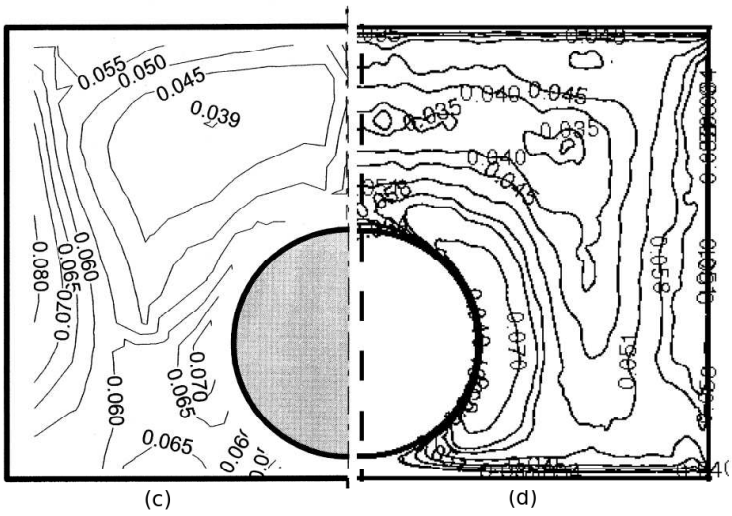

Figure 4.16 Turbulent intensities: (c) Experimental (Guellouz and Tavoularis, 2000): v_{rms}/U_b; (d) LES-IB: v_{rms}/U_b.

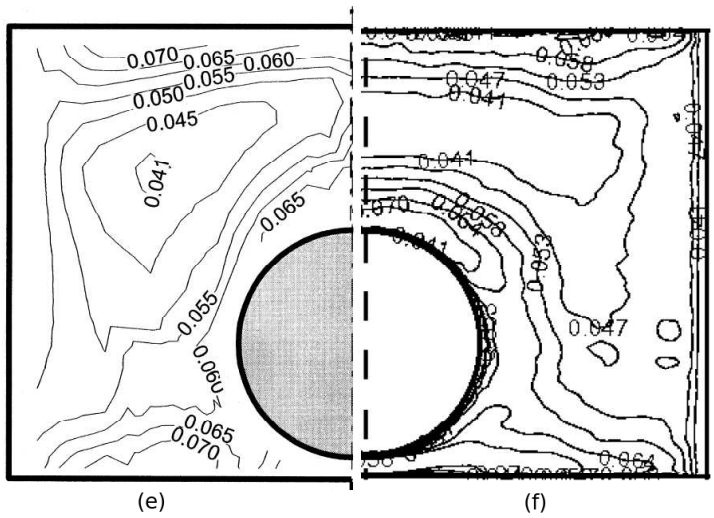

Figure 4.17 Turbulent intensities: (e) Experimental (Guellouz and Tavoularis, 2000): w_{rms}/U_b; (f) LES-IB: w_{rms}/U_b.

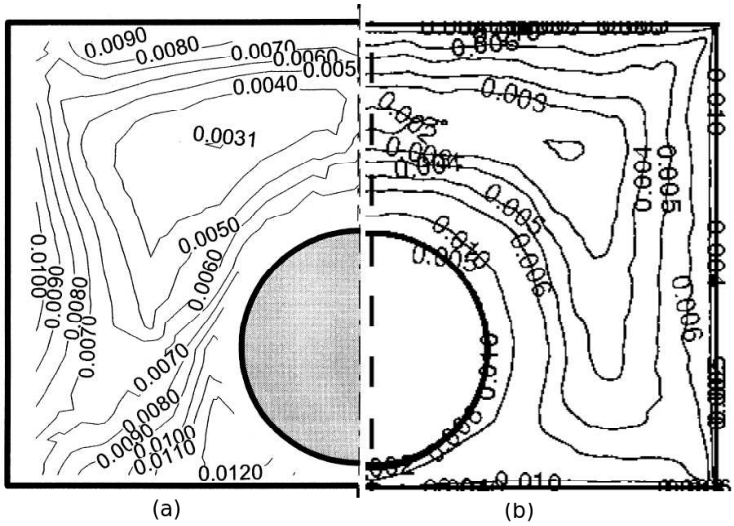

Figure 4.18 Turbulent kinetic energy: (a) Experimental (Guellouz and Tavoularis, 2000): k/U_b^2; (b) LES-IB: k/U_b^2.

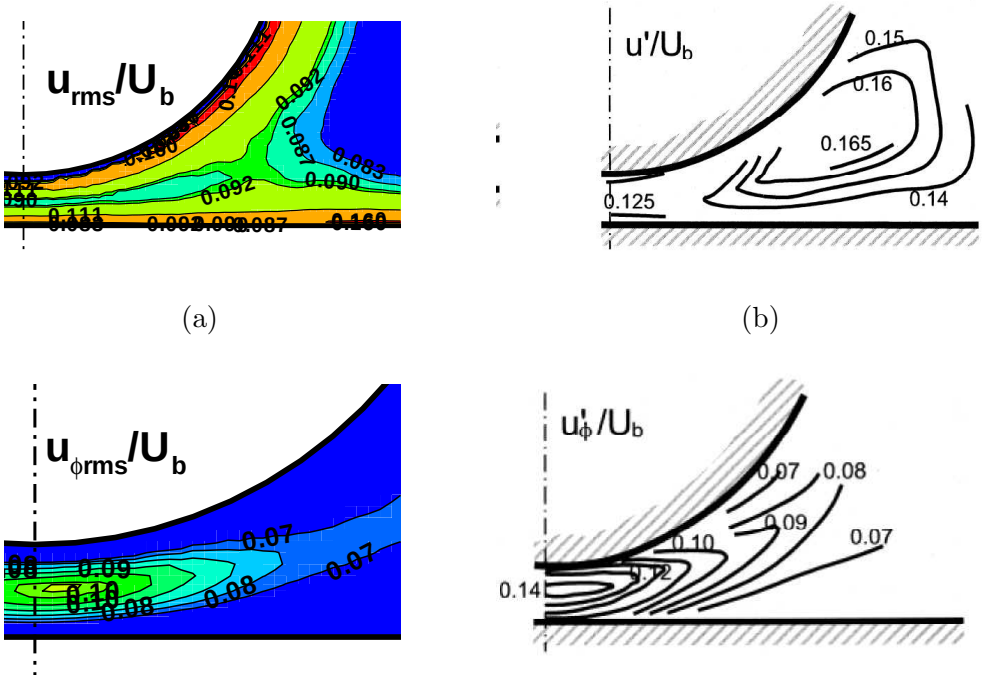

(a) (b)

(c) (d)

Figure 4.19 Turbulent intensities near the gap region (Experimental(Guellouz and Tavoularis, 2000)): (a) LES-IB: streamwise turbulent intensity; (b) Experimental: Streamwise turbulent intensity; (c) LES-IB: Azimuthal turbulent intensity; (d) Experimental: Azimuthal turbulent intensity.

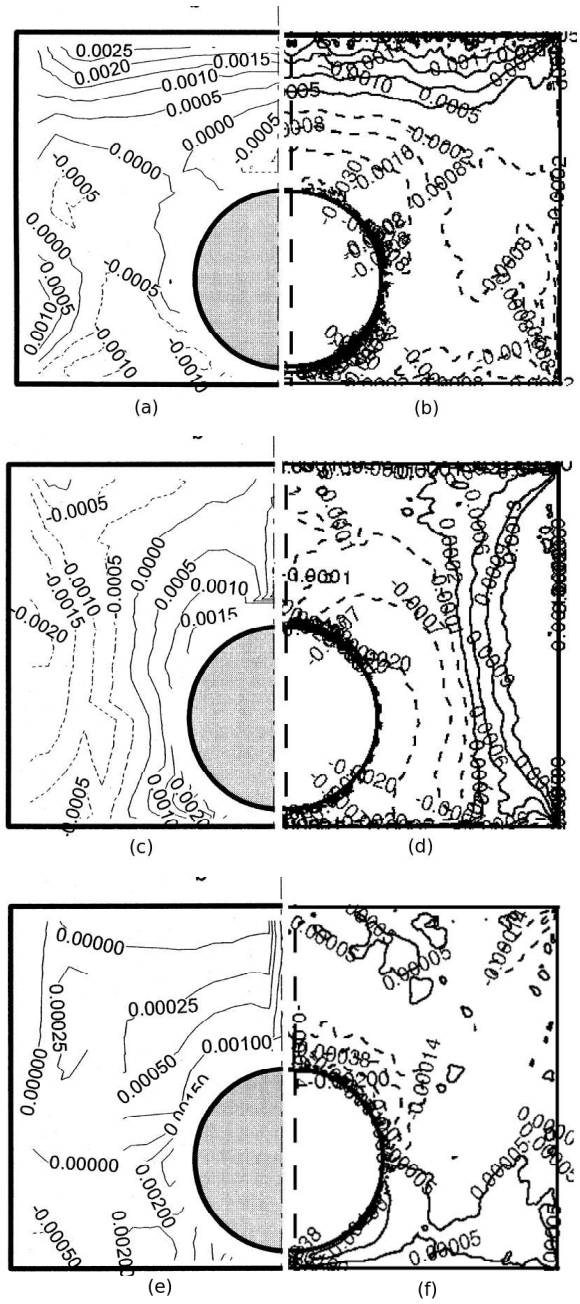

Figure 4.20 Turbulent shear stress contours (Experimental (Guellouz and Tavoularis, 2000)): (a) Experimental: $\langle uv \rangle / U_b^2$; (b) LES-IB: $\langle uv \rangle / U_b^2$; (c) Experimental: $\langle uw \rangle / U_b^2$; (d) LES-IB: $\langle uw \rangle / U_b^2$; (e) Experimental: $\langle vw \rangle / U_b^2$; (f) LES-IB: $\langle vw \rangle / U_b^2$.

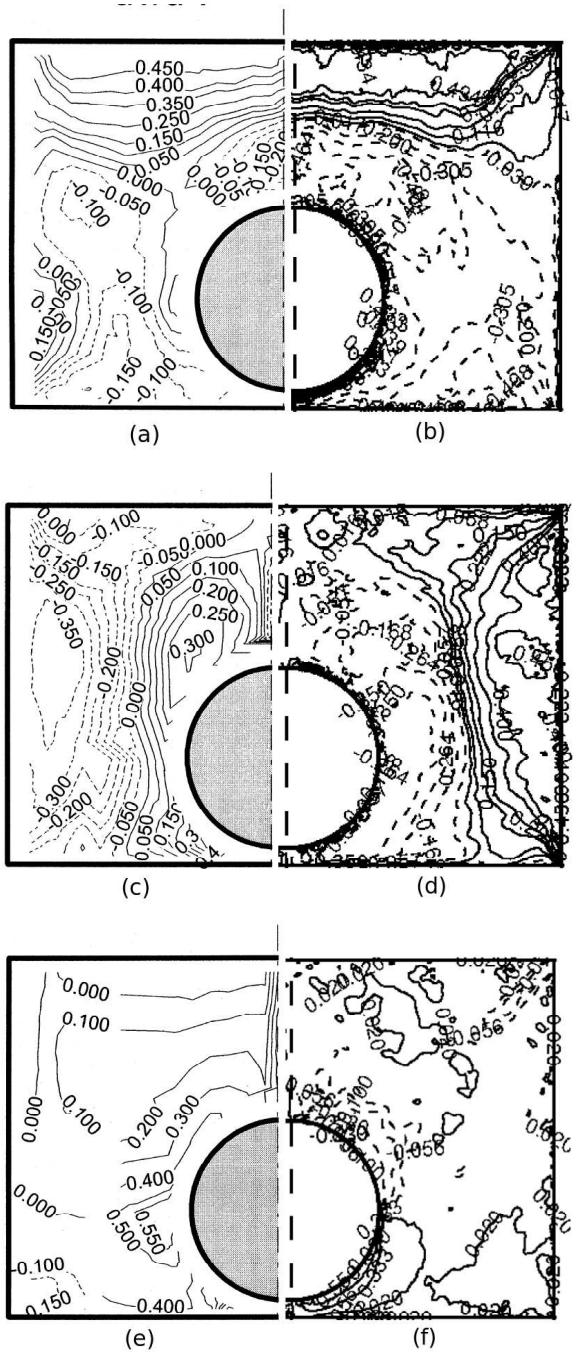

Figure 4.21 Turbulent shear stress correlations (Experimental (Guellouz and Tavoularis, 2000)): (a) Experimental: $\langle uv \rangle / u_{rms} v_{rms}$; (b) LES-IB: $\langle uv \rangle / u_{rms} v_{rms}$; (c) Experimental: $\langle uw \rangle / u_{rms} w_{rms}$; (d) LES-IB: $\langle uw \rangle / u_{rms} w_{rms}$; (e) Experimental: $\langle vw \rangle / v_{rms} w_{rms}$; (f) LES-IB: $\langle vw \rangle / v_{rms} w_{rms}$.

CHAPTER 5. LARGE EDDY SIMULATION OF FLOWS WITH HEAT TRANSFER USING NON-BODY CONFORMAL GRIDS

5.1 Introduction

Turbulent heat transfer in complex geometries is important for many engineering applications such as heat exchanger designs, rod bundle flows in nuclear reactors or even turbine blade cooling. Application of large eddy simulation to industrial problems aims to capture the large turbulent structures, which often requires sufficient near wall grid resolution and good subgrid scale models (Moin, 2002). The conventional body-fitted curvilinear (Jordan, 1999) and unstructured grid LES (Mahesh et al., 2000) solvers have been successfully applied to various flow cases such as gas-turbine combustors and asymmetric diffusers. However, the increasing geometrical complexity makes the body-fitted grid generation more challenging and proper domain decompositon is often required. The non-body conformal grid methods are gaining popularity and have been combined with LES solvers to solve a variety of complex turbulent flow problems (Balaras, 2004; Ghias et al., 2004; Tyagi and Acharya, 2005; Ikeno and Kajishima, 2007). The general approaches include the Cartesian grid method (Ye et al., 1999) and the immersed boundary method (Mohd-Yusof, 1998). Although various succssessful results have been achieved, most of them have been applied to incompressible flow problems and very few results for compressible turbulent flows have been discussed.

Based on the author's knowledge, Kim and Lee (2004) first implemented the immersed boundary method to simulate forced and mixed convection around a circular cylinder with both isothermal and isoflux thermal boundary conditions. It was observed that the averaged and local Nusselt number along the cylinder surface agreed with the experimental results very well. Pacheco et al. (2007) developed a scheme which accounted for Dirichlet, Neumann and

Robin boundary conditions on complex geometries with immersed boundary methods. In their scheme, a bilinear interpolation similar to that of Kim and Lee (2004) was also utilized and flow over a cylinder and sphere with forced and natural convection was simulated. Palma et al. (2006) combined the immersed boundary method with a compressible RANS solver to simulate a supersonic flow past an airfoil and a turbulent flow past a circular cylinder. The pressure coefficient and Mach number contours agreed with body fitted grid results very well. Therefore, it was demonstrated that the immersed boundary method is an appropriate approach to simulate heat transfer and turbulent flow problems. However, based on the author's knowledge, there are no reported data of turbulent heat transfer parameters such as Nusselt number and heat transfer coefficient using immersed boundary method yet.

In this study, we combine the immersed boundary method with a compressible large eddy simulation solver (denoted as LES-IB) and simulate a pipe flow with constant heat flux. Using two different methods of imposing the isoflux thermal boundary condition, the thermal properties obtained from the simulation are reported and compared with the body-fitted DNS and LES results. To verify the code, flow over a heated circular cylinder was simulated at different Reynolds numbers and the results were compared with the results obtained by experiments and body-fitted grid simulations.

5.1.1 Immersed boundary treatment

The basic procedure of the immersed boundary treatment is based on that stated in Chapter 3. Specifically, in the current work where the isoflux thermal boundary condition is imposed, the wall heat transfer is taken into consideration. The forcing calculation procedure includes an extra step to evaluate the temperature of the solid point s closest to the interface as shown in Fig. 5.1. The temperature at the virtual point vp is evaluated based on a bilinear interpolation using its neighbor fluid points. Then the target value for the solid points s is calculated as

$$T_s = T_{vp} - \frac{\partial T}{\partial n} \cdot (\mathbf{x}_{vp} - \mathbf{x}_s). \tag{5.1}$$

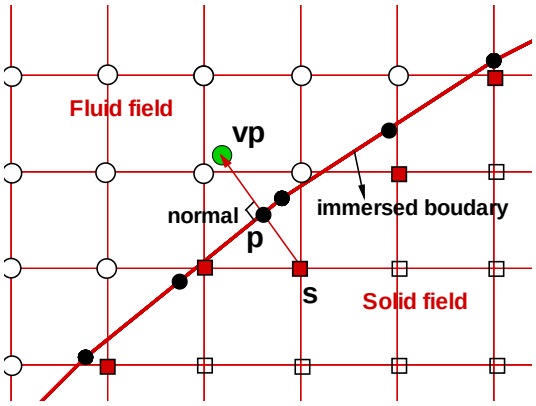

Figure 5.1 Schematic diagram of grid notation close to the immersed interface for isoflux heating case.

5.2 Results

The non-body conformal grid method was applied to flow over a heated cylinder to test the performance of the current solver for laminar flow heat transfer simulations. The simulated drag coefficients, lift coefficients and Strouhal numbers are compared with body-fitted grid simulation results and experimental values in the literature. To demonstrate the capability of the current method in turbulent flow heat transfer simulations, a turbulent pipe flow with $Re_D = 5300$ was simulated and the statistical results are compared to experimental data and body-fitted grid results.

5.2.1 Laminar flow over a heated circular cylinder

In the current work, a three-dimensional mesh was generated with a very thin layer in the spanwise z direction which contains only two cells. The computational domain was $[-20D, 40D]$ in the x direction and $[-20D, 20D]$ in the y direction. A hyperbolic tangent stretching function was employed in both streamwise and transverse directions to ensure that the grids cluster toward the cylinder boundary. The mesh size in the z direction was set to be the same as the smallest grid size in the y direction. To compare the characteristic flow parameters with those calculated from incompressible flow solvers in the literature, the Mach number was set to a small value $Ma = 0.03$. The Navier-Stokes characteristic boundary con-

Table 5.1 Nusselt number comparison for flow over a heated cylinder

$\overline{Nu}$	$Re_D = 40$	$Re_D = 80$	$Re_D = 100$	$Re_D = 120$	$Re_D = 150$
Pacheco et al. (2007)	3.62	4.7	-	5.5	6.13
Kim and Lee (2004)	3.23	-	5.13	5.62	-
Eckert and Soehngen (1952)	3.48	-	5.23	5.69	-
Current LES-IB	3.30	4.37	4.95	5.45	6.13

dition proposed by Thompson (1990) and Poinsot and Lele (1992) was employed at the inlet and outlet, while adiabatic free-shear wall boundary conditions were imposed at the vertical boundaries. Periodic boundary conditions were imposed in the spanwise direction.

The grid convergence study for laminar flow over a cylinder has been demonstrated in Wang and Pletcher (2008), where the current solver was applied for non-heating flow simulations. It was demonstrated that the current solver can achieve second order accuracy globally and locally. Computations were carried out on five sets of grids $115 \times 75 \times 2$, $143 \times 96 \times 2$, $184 \times 120 \times 2$, $230 \times 150 \times 2$ and $345 \times 225 \times 2$. It was shown that the $230 \times 150 \times 2$ grid is fine enough for the current solver to achieve a good agreement with the experimental and body-fitted grid simulation results. A similar grid independence study was also performed for the heating case and it was shown that the grid utilized in the non-heating case is also applicable in the current study. The simulated results for Reynolds number $Re_D = 80, 100, 120, 140$ and $T^* = T_w/T_\infty = 1.1, 1.5, 1.8$ are presented and compared with experimental and simulation results. All of these computations were performed on the grid resolution $230 \times 150 \times 2$, the same as that used in the non-heating cases. The non-dimensional time step was set equal to 0.01, which corresponds to about 600 steps per shedding cycle. The solution at each time step was considered converged if the residual was reduced to 10^{-7}. The computed time-averaged Nusselt numbers $\overline{Nu} = \overline{h}d/k$ are listed in Table 5.1.

As shown in the table, $\overline{Nu}$ increases with Reynolds number and the simulated results with the current LES-IB solver show a consistently good agreement with the reported values in the literature. Figure 5.2 shows the local distribution of the Nusselt number along the cylinder surface, together with the experimental (Eckert and Soehngen, 1952) and the simulation results (Kim and Lee, 2004) for $Re_D = 120$. It can be observed that the current simulation results

show a good agreement with the reported experimental and simulation data.

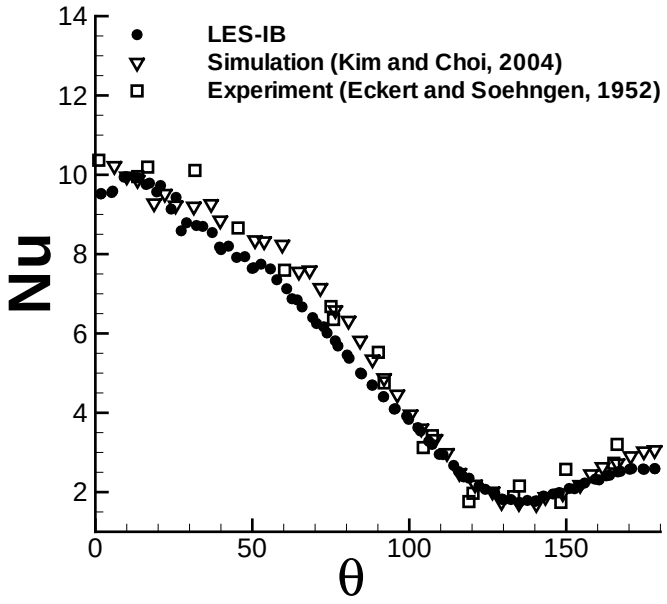

Figure 5.2 Local distribution of Nusselt number along the cylinder surface ($Re_D = 120$).

Figure 5.3 presents the Strouhal number variation for increasing values of T^*, together with the experimental (Wang et al., 2000) and simulation results (Palma et al., 2006). Although the results from the current simulation are slightly higher than those obtained from the experiment and simulation in the literature, the overall tendency of variations with respect to the change of Reynolds numbers and temperature ratios agrees with that reported in the literature. Generally, for a fixed temperature ratio, the Strouhal number increases with Reynolds number. As the temperature ratio increases, the flow tends to be laminarized so the Strouhal number decreases.

Eventually, an effective Reynolds number can be defined based on the effective temperature $T_{eff} = T_\infty + 0.28(T_w - T_\infty)$(Wang et al., 2000). The relationship between Strouhal number and the effective Reynolds number Re_{eff} for $1 \leq T^* \leq 2$ collapses into a universal curve, which is demonstrated in Fig. 5.4 together with the data obtained from the experiment (Wang et al., 2000) and simulation by Palma et al. (2006). The current simulation results capture the

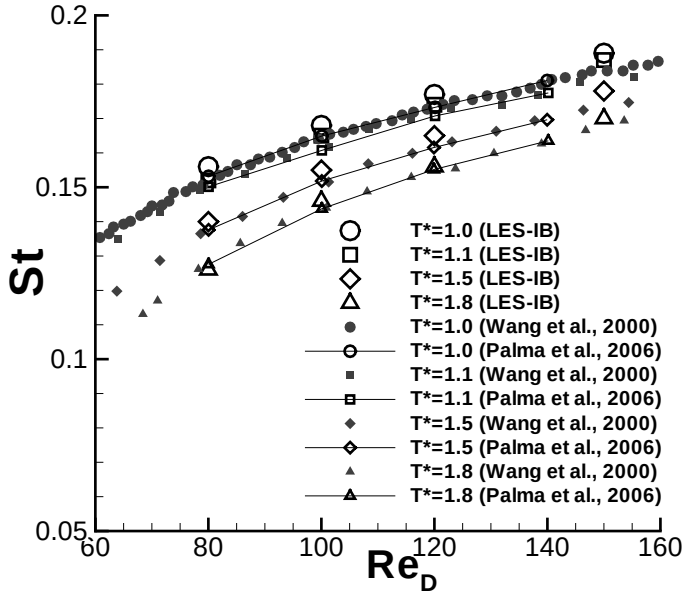

Figure 5.3 Strouhal number variation with Reynolds number and temperature ratio.

trend of variation very well compared to the reference data.

Figure 5.5 shows the Nusselt number variations with temperature ratio for different Reynolds numbers. As the temperature ratio increases, the gas density decreases and viscosity increases and therefore the local Reynolds number goes down. As shown in Incropera et al. (2005), the empirical correlations between Nusselt number and Reynolds number generally satisfy $Nu \propto Re_D^m$. Therefore, the overall trend of Nusselt number variations with respect to the change of temperature ratios is correctly captured. Moreover, the evolution of mean drag coefficients C_d and lift coefficients C_L for different Reynolds number and temperature ratio cases are shown in Fig. 5.6 and Fig. 5.7, respectively. As shown in the figure, the drag coefficient increases with the temperature ratio T^* for all Reynolds number cases, while the magnitude and frequency of lift coefficients decrease. This observation is consistent with the behavior of flow laminarization.

Finally, Fig. 5.8 presents snapshots of temperature contours for different Reynolds number cases. It was shown that the temperature at the center of the first shedding vortex is very

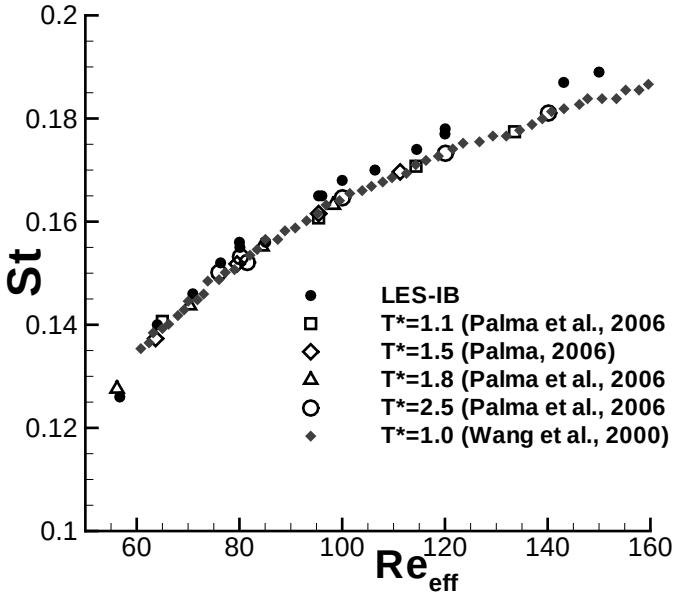

Figure 5.4 Strouhal number variation with effective Reynolds number.

close to the effective temperature calculated with equation $T_{eff} = T_\infty + 0.28(T_w - T_\infty)$, which was also observed in the numerical simulation by Palma et al. (2006).

5.2.2 Turbulent pipe flow with heating

The simulation of turbulent pipe flow with heat transfer was designed to validate the performance of the current LES-IB solver for turbulent flow simulations. The simulation results of the turbulent statistics are compared with DNS data (Satake and Kunugi, 1999) and an LES simulation (Xu and Pletcher, 2005) using body-fitted grids.

5.2.2.1 Simulation details

A fully developed turbulent pipe flow with bulk Reynolds number $Re_b = u_b D/\nu = 5300$ was simulated. Similar to the non-heating case (Wang and Pletcher, 2008), the computational domain is $L = 5D$. The grid independence study was performed with grid resolutions: $60\times80\times80$ (case 1), $100\times108\times108$ (case 2), $128\times136\times136$ (case 3) and $160\times170\times170$ (case 4). The simulation results of turbulent heat flux and temperature contours with $128 \times 136 \times 136$ grid

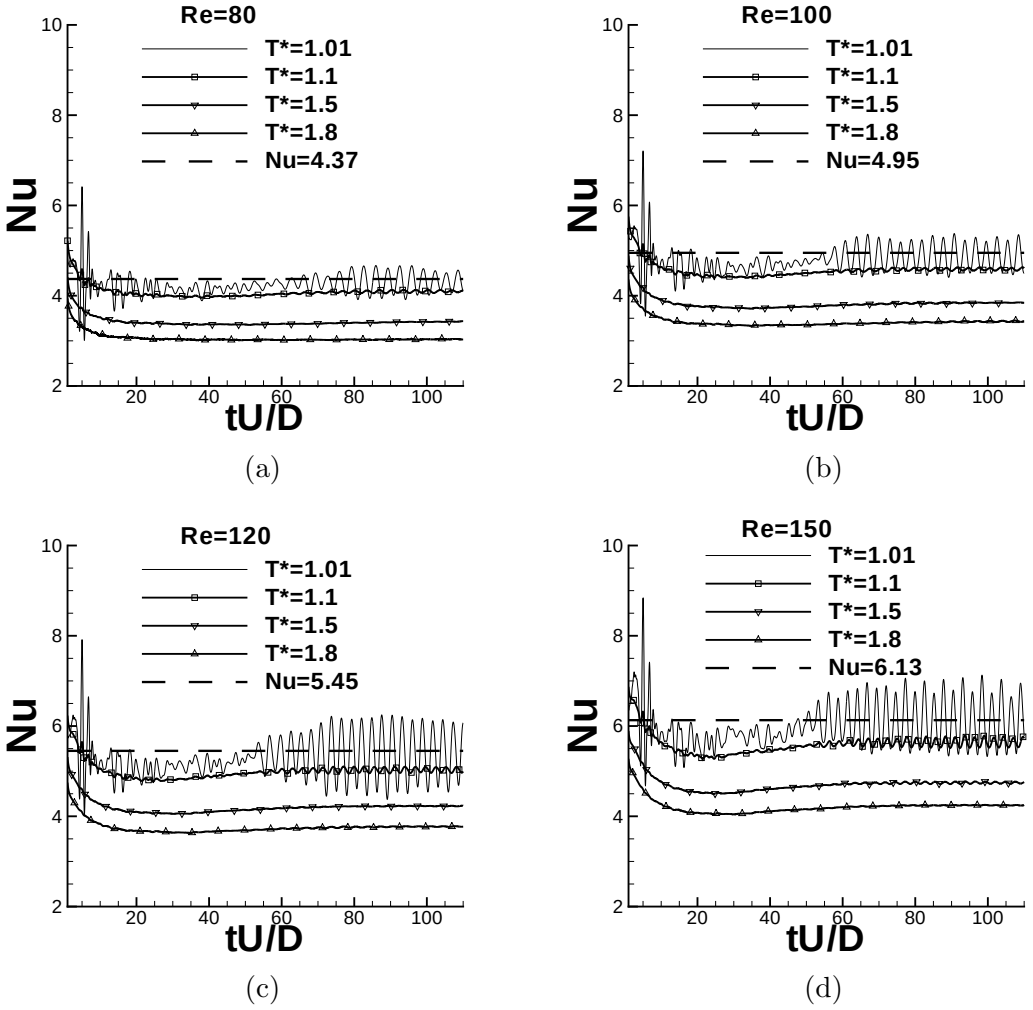

Figure 5.5 Nusselt number evolution at different temperature ratios: (a) $Re_D = 80$; (b) $Re_D = 100$; (c) $Re_D = 120$; (d) $Re_D = 150$

resolution show good agreement with DNS and LES simulations, and exhibit no significant difference from those obtained with a $160 \times 170 \times 170$ grid. Therefore, further simulation results with the $128 \times 136 \times 136$ grid were collected and turbulent statistics for temperature distribution were calculated. To keep the effects of property variations small enough to allow comparison with passive scalar DNS simulation results, the heat flux was kept as low as the one used in the LES simulation (Xu and Pletcher, 2005). The Mach number was 0.001 and the non-dimensional physical time step was set as 0.01 to satisty the CFL number requirement. The computational domain and grid topology are shown in Fig. 5.9. As shown in the figure, grids are uniform in the streamwise direction and clustered toward the pipe wall in the y and z directions. The grid resolutions in terms of wall units are listed in Table 5.2, where the definition of wall coordinates is $x^+ = u_\tau x/\nu_w$ and $y^+ = u_\tau y/\nu_w$.

Table 5.2 Pipe flow grid resolution in wall coordinates

Grid	Streamwise		Normal to the wall ($\theta = 0°$ or $90°$)			
	Δx	Δx^+	Δy_{min}	Δy^+_{min}	Δy_{max}	Δy^+_{max}
case 1	0.125	24.20	0.0055	1.065	0.0335	6.487
case 2	0.10	21.61	0.0033	0.713	0.0268	5.790
case 3	0.075	14.79	0.00323	0.637	0.0234	4.618

The immersed boundary conditions were implemented at the pipe wall to achieve a no-slip velocity condition and zero normal pressure gradient boundary condition. In the streamwise direction, periodic boundary conditions were enforced except for the treatment of pressure and temperature. The pressure actually decreases in the streamwise direction so it was assumed to be step-periodic and decomposed into periodic and aperiodic components as

$$\bar{p}(x, y, z, t) = \beta x + \bar{p}_p(x, y, z, t), \tag{5.2}$$

where β is the average streamwise pressure gradient. The equation of state becomes

$$\bar{\rho}(x, y, z, t) = \frac{\bar{p}}{R\tilde{T}} = \frac{\beta x}{R\tilde{T}} + \frac{\bar{p}_p(x, y, z, t)}{R\tilde{T}}. \tag{5.3}$$

In the current study, the pressure gradient part was implemented as a body force on the right hand side of the streamwise velocity momentum equation and the periodic pressure

component was determined by requiring that the mean mass flow rate be constant. Following the approach investigated by Benocci and Pinelli (1990), the average streamwise pressure gradient was calculated dynamically at each physical time step to provide the desired mass flow rate as

$$\beta^{n+1} = \beta^n - \frac{1}{\Delta t}\left[\left(\frac{\dot{m}}{A_c}\right)^0 - 2\left(\frac{\dot{m}}{A_c}\right)^n + \left(\frac{\dot{m}}{A_c}\right)^{n-1}\right], \tag{5.4}$$

where A_c is the cross-section area of the flow domain and Δt is the physical time step. The average mass flow rate $\dot{m}/A_c$ is defined as

$$\frac{\dot{m}}{A_c} = \frac{1}{A_c}\int \langle \rho u \rangle_s dA \tag{5.5}$$

where $\langle\cdot\rangle_s$ represents an ensemble average along the streamwise and circumferential directions. $(\dot{m}/A_c)^0$ is the desired mass flow rate and its non-dimensional value is 1.0. Similarly, the temperature was treated in a step periodic manner as

$$\begin{aligned} \tilde{T}_p(0,y,z,t) &= \tilde{T}_p(L_x,y,z,t) - \Delta\tilde{T}_x, \\ \tilde{T}_p(L_x,y,z,t) &= \tilde{T}_p(0,y,z,t) + \Delta\tilde{T}_x. \end{aligned} \tag{5.6}$$

Assuming that the axial conduction and viscous dissipation are negligible, the bulk streamwise temperature difference $\Delta\tilde{T}_b$, was obtained by the energy balance of the computational domain

$$\Delta\tilde{T}_b = \frac{4q_w L_x}{(\dot{m}/A_c)D}, \tag{5.7}$$

where the bulk temperature is defined as

$$T_b(x) = \frac{1}{\rho_b U_b A_c}\int \rho U T dA. \tag{5.8}$$

The constant nondimensional heat flux desired at the wall, q_w, is defined as

$$q_w = \frac{q_w^*}{\rho_{ref} U_{ref} c_p^* T_{ref}}, \tag{5.9}$$

where q_w^* is the dimensional wall heat flux $q_w^* = -k^*\frac{\partial T^*}{\partial y^*}$. In the current study, q_w was set to the same value, 4.0×10^{-4}, as that used in the DNS and LES simulations. For constant wall heat flux, the averaged streamwise gradients for local, wall and bulk temperatures are all equal to a constant and only depend on the amount of heat added to the flow, i.e.,

$$\frac{\partial T}{\partial x} = \frac{\partial T_w}{\partial x} = \frac{\partial T_b}{\partial x}. \tag{5.10}$$

Therefore, the local temperature difference $\Delta\tilde{T}_x$ is

$$\Delta\tilde{T}_x = \Delta\tilde{T}_b = \frac{4q_w L_x}{(\dot{m}/A_c)D}. \tag{5.11}$$

It was shown by Kasagi et al. (1989) and Xu and Pletcher (2005) that the implementation of a Neumann boundary condition by directly imposing wall normal temperature gradients would lead to larger wall temperature fluctuations than those observed experimentally because the simulations do not take into account the heat capacity of the wall. Therefore, an alternative procedure to represent the isoflux boundary condition was established by setting a specified wall temperature which varied linearly in the streamwise direction

$$T_w(x) = T_w(0) + \left(\frac{\partial T_w}{\partial x}\right) x, \tag{5.12}$$

where $T_w(0)$ is the wall temperature at the inlet of the simulating domain and the temperature gradient $\partial T_w/\partial x$ is evaluated based on Eqn. (5.11). In this study, both implementations with specified linearly varying wall temperature and traditional heat flux conditions were implemented and compared with DNS and LES results. These two conditions will be hereafter referred to as specified linear wall temperature and specified heat flux conditions, respectively.

5.2.2.2 Temperature Statistics

The turbulent statistics of temperature distributions are compared to the passive scalar DNS (Satake and Kunugi, 1999) and LES results (Xu and Pletcher, 2005).

The non-dimensional temperature θ^+ is defined as

$$\theta^+(x,y,z,t) = \frac{\langle T_w^* \rangle(x) - T^*(x,y,z,t)}{T_\tau^*}, \tag{5.13}$$

where $\langle T_w^* \rangle$ is the averaged wall temperature and T_τ^* is the friction temperature $T_\tau^* = \frac{q_w^*}{\rho_w^* c_p^* u_\tau^*}$. Since the variation of the temperature θ^+ in the streamwise direction was negligibly small due to very low heat transfer, the ensemble averages of the temperature statistics were performed in the streamwise and circumferential directions and in time. Figure 5.10 shows the mean temperature profiles normalized by friction temperature T_τ. It can be observed that the linear velocity distribution $\theta^+ = \mathrm{Pr} y^+$ for $y^+ < 5$ has been well resolved with both specified linear wall

temperature and specified heat flux thermal boundary conditions. As $y^+ > 5$, the simulated results also agree well with DNS and the empirical log-law profile $\theta^+ = 2.853\ln y^+ + 2.347$ in the logrithmic region.

The temperature fluctuations in the near wall region are shown in Fig. 5.11, together with the DNS and LES results. It can be observed that the LES-IB simulation with either specified linear wall temperature or specified heat flux boundary condition resulted in similar temperature fluctuation profiles and they agree well with the DNS results close to the pipe wall. Specifically, at the location very close to the wall, the specified linear wall temperature condition resulted in better agreement with the DNS data while a slightly larger difference from DNS data was observed for the specified heat flux condition. Similar behavior was also observed by the LES simulations. As shown in Fig. 5.11, the LES simulation with the specified heat flux condition led to large overprediction of temperature fluctuations near the wall while a good agreement with DNS was obtained with the specified linear wall temperature condition. However, at the positions away from the wall, the LES-IB simulation shows slightly overprediction compared to DNS and LES. For the specified heat flux case, the magnitude of the overprediction is similar to that in the LES simulation.

The streamwise and wall-normal turbulent heat fluxes normalized by friction velocity and temperature are shown in Fig. 5.12 and Fig. 5.13, respectively. Unlike the LES simulation results, in which a significant overprediction of streamwise turbulent heat flux is observed for the specified heat flux thermal boundary condition, very good agreement with DNS results can be observed for both boundary conditions in the LES-IB simulations. Similarly, the wall-normal turbulent heat flux obtained from both thermal boundary conditions agree with the DNS satisfactorily in both LES and LES-IB simulations.

The $u\theta$ and $u_r\theta$ cross-correlation coefficients defined as

$$R(u\theta) = \frac{\langle u'\theta' \rangle}{u'_{rms}\theta'_{rms}} \tag{5.14}$$

$$R(u\theta) = \frac{\langle u'_r\theta' \rangle}{u'_{rrms}\theta'_{rms}} \tag{5.15}$$

are shown in Fig. 5.12 and Fig. 5.13. Good agreement with DNS results was observed in the

near wall region; however, a large overprediction was observed in the core region. This is most likely because of the large over prediction of the temperature fluctuations in the core region at a low heating level.

5.2.2.3 Nusselt number comparison

The average friction coefficients and Nusselt numbers calculated from the specified linear wall temperature and specified heat flux conditions are compared to LES results and the constant property correlations proposed by Gnielinski (1976), which are valid for $2300 < Re_D < 5 \times 10^6$. The friction coefficient correlation is $C_f = (1.58\ln Re_D - 3.28)^{-2}$ and the Nusselt number correlation is defined as

$$Nu_D = \frac{(C_f/2)(Re_D - 1000)Pr}{1 + 12.7(C_f/2)^{1/2}(Pr^{2/3} - 1)}, \tag{5.16}$$

where Re_D is the bulk Reynolds number based on the hydraulic diameter. The average friction factor and Nusselt number for both cases are compared with LES and correlation values in Table 5.3. In the table, the difference between the LES-IB, LES simulation results and the correlation, is defined as

$$diff = \frac{\text{Comparison data} - \text{Correlation value}}{\text{Correlation value}}. \tag{5.17}$$

It is observed from Table 5.3 that the friction coefficients are slightly underpredicted and the Nusselt numbers are overpredicted in the current LES-IB simulation compared to the correlation. But the difference is generally less than 10%, which is within the uncertainty band usually ascribed to the correlations for turbulent flows with heat transfer. Compared to the LES simulations, the Nusselt numbers obtained from LES-IB simulations are closer to the correlations for both thermal boundary conditions.

5.3 Conclusions

A non-body conformal grid method was incorporated into a large eddy simulation solver to simulate laminar and turbulent heat transfer problems. The scheme was developed based on fixed Cartesian grids which significantly simplifies the grid generation procedure. Flow

Table 5.3 Pipe flow: Friction factor and Nusselt number comparison

Comparison	C_f	Diff.(%)	Nu	Diff.(%)
Specified wall heat flux q_w				
LES-IB	0.0091	-4.21	17.90	3.89
LES (Xu and Pletcher, 2005)	0.01	5.26	16.3	-5.4
Correlation (Gnielinski, 1976)	0.0095	-	17.23	-
Specified linear wall temperature T_w				
LES-IB	0.0088	-5.38	18.21	1.17
LES (Xu and Pletcher, 2005)	0.0085	-8.6	17.0	-5.5
Correlation (Gnielinski, 1976)	0.0093	-	18.0	-

over a heated cylinder at different Reynolds number and temperature ratio conditions was simulated using the methodology developed to validate the numerical scheme. The Nusselt number study with $Re_D = 40, 80, 100, 120, 150$ demonstrated the accuracy and consistency of the current method. The local distribution of Nusselt number along the cylinder surface agreed with the experimental and reference numerical simulation satisfactorily. As the temperature ratio increased, the drag coefficients increased and the magnitude and frequency of lift coefficients decreased, which reflects the laminarization tendency of the flow. Also, the temperature contours showed that the temperature at the center of the first vortex was very close to the effective temperature defined in the literature.

The turbulent pipe flow simulation obtained with the current LES-IB method demonstrated the capability of this solver to simulate turbulent heat transfer with non-body conformal grids. Two ways of imposing the uniform heat flux wall boundary condition was investigated. The nondimensional temperature statistics show good agreement with DNS and LES data, where the mesh is aligned with the wall normal direction. In the near wall region, the temperature fluctuations compared well with DNS results, while it was slightly overpredicted with the specified wall heat flux boundary condition. Good agreement with DNS was obtained for both the streamwise and wall-normal turbulent heat fluxes. The friction coefficients and Nusselt numbers agreed with the constant property empirical correlations within the uncertainty level usually ascribed to the correlations for turbulent flows with heat transfer.

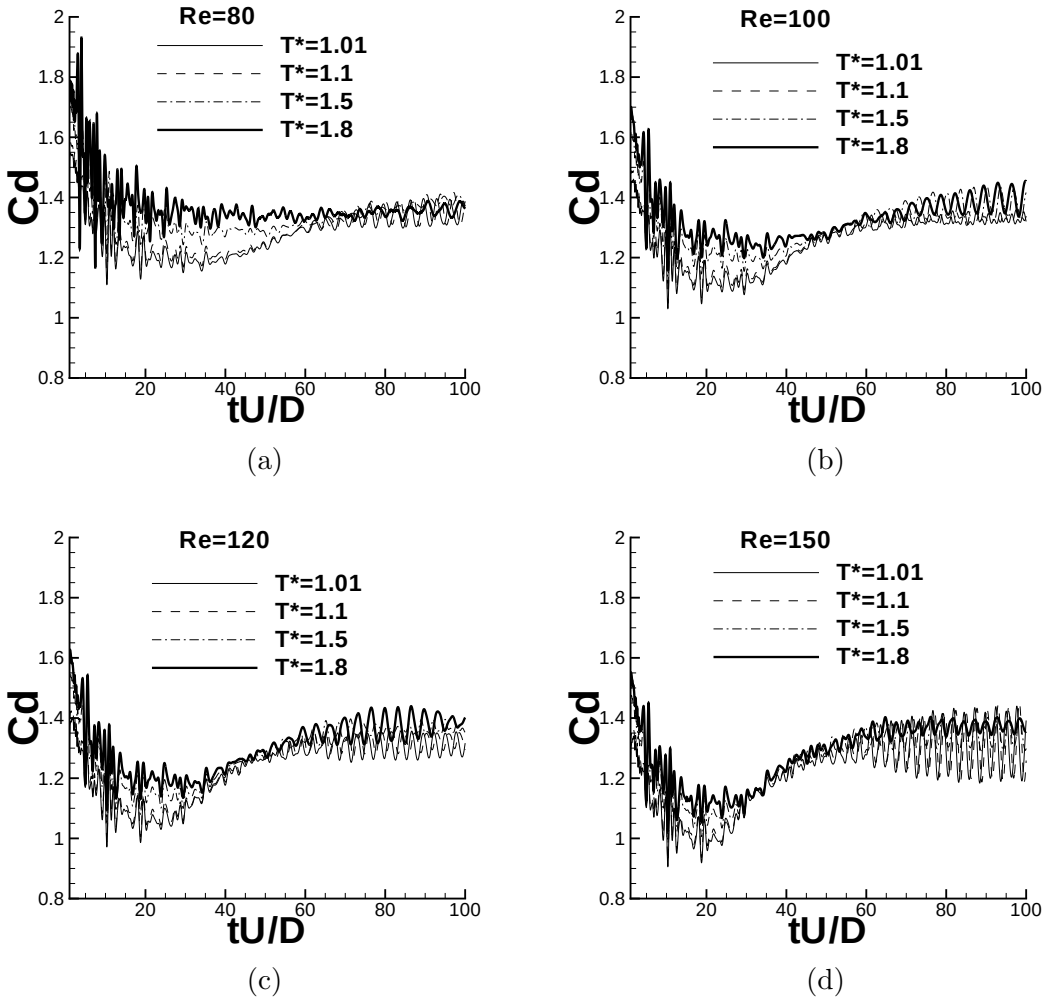

Figure 5.6 Drag coefficient evolution at different temperature ratios: (a) $Re_D = 80$; (b) $Re_D = 100$; (c) $Re_D = 120$; (d) $Re_D = 150$

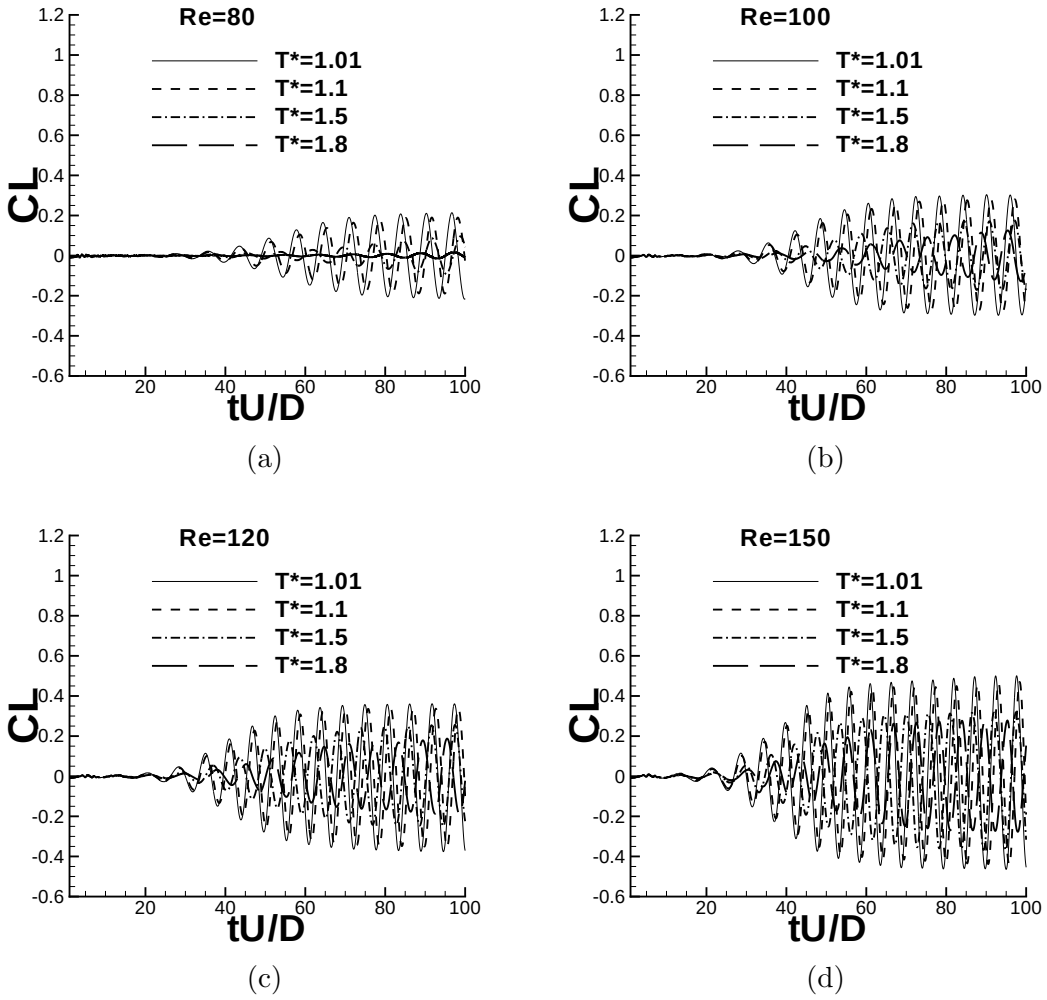

Figure 5.7 Lift coefficient evolution at different temperature ratios: (a) $Re_D = 80$; (b) $Re_D = 100$; (c) $Re_D = 120$; (d) $Re_D = 150$.

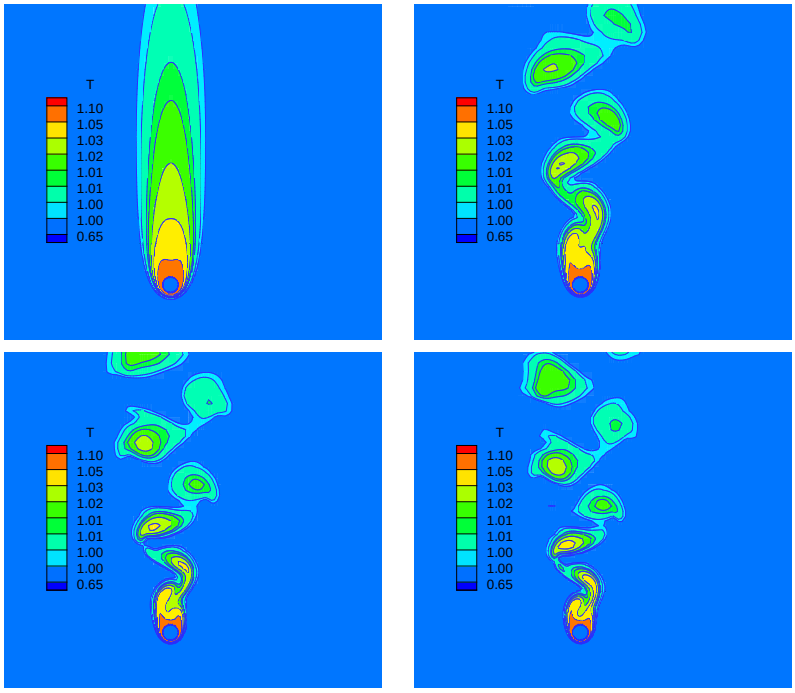

Figure 5.8 Temperature contours for $Re_D = 40, 80, 120, 150$ ($T^* = 1.1$), where the flow direction from bottom to top.

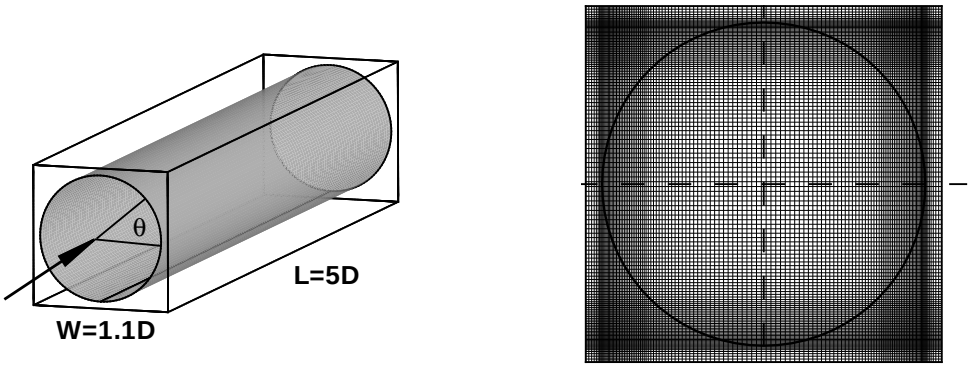

(a) (b)

Figure 5.9 (a) Computational domain; (b) Cross section grid distribution ($100 \times 136 \times 136$).

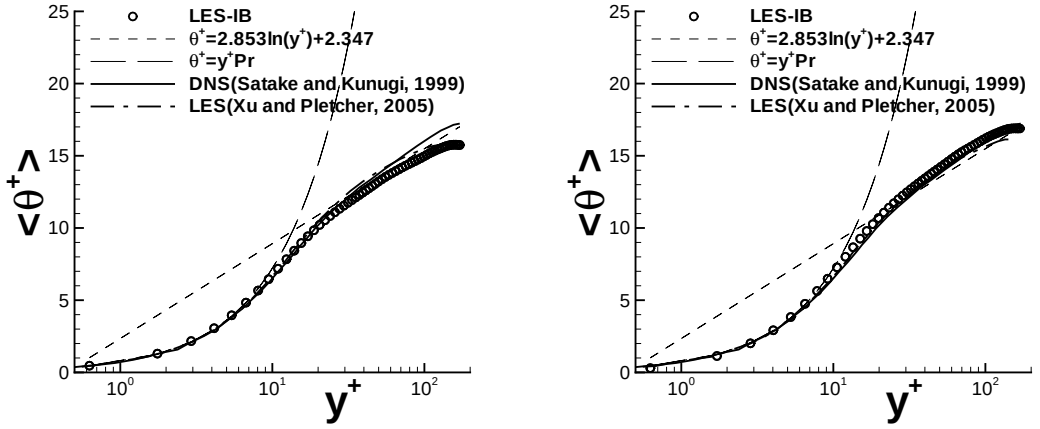

(a) Specified linear wall temperature (b) Specified heat flux

Figure 5.10 Mean temperature distribution in wall coordinates.

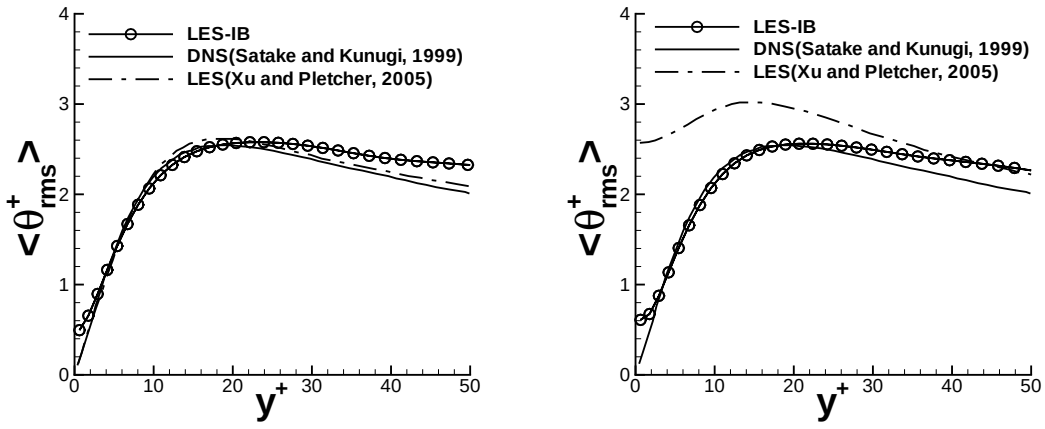

(a) Specified linear wall temperature (b) Specified heat flux

Figure 5.11 Temperature fluctuation normalized by friction temperature.

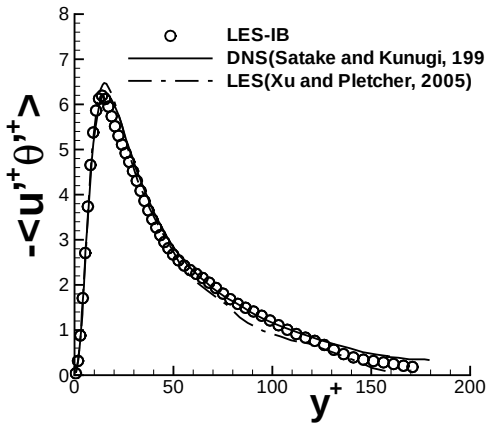

(a) Specified linear wall temperature

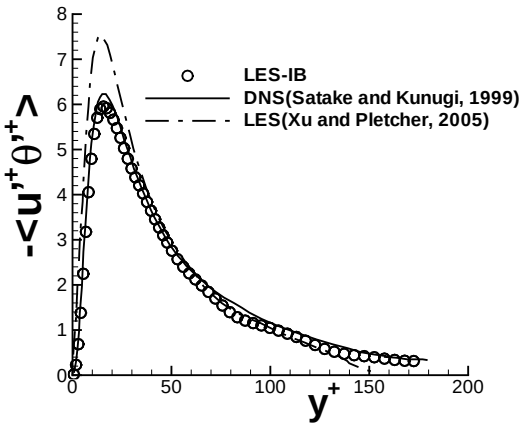

(b) Specified heat flux

Figure 5.12 Streamwise turbulent heat flux normalized by friction velocity and temperature.

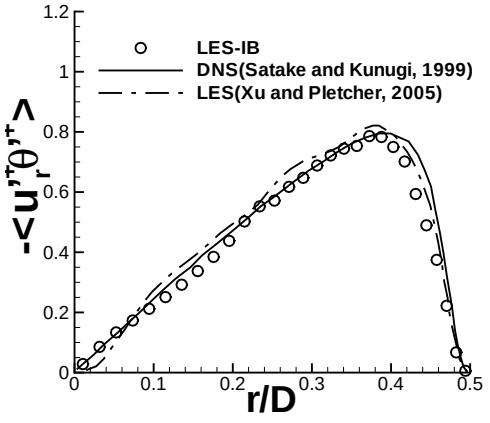

(a) Specified linear wall temperature

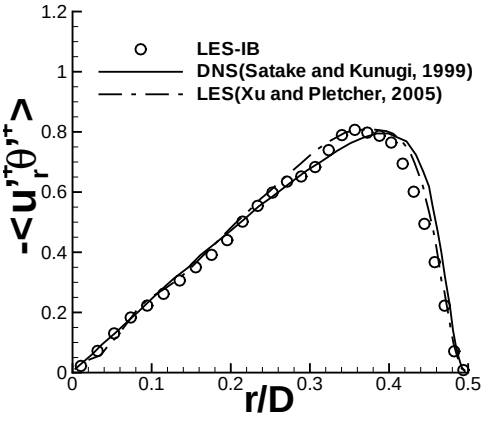

(b) Specified heat flux

Figure 5.13 Wall-normal turbulent heat flux normalized by friction velocity and temperature.

CHAPTER 6. LARGE EDDY SIMULATION OF COMPLEX FLOW PROBLEMS

In this chapter, transonic and supersonic flow over a cylinder, flow over an oscillating cylinder and an internal flow through a subchannel around two cylindrical rods are studied. The results are compared with experimental data and show the capability of the current immersed boundary method in simulating high Mach number and high Reynolds number flows in complex geometries.

6.1 Simulation of compressible flow over cylinder

In the literature, a series of immersed boundary method based Navier-Stokes solvers have been developed for incompressible flows. However, a compressible flow solver with the IB method is relatively rare. Palma et al. (2006) implemented the immersed boundary method in a finite-volume based compressible flow solver with a $k-\omega$ model and simulated both incompressible and compressible flows. Ghias et al. (2007) combined the immersed boundary method with a finite difference compressible flow solver and simulated a series of low and high Reynolds number flows. To the auther's knowledge, no implementation of this approach for a compressible, finite-volume based large eddy simulation solver exists in the literature yet. The differences in the grid resolution and boundary conditions between incompressible and compressible flows requires some additional considerations when developing an IB method. It should also be pointed out that a finite-volume based Cartesian grid method for inviscid compressible flows has been developed by Colella et al. (2006) and Miller and Colella (2002). However, the inclusion of viscosity changes the character of the governing equations and the requirements on temporal and spatial discretization. The existence of a boundary layer has

a dominant consequence on the features of the IB method since it requires very fine grid resolution near the immersed boundary.

6.1.1 Problem description

In order to demonstrate the performance of the current solver in handling compressibility effects, a transonic flow condition ($Ma_\infty = 0.75$, $Re = 100$) and a supersonic flow condition ($Ma_\infty = 1.3$, $Re = 300$) were tested. The grid resolution is similar to that in the cylinder case in Chapter 4. In compressible flows, the imposition of boundary conditions needs special care. For hyperbolic systems, the number of boundary conditions needed must be equal to the number of characteristics that are directed from the exterior of the region toward the boundary. For subsonic flows, the characteristics carry information toward the flow domain both from the interior and exterior. The boundary conditions are used to replace the information carried to the boundary by the characteristics from the exterior. At the outflow boundaries, some of the characteristics have a negative sign and the corresponding boundary conditions must be specified from the exterior. The others then can be determined from the interior. The specification of the outflow boundary condition must be selected to ensure the numerical problem is well posed (Tannehill et al., 1997). For supersonic flows, the signals are carried into the domain from the upstream region by both the streamline characteristics as well as the characteristics involving the acoustic speeds. Therefore, all the information at the inflow boundary must be specified using the free stream conditions. There are no characteristics that carry information from the interior of the domain to the boundary. At the outflow boundaries, the characteristics all carry the same sign for the supersonic case and the solution must be determined entirely from conditions based on the interior. In this study, the boundary condition was specified following the method proposed by Poinsot and Lele (1992). At the transverse boundaries the free stream velocity, pressure and temperature are determined by assuming adiabatic conditions. The periodic boundary condition is specified in the spanwise direction.

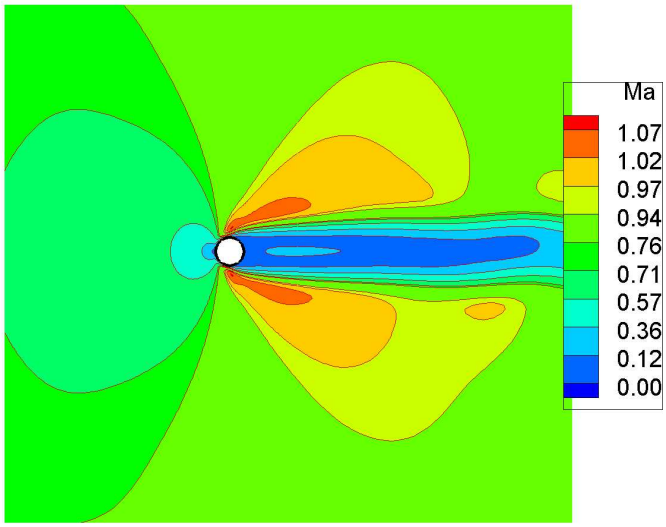

Figure 6.1 Mach number contours at $Re = 100$ and $Ma_\infty = 0.75$, where flow direction is from left to right.

6.1.2 Results analysis

The results of the transonic flow case are show in Figs. 6.1, 6.2 and 6.3. As the flow goes over the cylinder, it accelerates and consequently the local Mach number goes over 1.07 which is clearly in the compressible regime. For the supersonic flow case, the instantaneous pressure and temperature contours are shown in Figs. 6.4 and 6.5. As shown in the figures, a bow shock forms as the flow approaches the stationary object. After the shock, pressure, temperature and density have a rapid rise.

The simulation Mach number contours (Fig. 6.6) are compared to those obtained by Palma et al. (2006) (Fig. 6.7), while the density contours (Fig. 6.8) are compared to the simulation by Boiron et al. (2009) (Fig. 6.9). Although the Reynolds number simulated in the current study is smaller than that in both the studies by Palma et al. (2006) and Boiron et al. (2009) ($Re_\infty = 2 \times 10^5$ and $Re_\infty = 5 \times 10^4$, respectively), the effect on the flow behavior by the bow shock was captured in the present simulation. However, as shown in Fig. 6.8 and 6.9, the distances between the bow shock and the cylinder are different due to different Mach numbers.

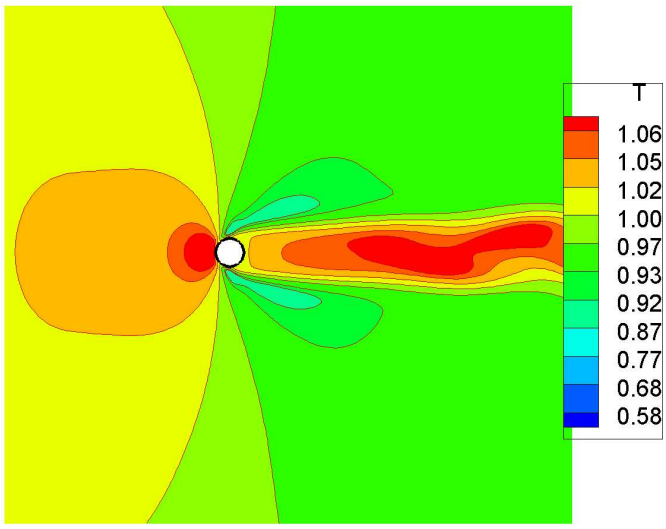

Figure 6.2 Temperature contours at $Re = 100$ and $Ma_\infty = 0.75$.

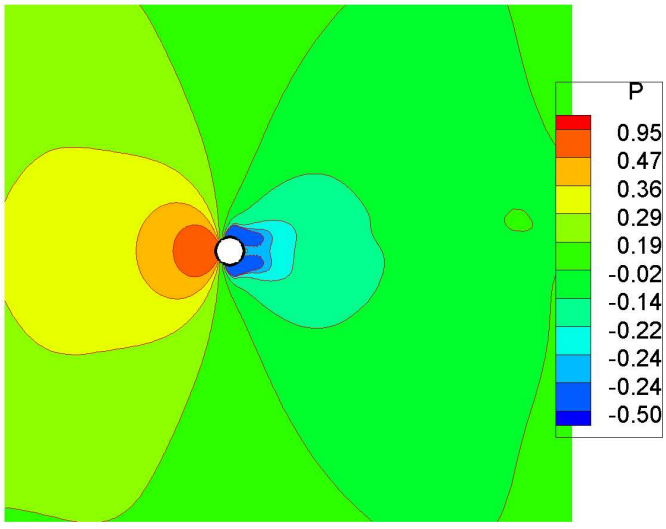

Figure 6.3 Pressure contours at $Re = 100$ and $Ma_\infty = 0.75$.

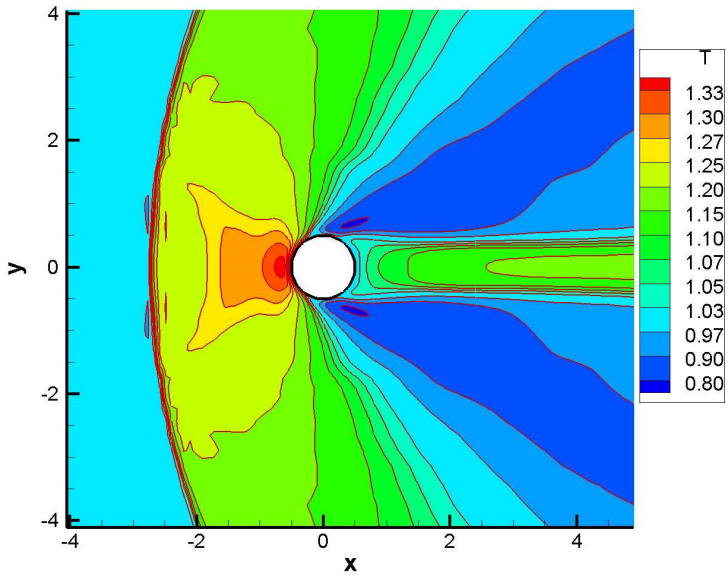

Figure 6.4 Temperature contours at $Re = 300$ and $Ma_\infty = 1.3$.

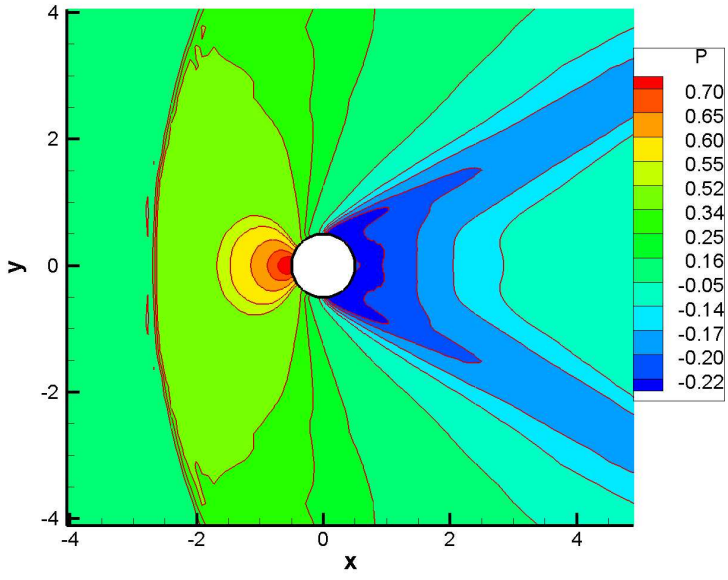

Figure 6.5 Pressure contours at $Re = 300$ and $Ma_\infty = 1.3$.

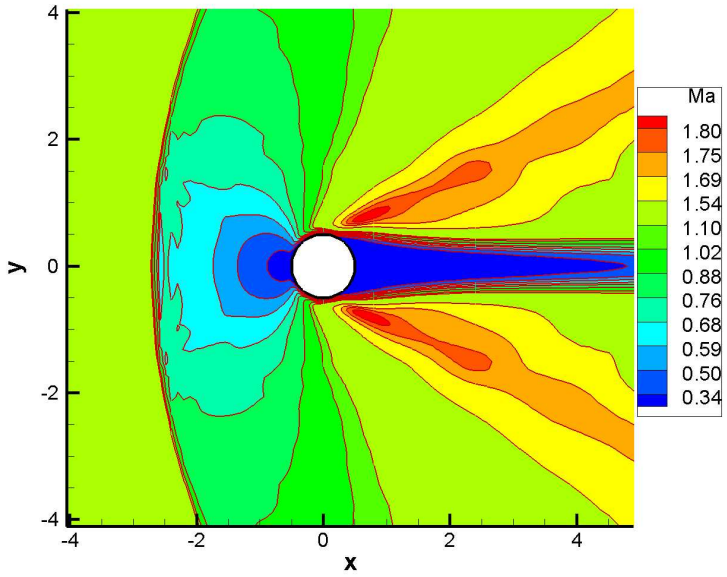

Figure 6.6 Mach number contours at $Re = 300$ and $Ma_\infty = 1.3$.

From theoretical and experimental results, Billig (1967) proposed a formula to estimate the distance Δ between the shock and the obstacle along the stagnation line as

$$\frac{\Delta}{r} = 0.386 exp(\frac{4.67}{M_\infty^2}), \tag{6.1}$$

where r is the radius of the cylinder. The distance Δ from current simulation is $\Delta \approx 5.7r$, which is close to the estimated value from above equation, $6r$. Also based on this formula, it can be expected that the distance is larger for lower Mach number flows. Therefore, it can be observed from Fig. 6.8 that the distance between the bow shock and the cylinder along the stagnation line is larger that observed in Fig. 6.9. At last, it should be pointed out that the current simulation for supersonic flow case only serves as a demonstrative study to show the possibility of applying immersed boundary method in compressible flow simulations. To obtain quantitative comparisons with experiments or body-fitted grid simulations, further detailed study is required.

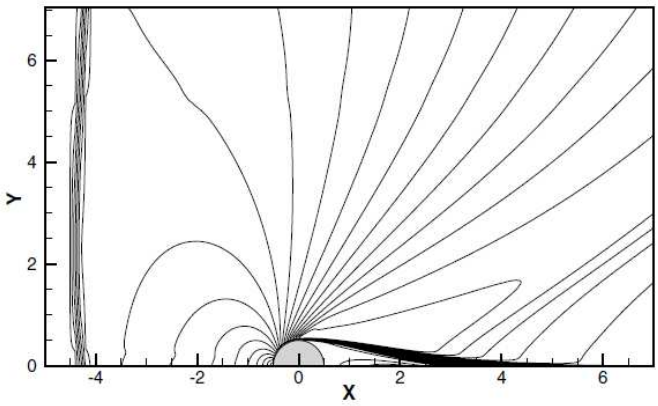

Figure 6.7 Palma et al. (2006): Mach number contours for $Ma_\infty = 1.3$.

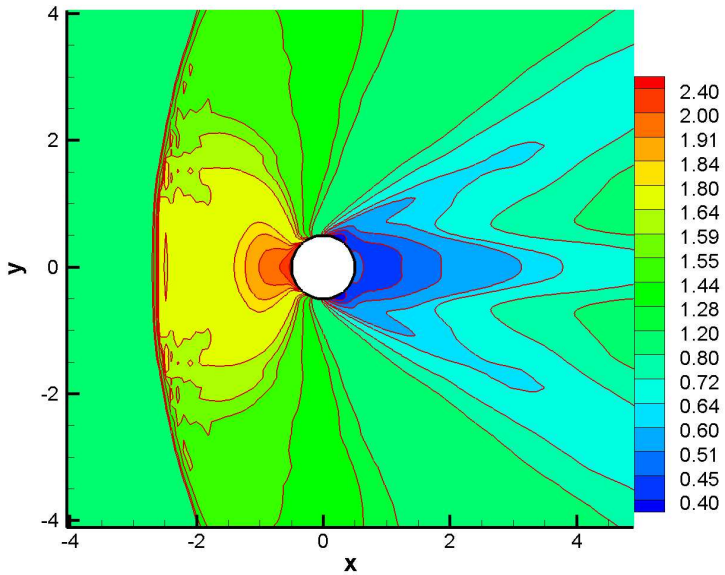

Figure 6.8 Density contours at $Re = 300$ and $Ma_\infty = 1.3$.

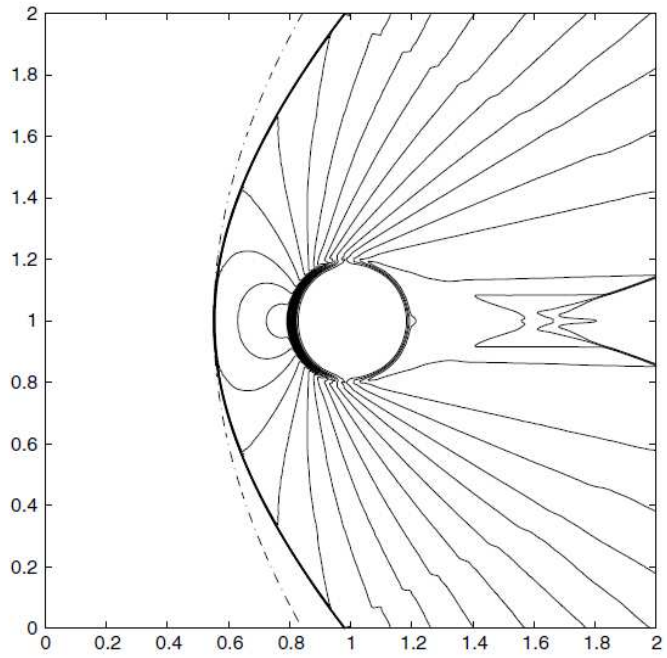

Figure 6.9 Boiron et al. (2009): Density contours for $Ma_\infty = 2$.

6.2 Simulation of flow over an oscillating cylinder

Flow over an oscillating cylinder was simulated to test the capability of the current solver in solving flow problems with immersed moving objects. The parameters were chosen based on the simulation of Guilmineau and Queutey (2002). The prescribed motion of the cylinder in the cross-stream direction is assumed to be $y(t) = Asin(2\pi f_e t)$, where $A = 0.2D$ and f_e is the excitation frequency. In the simulation of Guilmineau and Queutey (2002), five sets of frequency values were tested with $F = f_e/f_0 = 0.8, 0.9, 1.0, 1.1, 1.12, 1.2$ with f_0 being the vortex shedding frequency for a fixed cyilnder at $Re = 185$. In the current study, three sets of frequency values were studied as $F = 0.8, 0.975, 1.2$. The reason for choosing $F = 0.975$ is that a half cycle motion comparison can be made between the present simulation with that by Blackburn and Henderson (1999). The computational domain was $60D \times 40D \times 0.06D$ and the boundary conditions were specified similar to those for fixed cylinder simulations. The instantaneous vorticity contours for the cylinder at the extreme upper position were plotted out and compared with those from Guilmineau and Queutey (2002), as shown in Fig. 6.10. It

can be observed that, as the frequency ratio F increases, the length of the vortex attached to the upper side of the cylinder decreases. As was discussed in Guilmineau and Queutey (2002), for $F > 1.10$, the upper vortex was diminished in strength to the extent that the lower vortex became the dominant vortex and the upper vortex rolled up tightly behind the cylinder. The same trend was well captured in the current simulation when $F = 1.2$. To compare the vorticity contours within a half cycle, the current simulation results for $F = 0.975$ are compared to those of Blackburn and Henderson (1999) in Fig. 6.11. As shown in the figure, the vorticity patterns within half of a cycle are quite similar in both simulations. However, it should be pointed out that the Reynolds number is $Re = 500$ in the simulation of Blackburn and Henderson (1999) and they assumed the flow behavior was still two-dimensional.

6.3 Large eddy simulation of subchannel flows surrounding two cylindrical rods in a rectangular duct

6.3.1 Introduction

Idealized flow geometries are often not found in the reactor cores of light water reactors which include closely-packed fuel rods, grid spacers and a variety of deflectors. The flow geometry is generally more complex than the geometries that have been used to generate the empirical correlations used in the thermal hydraulic safety codes. As a powerful tool to help the design and operation of reactors, computational thermal fluid mechanics has been applied for flow simulations in and around complex geometries in advanced light water reactors (ALWRs) and supercritical fluid reactors (SCRs). However, most of these applications depend on turbulence models such as the $k - \epsilon$ model or eddy viscosity model (EVM). Predictions of mean velocity profiles which appear reasonable can be misleading, particularly when wall heat transfer and friction are important (McEligot, 1986). One of the major deficiencies of turbulence models based on the dissipation ϵ equation is that they are known to predict the onset of separation too late and to underprecidt the amount of separation (Menter and Esch, 2001). Direct numerical simulation solves the the N-S equations without modeling but its high computational cost inhibits the resolution of the flow characteristics. On the other hand, large

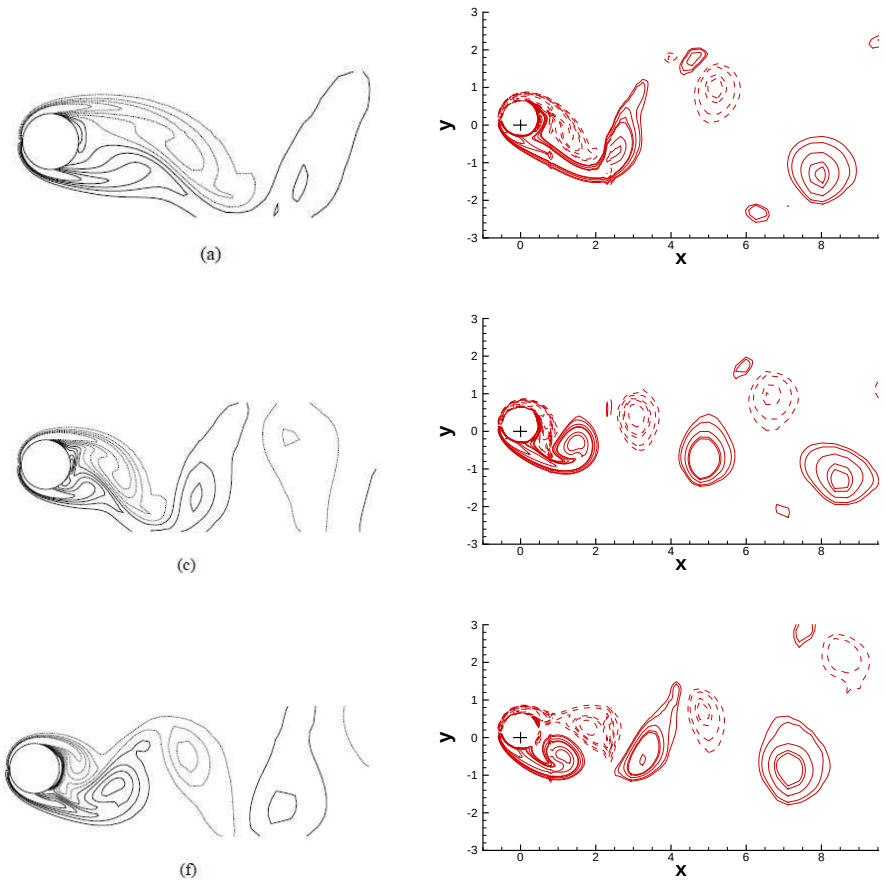

Figure 6.10 Instantaneous vorticity contours for Re=185 and A/D=0.2. In all frames, the location of the cylinder is at its extreme upper position. left - simulation by Guilmineau and Queutey (2002)(F=0.8, 1.0, 1.2); right - LES-IB simulation (F=0.8, 0.975, 1.2).

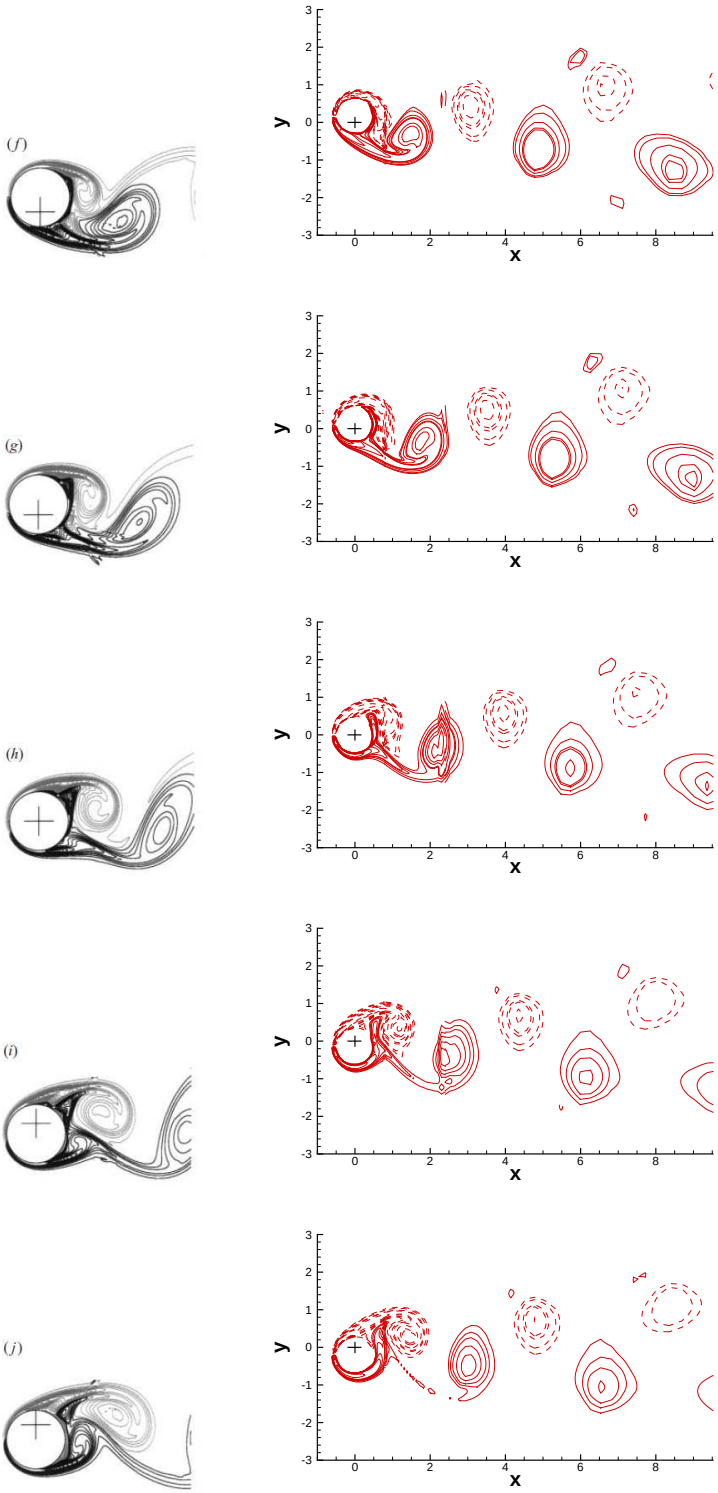

Figure 6.11 Instantaneous vorticity contours over a half cycle: left - Blackburn and Henderson (1999)(A=0.25, F=0.975); right - LES-IB simulation (A=0.2, F=0.975).

eddy simulation (LES) solves most energetic eddies directly in the flow and models the smallest scales which require very fine grid resolutions. Therefore, this approach requires less computer power than DNS and quite realistic results can be obtained since modeling generally plays a fairly minor role in LES.

6.3.2 Problem description

This section demonstrates a practical application of the immersed boundary method in a complex geomtry flow simulation. As shown by Smith (2005), the safe, reliable and efficient operation of nuclear reactors depends on the ability to accurately predict velocity and temperature distributions in the flow inside coolant channels. Significant differences and uncertainties have been found between thermal hydraulic correlations for various types of reactors. To predict the the flow behavior through rod bundles, Smith (2005) carried out an experiment with two parallel rods which represented a small section of a reactor core. The data provided benchmark velocity and turbulent measurements for the portion of the study dwelling on forced convection in complex reactor geometries. In this study, we simulated the same geometry as that in their experiment but excluded the spacers. As shown in the experiment, the thickness of the spacer was small and the measurement domain was chosen to lie between two spacers. Although the existence of spacers would affect the flow distribution, it is still a reasonable step to simulate bare rods inside a duct similar to the experiment of Rehme (1989). Also, it was shown that the simulation results with bare rods are similar to the experimental results.

In the experiment of Smith (2005), the geometry was scaled to be six to seven times larger than typical fuel pins. The rod diameter was 63.5mm and the axial pitch of the ring-cell spacers was 444.5mm. The nominal dimensions of the rectangular flow channel containing the simulated fuel rods were 76.8mm$\times$ 153.7mm. Therefore, the pitch-to-diameter ratio $P/D \approx 1.21$. In the experiment, the streamwise x origin was at the downstream end of the upstream spacer and the domain extended slightly upstream of that point. The measurement domain extended to upstream of the second spacer at $x = 400$mm. The spanwise origin z was centered on the lower rod and the cross stream y axis origin was centered in the channel.

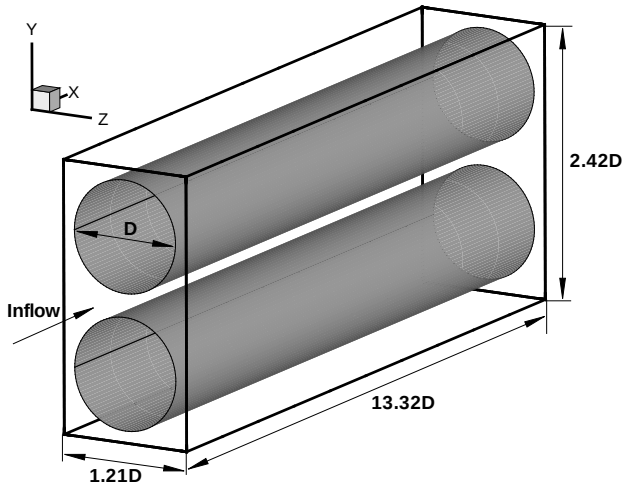

Figure 6.12 Simulation geometry setup for the two rod case.

The simulation configuration was a scaled model of the experimental setup, as shown in Fig. 6.12. The computational domain was $L = 13.32D$ with pitch-to-diameter ratio $P/D = 1.21$, as shown in Fig. 6.13.

A Cartesian grid was generated with $165 \times 180 \times 120$ grid points in the streamwise, vertical and spanwise directions, respectively. To resolve the turbulent structures near the wall, a hyperbolic stretching function was implemented in both vertical and spanwise directions. A bulk Reynolds number, based on the hydraulic diameter $D_h \approx 0.401D$ is $Re = 7648$, was the same as that used in the experiment of Smith (2005). The first grid point away from the wall was 0.51 in terms of wall units $y^+ = yu^*/\nu$. In the streamwise direction the grid was uniformly distributed with $\Delta x^+ = 39.93$ in terms of wall units. No slip boundary conditions were enforced at the four duct walls and a step-periodic boundary condition was assigned at the inflow and outflow boundaries by assuming fully developed flow.

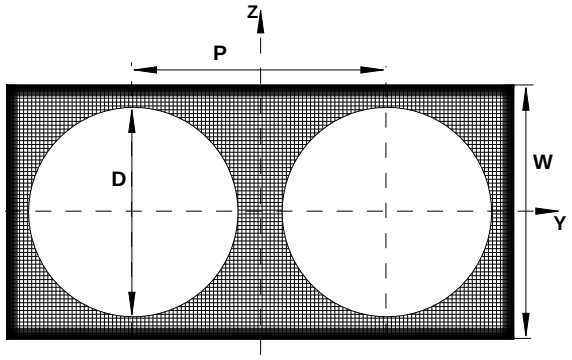

Figure 6.13 Geometry parameters and grid distribution for two rod case.

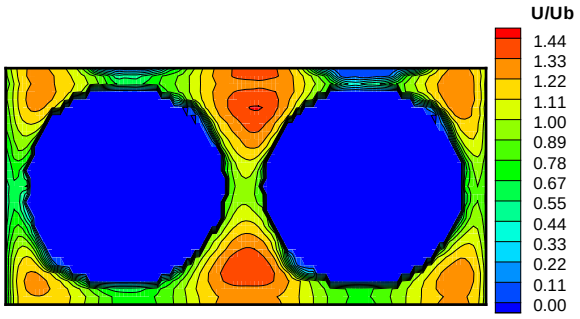

(a) Experimental results (Smith, 2005).

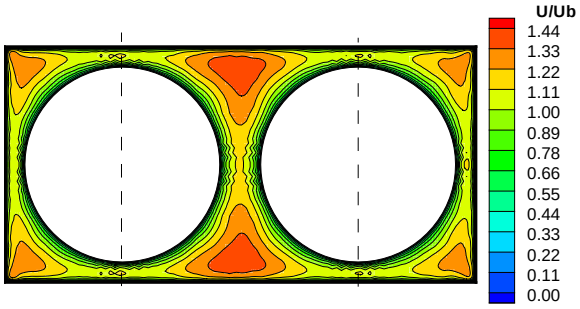

(b) Present simulation results.

Figure 6.14 Mean axial velocity comparison for the two rod case.

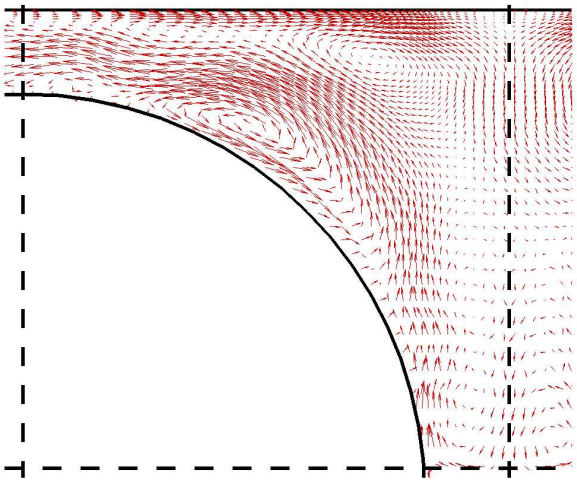

Figure 6.15 Secondary flow patterns between two rods and upper wall.

6.3.3 Results analysis

Figure 6.14 shows the comparison of mean streamwise velocity contours normalized by bulk velocity between experimental and the present simulation results. It is observed from both contour plots that the peak value appears at two locations along the channel bisector between the two rods and is symmetric with respect to the horizontal axis of the duct, as shown in Fig. 6.13. At the four duct corners, the secondary flow features are captured by the current simulation, as shown in Fig. 6.15. Axial velocity distributions along the cross stream $y-$axis obtained in the simulation and experiment are compared in Fig. 6.16, in which the experimental data are extracted from the data file of Smith (2000). The simulation results agree well with experimental data.

Figures 6.17 and 6.18 show the comparison of the simulated axial and cross stream turbulence intensity contours with the experimental results of Smith (2005), in which the contour levels were normalized by the bulk velocity. It was observed from Fig. 6.17 that axial intensities are high near the rod walls and the duct walls, low at the inner subchannels where the mean axial velocities obtain the maximum. In both simulation and experimental results, the axial

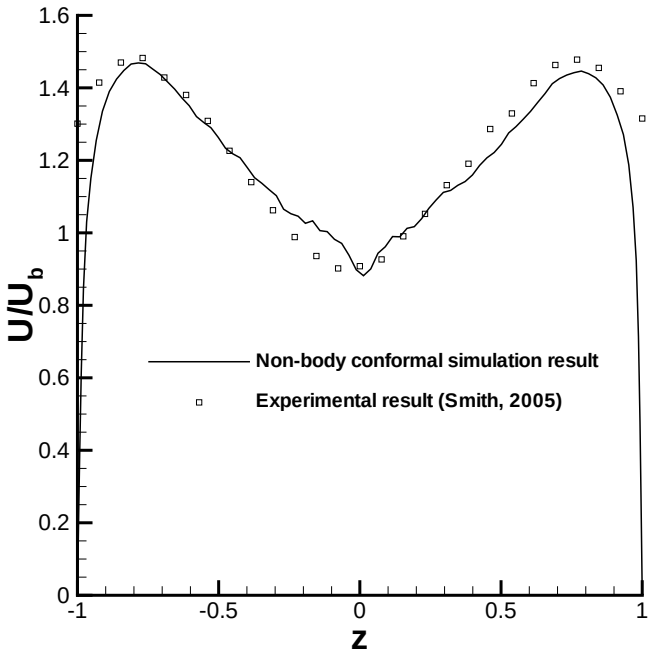

Figure 6.16 Mean axial velocity comparison at the duct center plane.

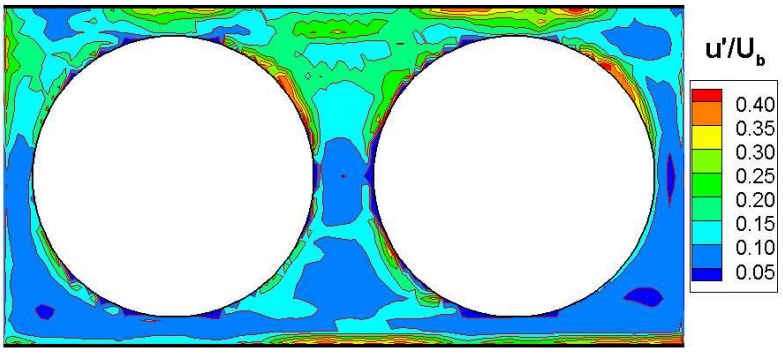

(a) Experimental results at plane $x/L = 0.5$ (Smith, 2005).

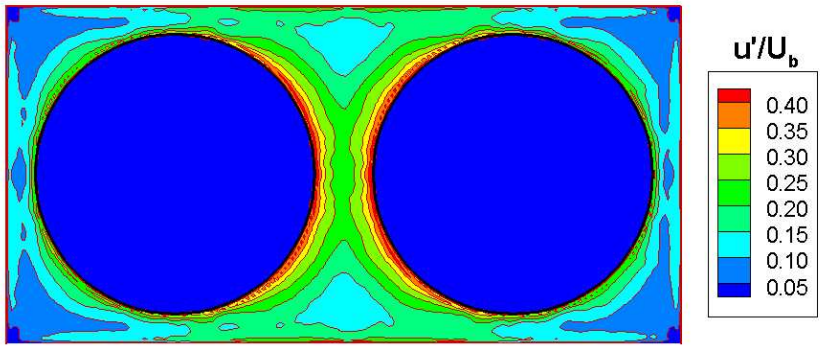

(b) Present simulation results.

Figure 6.17 Axial turbulent intensity comparison for the two rod case.

intensities obtain high values along 45° axes of both rods. The cross stream intensities reach high values along both $z = constant$ walls, while reaching low values at both $y = constant$ walls. However, the relative high value patterns between the two rods observed in the simulation results are not significant in the experimental data. The possible reason is that the cross stream intensity quantities are much smaller compared to the axial ones so that it is not easy to measure. It should be noted that, from both figures, the experimental data are not symmetric with respect to $z = 0$ axis, which makes it almost impossible to obtain an exact match between experimental and simulation results. However, the overall distribution patterns and magnitudes between them are quite good.

Figures 6.19 and 6.20 show the comparison of the Reynolds stress and turbulent kinetic energy contours, in which the contour levels were normalized by the square of bulk velocity. Along the $y-$axis direction, the $u'v'-$component of Reynolds stress contours show alternating signs between the opposite walls in Fig. 6.19, which agree with the general secondary flow patterns. In both experimental and simulation results, the turbulent kinetic energy reached high values at the locations very close to the rod walls and two $z = constant$ walls. The overall agreement of the distribution and magnitude is quite good, although the experimental data are not symmetric with respect to $z = 0$ axis.

6.4 Conclusions

Non-body conformal grids have been successfully employed to simulate compressible flow and complex geometry flow. In the former case, the simulated Mach number shows the compressiblility of the flow and the results compare well with those obtained by Ghias et al. (2007). In the subchannel flow surrounding a rectangular duct and two cylindrical rods, the simulated turbulent statistics show reasonably good agreement with the results from the experiment(Smith, 2005).

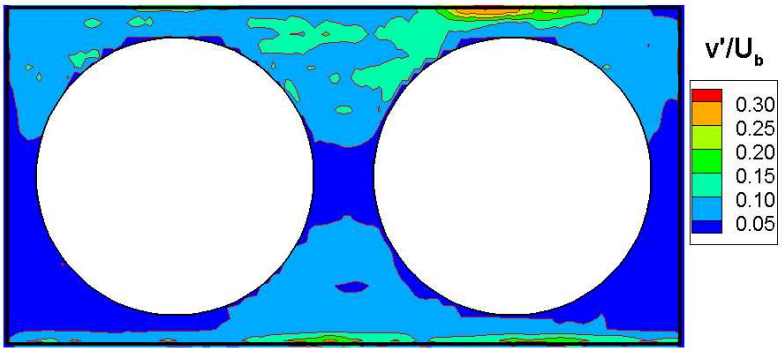

(a) Smith (2005) experimental results at plane $x/L = 0.5$.

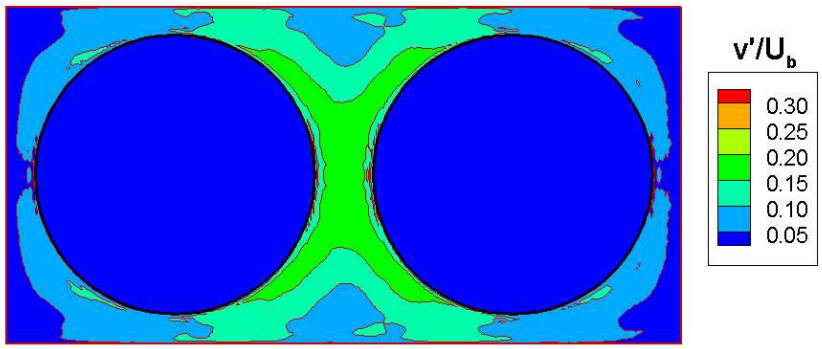

(b) Present simulation results.

Figure 6.18 Cross stream turbulent intensity comparison for the two rod case.

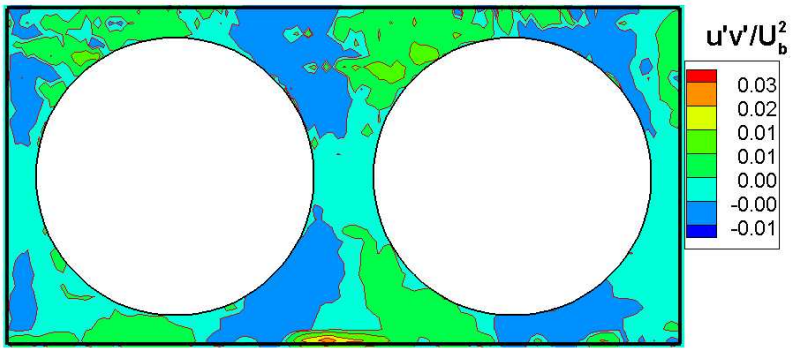

(a) Smith (2005) experimental results at plane $x/L = 0.5$.

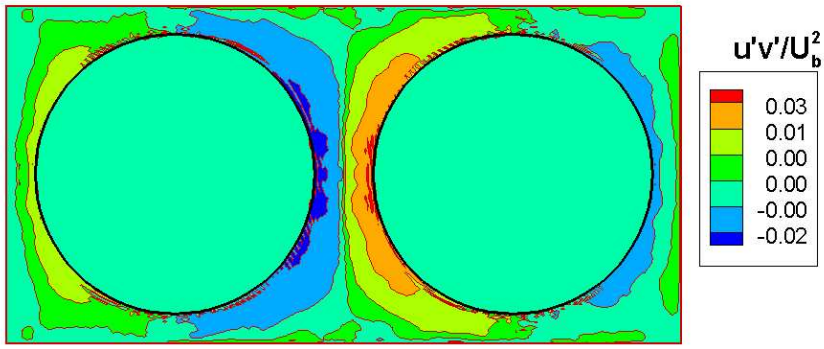

(b) Present simulation results.

Figure 6.19 Reynolds stress comparison for the two rod case.

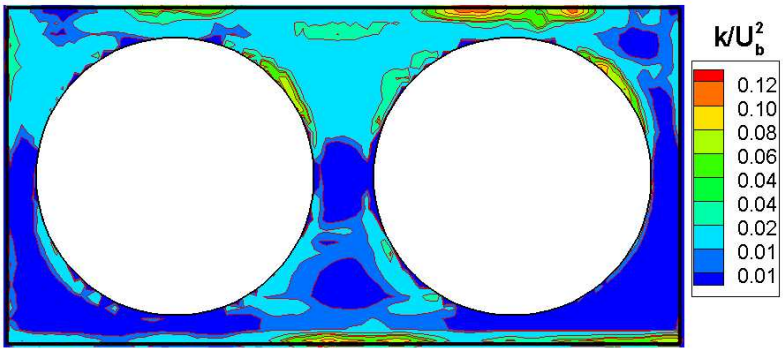

(a) Smith (2005) experimental results at plane $x/L = 0.5$.

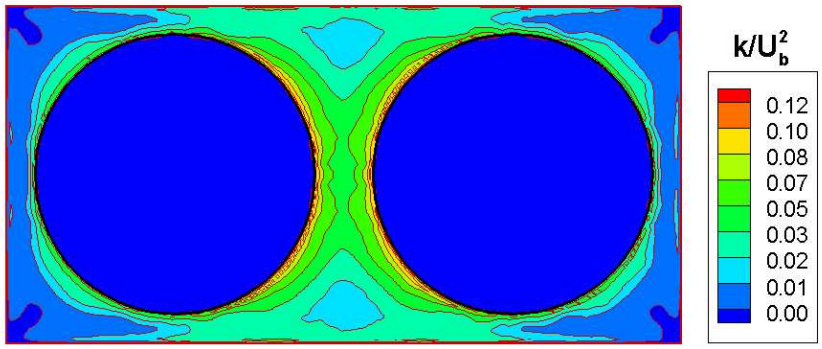

(b) Present simulation results.

Figure 6.20 Turbulent kinetic energy comparison for the two rod case.

CHAPTER 7. MULTISCALE INTERACTION TIME MODEL STUDY OF PARTICLE-LADEN FLOWS WITH DNS

7.1 Introduction

Under the Lagrangian-Eulerian description of turbulent particle flows, the evolution equation for the particle velocity implies a modeled evolution for the droplet distribution function (DDF) of particle fluctuating velocity (Pai and Subramaniam, 2006). The particle velocity evolution equation

$$\frac{d\mathbf{V}_p}{dt} = f(Re_d)\frac{\mathbf{U}_f - \mathbf{V}_p}{\tau_p} + \mathbf{F}_{add} \tag{7.1}$$

represents a class of Lagrangian models widely used in the literature, in which τ_p is the particle response time and F_{add} represents extra forces such as virtual mass force, Basset force and buoyancy force (Crowe et al., 1997). The instantaneous fluid phase velocity $\mathbf{U}_f$ can be decomposed into a mean $\langle \mathbf{U}_f \rangle$ and fluctuation $\mathbf{u}'_f$,

$$\mathbf{U}_f = \langle \mathbf{U}_f \rangle + \mathbf{u}'_f. \tag{7.2}$$

The flutuating fluid phase velocity $\mathbf{u}'_f$ is usually sampled from a joint-normal probability density function with zero mean and covariance $(2k_f/3)\delta_{ij}$ by assuming isotropic turbulence. It was observed by Pai and Subramaniam (2007) that the timescale for interphase TKE transfer is different from that associated with particle dispersion and the trends of these time scales are also different for varying Stokes numbers. Since $\mathbf{u}'_f$ represents a model for the fluctuating fluid-phase velocity that does not represent all the velocity scales that are captured in the DNS velocity field, the drag model based on the particle response time is not capable of capturing the observed trends in the decay of TKE with Stokes number $St_\eta = \tau_p/\tau_\eta$. Therefore, in Pai and Subramaniam (2006) and Xu and Subramaniam (2006), a multiscale interaction time

model (MIM) was proposed based on the equilibration of energy model (EEM) concept and the particle and fluid TKE evolution predicted by the EEM model correctly reproduced the trends with Stokes numbers. In this work, we will study the possibility of applying the MIM model concept to DNS and LES of particle-laden turbulent flows. The basic assumptions include free decaying turbulence, volume fraction $O(10^{-3})$ and mass loading $O(1)$. Due to the low volume fraction, two way coupling was considered but collision was neglected.

7.2 Problem description

In this section, a multiscale interaction time model based on model spectrum is formed and the RANS-MIM model proposed by Xu and Subramaniam (2006) is applied to an isotropic homogeneous flow field. The model timescale is compared to the characteristic fluid timescale and partical response time. It will be shown that the modeled MIM timescale has better capability to capture the multiscale interaction between the particles and flow eddies. In the literature, there are different spectra such as one-dimensional spectra, power-law spectra, Kolmogrov spectra and von Karman spectrum which could be used to initialize the isotropic turbulent field. In this study, we selected the von Karman spectrum for the initialization. The initial parameters include wave number modes, phase shifting coefficients and RK coefficients. Initialization of wave number mode depends on $\kappa_{max}\eta$ and the initial integral length scale, which were specified before the simulation. Based on the description of Pope (2000), the two spatial-resolution requirements $L/L_{11} = 8$ and $\kappa_{max}\eta = 1.5$ determine the necessary number of Fourier modes (or grid nodes), where L is the box side length and L_{11} is longitudinal integral length scale. In this study we chose the box side length $L = 2\pi$ and grid resolution $N^3 = 64 \times 64 \times 64$. Based on the the chosen resolution, other simulation parameters can be determined and they are listed in Table 7.1.

Table 7.1 Simulation parameters

Parameter	Current simulation (64^3)	DNS (Sundaram and Collins, 1999) (128^3)
ν	7.854×10^{-3}	7.854×10^{-3}
$l_e(0)$	1.3812	1.6223
$\eta(0)$	0.0362	0.0384
$\epsilon(0)$	0.282	0.22282
$k_{max}\eta(0)$	2.1845	2.1845
$R_\lambda(0)$	37.45	81.145
$u'(0)$	0.8262	0.9363
$\tau_\eta(0)$	0.16688	0.18774
Δt	0.002	0.0031

Notation: ν is the fluid kinematic viscosity; $l_e(0)$ is the initial large eddy length scale; $\eta(0)$ is the initial Kolmogrov length scale; $\epsilon(0)$ is the initial dissipation rate; $k_{max}\eta(0)$ is the initial resolution of the calculation; $R_\lambda(0)$ is the initial Taylor Reynolds number; $u'(0)$ is the initial turbulent intensity; $\tau_\eta(0)$ is the initial Kolmogrov time scale and Δt is the time step.

7.3 Governing equation and numerical scheme

Starting from the incompressible Navier-Stokes equation in physical space,

$$\frac{\partial u_j}{\partial t} + \frac{\partial (u_j u_k)}{\partial x_k} = -\frac{1}{\rho}\frac{\partial p}{\partial x_j} + \nu \frac{\partial^2 u_j}{\partial x_k x_k} + f_j, \tag{7.3}$$

a Fourier transform $\mathcal{F}_\kappa()$ function was applied to both sides:

$$\frac{d\hat{u}_j}{dt} + \nu\kappa^2 \hat{u}_j = -i\kappa_j \hat{p} - \hat{G}_j + \mathcal{F}_\kappa(f_j), \tag{7.4}$$

where $\hat{p}$ is the Fourier transform of the dynamic pressre p/ρ and $\hat{G}_j$ is the Fourier transform of the nonlinear (convective) term:

$$\begin{aligned}
\hat{G}_j(\kappa, t) &= \mathcal{F}_\kappa\{\frac{\partial (u_j u_k)}{\partial x_k}\} \\
&= i\kappa_k \mathcal{F}_\kappa\{u_j u_k\} \\
&= i\kappa_k \mathcal{F}_\kappa\{(\sum_{\kappa'} \hat{u}_j(\kappa') e^{i\kappa'\cdot\mathbf{x}})(\sum_{\kappa''} \hat{u}_k(\kappa'') e^{i\kappa''\cdot\mathbf{x}})\} \\
&= i\kappa_k \sum_{\kappa'} \hat{u}_j(\kappa')\hat{u}_k(\kappa - \kappa').
\end{aligned} \tag{7.5}$$

A fractional step scheme is used to discretize the governing equation, where the Adams-Bashforth adaptive scheme was used for convective terms and the Crank-Nicholson adaptive

scheme was used for the viscous terms,

$$\frac{\hat{u}_j^* - \hat{u}_j^n}{\Delta t} = -\nu\kappa^2(c_1\hat{u}_j^* + c_2\hat{u}_j^n) - (a_1\hat{G}_j^n + a_2\hat{G}_j^{n-1}) - i\kappa_j\hat{p}^n + \hat{f}_j^{n+1}, \tag{7.6}$$

where the Adams-Bashforth coefficients c_j and Crank-Nicholson coefficients a_j are specified as $c_1 = 0.5; c_2 = 0.5; a_1 = 1.5; a_2 = -0.5$. The calculation of the nonlinear convective term considered the dealiasing effect. Further details on the numerical scheme can be found in Mohd-Yusof (1996). In Fourier space, the pressure Poisson equation was obtained by multiplying both sides of Navier-Stokes equation, Eq. 7.4, by κ_j. Since the flow was assumed to be incompressible, the equation then becomes

$$\kappa^2\hat{p} = \kappa_j\hat{G}_j - \kappa_j\hat{f}_j. \tag{7.7}$$

In the discretized form, the pressure field at timestep n was calculated as

$$\kappa^2\hat{p}^n = \kappa_j(a_1\hat{G}_j^n + a_2\hat{G}_j^{n-1}) - \kappa_j\hat{f}_j^n. \tag{7.8}$$

Then the gradient of pressure $\kappa_j\hat{p}^n$ was calculated and used to update velocity field. With the intermediate velocity $\hat{u}_j^*$ solved from Eq. 7.6, the new velocity $\hat{u}_j^{n+1}$, which satisfies continuity equation, is calculated as,

$$\hat{u}_j^{n+1} = \hat{u}_j^* - \Delta t\nabla\hat{\phi}. \tag{7.9}$$

Then the pressure field is updated with the calculated pressure correction $\hat{\phi}$. The pressure correction was calculated by taking the divergence on both sides of above equation,

$$\Delta t\kappa^2\hat{\phi} = \kappa_j\hat{u}_j^*. \tag{7.10}$$

The pressure field is updated as

$$\hat{p}^{n+1} = \hat{p}^n + \hat{\phi}. \tag{7.11}$$

The particle motion follows

$$\begin{aligned} \frac{d\mathbf{x}_p^n}{dt} &= \mathbf{v}_p^n \\ m_p^n\frac{d\mathbf{v}_p^n}{dt} &= m_p^n\frac{\mathbf{u}(\mathbf{x}_p^n) - \mathbf{v}_p^n}{\tau_p^n} + \sum_{j=1}^{N^3} w_j\mathbf{f}_j. \end{aligned} \tag{7.12}$$

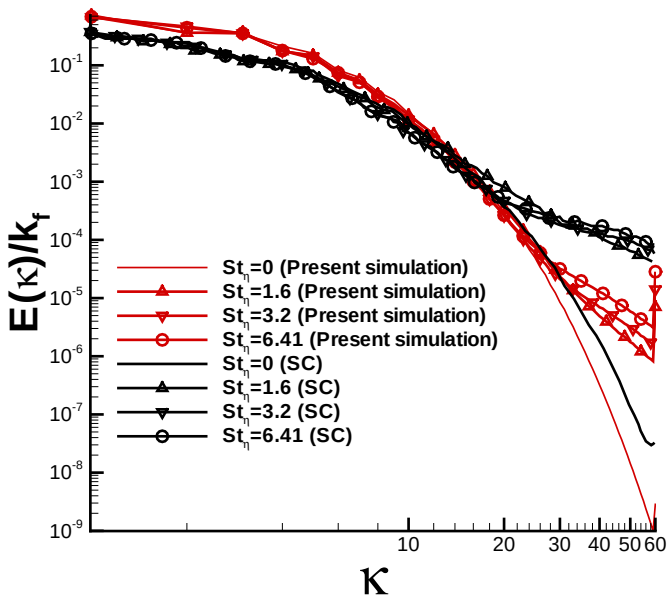

Figure 7.1 Flow energy spectrum comparison: "SC" represents Sundaram and Collins (1999).

7.3.1 Validation of present DNS simulation of turbulent particle-laden flows

Before introducing the MIM model, the current DNS flow solver was validated using the simulation data of Sundaram and Collins (1999). The overall trends of fluid kinetic energy decay and dissipation rate, flow energy spectrum change with respect Stokes number, particle kinetic energy decay and dissipation rate agree well with those from Sundaram and Collins (1999). Fig. 7.1 and 7.2 show the flow energy spectrum and kinetic energy decay comparison, respectively.

7.4 DNS simulation results with MIM model

The basic idea of the multiscale interaction time model proposed by Pai and Subramaniam (2006) and Xu and Subramaniam (2006) is to construct a mean time scale to replace the particle response time in the drag model. First a Stokes number valid in the inertial range was

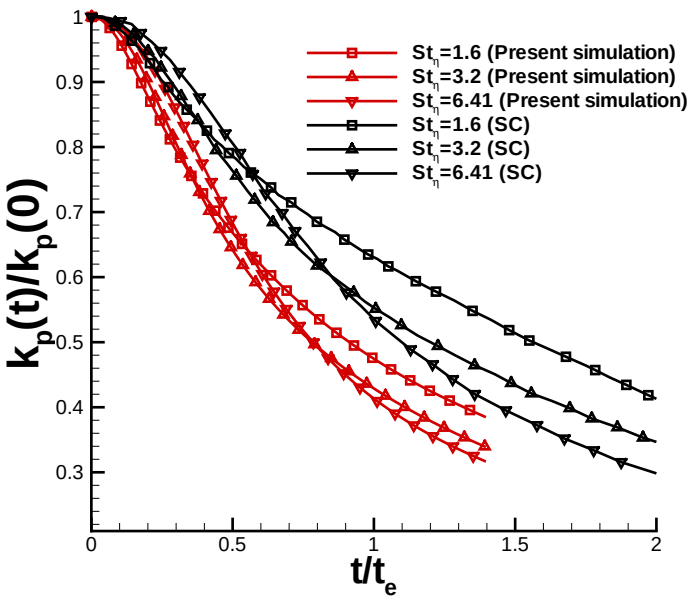

Figure 7.2 Particle energy comparison: "SC" represents Sundaram and Collins (1999).

defined as:

$$St_l = \frac{\tau_p}{\tau_l}, \tag{7.13}$$

where τ_l is defined as

$$\tau_l = \frac{|\mathbf{u}'_f|^2}{\epsilon_f}. \tag{7.14}$$

The velocity fluctuation $\mathbf{u}'_f$ was assumed to obey a joint normal distribution with zero mean and covariance $(2k_f/3)\delta_{ij}$. With this assumption, the probability density function of $|\mathbf{u}'_f|$ is

$$f(z) = \sqrt{\frac{2}{\pi}} \frac{1}{\sigma_f^3} z^2 e^{-z^2/2\sigma_f^2}, \tag{7.15}$$

where $\sigma_f^2 = 2k_f/3$ and z is the sample space variable corresponding to $|\mathbf{u}'_f|$. A mean time scale of interaction τ_{MIM} was derived as

$$\langle \tau_{MIM} \rangle = \int_{z_c}^{\infty} \tau_{MIM} f(z) dz + \int_0^{z_c} \tau_p f(z) dz \tag{7.16}$$

where $z_c = |\mathbf{u}'^*_f|$ and

$$\tau_{MIM} = St_l(\tau_p - \tau) + \tau. \tag{7.17}$$

$|\mathbf{u}_f'^*|$ represents a threshold value of $|\mathbf{u}_f'|$ where a transition of regime happens. τ is the large eddy turnover time scale $\tau = k_f/\epsilon_f$. The basic idea of this model is to separate the eddies with different scales into two regimes based on St_l. For $St_l > 1$, it can be argued that particle responds slowly to the eddies and the time scale of energy transfer is dominated by the particle response time τ_p. If $St_l < 1$, the particle responds immediately to the flow and the time scale of energy transfer is affected more by the eddy turnover time τ. In Eq. 7.16, the region $z \in (0, z_c)$ corresponds to the regime $St_l > 1$ and $z \in (z_c, \infty)$ corresponds to $St_l < 1$, as shown in Fig. 7.3. In this figure, the critical quantity z_c corresponds to the transition of these two regimes with $St_l = 1$ and then $|\mathbf{u}_f'^*|$ can be uniquely determined by the relation

$$|\mathbf{u}_f'^*|^2 = \tau_p \epsilon_f. \tag{7.18}$$

It should be noted that in the limit conditions the above model leads to correct physical behavior of the system. In the limit of $|\mathbf{u}_f'^*| \to 0$, all particles have $St_l < 1$ and they are simply convected by the flow with dominant time scale τ. However, in the limit of $|\mathbf{u}_f'^*| \to \infty$, all particles have $St_l > 1$ and it means no eddies are energetic enough to convect the particle so the dominant time scale of energy transfer is τ_p.

The basic idea of above MIM model is applied to the model spectrum of simulation for isotropic homogeneous turbulence below. In this case, the mean time scale based on wave numbers is defined as

$$\langle \tau \rangle_\kappa = \int_0^\infty \langle \tau | \kappa \rangle f(\kappa) d\kappa, \tag{7.19}$$

with the conditional average $\langle \tau | \kappa \rangle$ defined as

$$\langle \tau | \kappa \rangle = \begin{cases} \tau_p, & \kappa_c \le \kappa < \infty, \\ St_\kappa(\tau_p - \tau), & 0 \le \kappa < \kappa_c. \end{cases} \tag{7.20}$$

In the above equation $\tau = k_f/\epsilon_f$ and the wavenumber based Stokes number is defined as $St_\kappa = \tau_p/\tau(\kappa)$ with

$$\tau(\kappa) = \frac{\int_\kappa^{\kappa+d\kappa} E(\kappa) d\kappa}{2\nu \int_0^\infty \kappa^2 E(\kappa) d\kappa} = \frac{\int_\kappa^{\kappa+d\kappa} E(\kappa) d\kappa}{\epsilon_f}. \tag{7.21}$$

In Eq. 7.20, κ_c is determined from Fig. 7.4 with the separation of regimes concept. κ_c corresponds to $St_\kappa^* = \tau_p/\tau(\kappa) = 1$ therefore κ_c can be determined from Eq. 7.21.

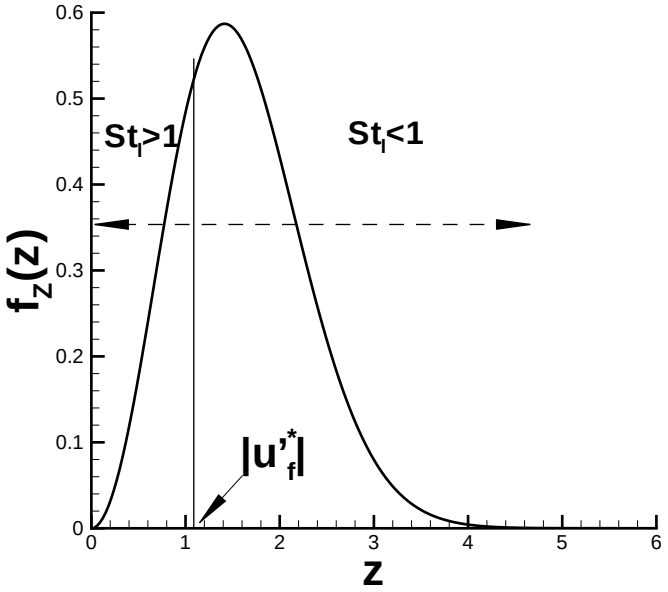

Figure 7.3 Probability function distribution of $|\mathbf{u}'_f|$.

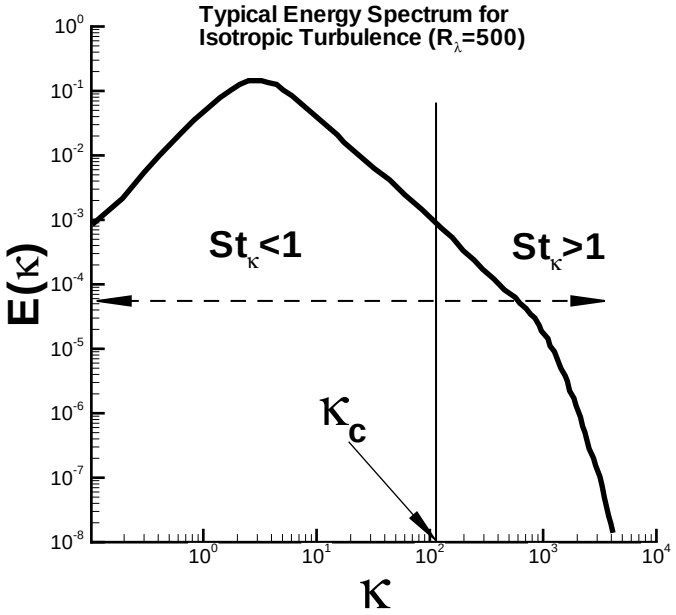

Figure 7.4 Separate regimes in energy spectrum based on St_κ.

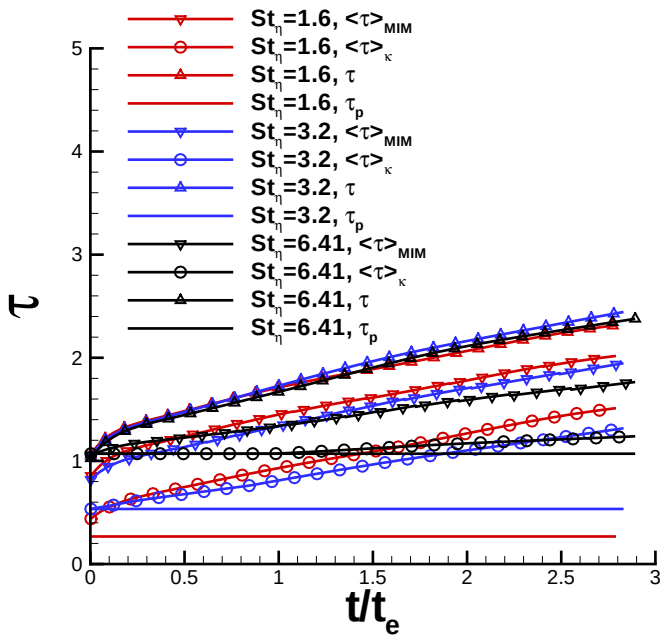

Figure 7.5 Time scales comparison: $\langle\tau\rangle_{MIM}$: mean time scale based on assumed pdf of $\mathbf{u}'_f$; $\langle\tau\rangle_{MIM}$: mean time scale based on energy spectrum; τ: eddy turnover time; τ_p: particle response time.

The results of both mean time scales τ_{MIM} and $\langle\tau\rangle_\kappa$ are shown in Fig. 7.5, compared with particle response time and large eddy turnover time scales. It can be observed that both mean time scales increase with fluid time scale, which corresponds to the trend of limit of $\kappa_c \to \infty$. It means that all particles have $St_\kappa < 1$ and they are convected by the eddies. Therefore the trend of mean time scales matches with the eddy turnover time scale. The evolution trends for both mean time scales agree well with each other.

7.5 MIM model consideration for large eddy simulation of particle laden flows

In this section, the extension of the MIM model to large eddy simulation is discussed. The particle velocity evolution model can be written as

$$\frac{d\mathbf{V}}{dt} = \Omega_p(\mathbf{U} - \mathbf{V}) + \mathbf{F}. \tag{7.22}$$

where Ω_p is a characteristic particle response frequency. The particle response frequency depends on the drag coefficient, C_D, which is a function of particle Reynolds number $Re_p = \frac{\rho_f d|\mathbf{U}-\mathbf{V}|}{\mu_f}$. For the widely used drag models in the literature, Ω can be written as

$$\Omega = \frac{f(Re_p)}{\tau_p}, \tag{7.23}$$

where $f(Re_p)$ represents a functional dependence on Re_p. Particle response time τ_p is given by $(\rho_p d^2)/(18\nu_f\rho_f)$. In LES, the instantaneous fluid-phase velocity $\mathbf{U}$ is decomposed into a filtered quantity, $\overline{\mathbf{U}}$, and a subgrid quantity $\mathbf{u}_{sgs}$ through

$$\mathbf{U} = \overline{\mathbf{U}} + \mathbf{u}_{sgs}.$$

Also, the particle velocity $\mathbf{V}$ can be decomposed into a filtered quantity and a pseudo-subgrid quantity as

$$\mathbf{V} = \overline{\mathbf{V}} + \mathbf{v}_{sgs}.$$

Instead of solving the above equation, we approximately solve the following equations

$$\frac{d\overline{\mathbf{V}}}{dt} = \frac{f(Re)}{\langle\tau\rangle}(\overline{\mathbf{U}} - \mathbf{V}) + \mathbf{F} \tag{7.24}$$

$$\frac{d\mathbf{v}_{sgs}}{dt} = \frac{f(Re)}{\langle\tau\rangle_{sgs}}(\mathbf{u}_{sgs} - \mathbf{v}_{sgs}), \tag{7.25}$$

where $\langle\tau\rangle$ is the mean time scale based on the filtered field and $\langle\tau\rangle_{sgs}$ is the subgrid mean time scale. $\langle\tau\rangle$ can be calculated with a procedure similar to the way $\langle\tau\rangle_{MIM}$ was calculated in the previous section based on the sampled PDF distribution of filtered flow field $\overline{\mathbf{U}}$. Typically, we can assume a Beta-distribution based on the literature about turbulent shear flows. And the subgrid mean time scale $\langle\tau\rangle_{sgs}$ can be approximated with a procedure similar to the way $\langle\tau\rangle_{MIM}$ was calculated in the previous section based on a Gaussian PDF distribution assumption. The detailed model procedure and results analysis will be the future work.

7.6 Conclusion

The DNS-LE solver has been tested and the simulated results compared reasonably well with the results of Sundaram and Collins (1999). The proposed mean time scale based on model

spectrum showed the similar trend to that calculated from an assumed PDF model. Generally, as turbulence decays, the characteristic fluid time scale increases. Therefore, the particles initially having large response time will change their interaction modes with the fluid time scale. If at the beginning the particle response time is significantly larger than the Kolmogrov time scale, the particles generally don't follow the fluid particle path. As turbulence decays, those particles will tend to be more easily convected by the fluid eddies.

CHAPTER 8. CONCLUSIONS AND RECOMMENDATIONS

The objective of the present study is the development of a non-body conformal grid method and its implementation in a compressible flow solver. Brief conclusions and recommendations for future related work are given in this chapter.

8.1 Summary

A non-body conformal grid method was incorporated into the large eddy simulations solver to simulate geometrically complex turbulent flows. The scheme was developed based on the fixed Cartesian grids which significantly simplifies the grid generation procedure.

In terms of the validation and application of the solver, a variety of flow problems including low to high Reynolds numbers, external and internal flows, incompressible and compressible flow were considered. First, the formal accuracy of the current solver was established for the problem of flow over a cylinder. Then flow over a cylinder with different Reynolds numbers was simulated and characteristic parameters were compared to those from the literature (experiments and simulation). The method developed was found to reproduce all features of the flow, compared to the referenced body-conformal grid simulations and experiments. Turbulent isothermal pipe flow was simulated with non-body conformed grids to validate the capability of the current solver for turbulent flow simulations. The turbulent statistical results were compared with body-fitted grid method data and good agreement was observed. By using this method, a rectangular duct flow containing a cylindrical rod was simulated and the turbulent statistics were compared with the results from other investigators. The comparison with experiments of Guellouz and Tavoularis (2000) shows better agreement for mean streamwise velocity distribution than the URANS simulation of Chang and Tavoularis (2005). The

axial turbulent intensities and turbulent kinetic energy show reasonable agreement with the experimental results of Guellouz and Tavoularis (2000).

Flow over a heated cylinder at different Reynolds numbers and temperature ratio conditions was simulated using the developed methodology. The Nusselt number study with $Re_D = 40, 80, 100, 120, 150$ demonstrated the accuracy and consistency of the current method. The local distribution of Nusselt number along the cylindrical surface agreed with the experimental and reference numerical simulation satisfactorily. As the temperature ratio increased, the drag coefficients increased and the magnitude and frequency of lift coefficients decreased, which reflects the laminarization tendency of the flow. Also, the temperature contours showed that the temperature at the center of the first vortex was very close to the effective temperature defined in the literature.

The turbulent pipe flow simulation obtained with the current non-body conformal grid method demonstrated the capability of this solver to simulate turbulent heat transfer problems. Two ways of imposing the uniform heat flux wall boundary condition was investigated. The nondimensional temperature statistics show a good agreement with DNS and LES data, where the mesh is aligned with the wall normal direction. In the near wall region, the temperature fluctuations compared well with DNS results, while it was slightly overpredicted with the specified wall heat flux boundary condition. Good agreement with DNS results was obtained for both the streamwise and wall-normal turbulent heat fluxes. The friction coefficients and Nusselt numbers agreed with the constant property empirical correlations within the uncertainty level usually ascribed to the correlations for turbulent flows with heat transfer.

Finally, non-body conformal grids have been successfully employed to simulate compressible flow and complex geometry flow. In the former case, the simulated Mach number shows the compressiblility of the flow and the results compare well with that by Ghias et al. (2007). In the subchannel flow surrounding a rectangular duct and two cylindrical rods, the simulated turbulent statistics show reasonably good agreement with the results from the experiment(Smith, 2005).

8.2 Contributions

- Developed a non-body conformal grid method within the framework of a compressible large eddy simulation solver.
- Validated the capability and order of accuracy of the non-body conformal grid method for the simulation of laminar and transition flows.
- Investigated the turbulent characteristics of duct sub-channel flows with the non-body conformal grid method.
- Extended the developed solver to simulate heat transfer problems for both external and internal flows.
- Studied the flow properties with Mach number with the developed non-body conformal grid method.
- Studied the MIM model based on wave spectrum for homogeneous isotropic turbulence.

8.3 Recommendations for Future Work

It was shown in the present study that the non-body conformal grid method helped simplifying the grid generation procedure for complex flows. A limiting factor in all these methods is the inflexibility in clustering grid points near a complex body. As the Reynolds number increases, more grid points are required to resolve the thinner boundary layer near the body. To investigate if they are still cost efficient compared to a body-fitted grid forulations, one needs to look at the rate of increase of the total number of grid points for both categories of methods as a function of Reynolds number. In general, for a single body simulation, the use of body-fitted grid method often only requires grid refinement in the the wall-normal direction, while two or three direction grid refinment is often required for the a non-body conformal grid method. As a result the required number of grid points increases faster for non-body conformal grid method. A possible remedy for this problem is to add grid adaptivity into the non-body conformal solver. A similar implementation has been carried out by the classical immersed boundary method (Lai and Peskin, 2002) and the Cartesian grid method. In the near future, the major development of the current work can be summarized as follows:

- Implement the grid adaptation capability into the current solver.
- Combine the non-body conformal grid method with wall models to tackle very high Reynolds number flows in complex geometries.
- Develop a general fluid-structure interaction solver for moving boundary problems.

APPENDIX A. JACOBIAN MATRICES

The transformation matrix between the conservative and the primitive variables (see Eq. 2.63) is

$$[T] = \begin{bmatrix} 1/\tilde{T} & 0 & 0 & 0 & -\tilde{p}/\tilde{T}^2 \\ \tilde{u}/\tilde{T} & \tilde{p}/\tilde{T} & 0 & 0 & -\tilde{p}\tilde{u}/\tilde{T}^2 \\ \tilde{v}/\tilde{T} & 0 & \tilde{p}/\tilde{T} & 0 & -\tilde{p}\tilde{v}/\tilde{T}^2 \\ \tilde{w}/\tilde{T} & 0 & 0 & \tilde{p}/\tilde{T} & -\tilde{p}\tilde{w}/\tilde{T}^2 \\ c_v + \tilde{K}/\tilde{T} & \tilde{p}\tilde{u}/\tilde{T} & \tilde{p}\tilde{u}/\tilde{T} & \tilde{p}\tilde{w}/\tilde{T} & -(\tilde{p}\tilde{K})/\tilde{T}^2 \end{bmatrix}, \tag{A.1}$$

where $\tilde{K} = \frac{1}{2}(\tilde{u}^2 + \tilde{v}^2 + \tilde{w}^2)$.

Its inverse is

$$[T]^{-1} = \begin{bmatrix} \tilde{K}/c_v & -\tilde{u}/c_v & -\tilde{v}/c_v & -\tilde{w}/c_v & 1/c_v \\ -\tilde{u}\tilde{T}/\tilde{p} & \tilde{T}/\tilde{p} & 0 & 0 & 0 \\ -\tilde{v}\tilde{T}/\tilde{p} & 0 & \tilde{T}/\tilde{p} & 0 & 0 \\ -\tilde{w}\tilde{T}/\tilde{p} & 0 & 0 & \tilde{T}/\tilde{p} & 0 \\ (\tilde{T}/\tilde{p})[\tilde{K}/c_v - \tilde{T}] & -\tilde{u}\tilde{T}/(\tilde{p}c_v) & -\tilde{v}\tilde{T}/(\tilde{p}c_v) & -\tilde{w}\tilde{T}/(\tilde{p}c_v) & \tilde{T}/(\tilde{p}c_v) \end{bmatrix} \tag{A.2}$$

The preconditiong matrix (see Eq. 2.83) is

$$[\Gamma] = \begin{bmatrix} R/\tilde{T} & 0 & 0 & 0 & -\tilde{p}/\tilde{T}^2 \\ R\tilde{u}/\tilde{T} & \tilde{p}/\tilde{T} & 0 & 0 & -\tilde{p}\tilde{u}/\tilde{T}^2 \\ R\tilde{v}/\tilde{T} & 0 & \tilde{p}/\tilde{T} & 0 & -\tilde{p}\tilde{v}/\tilde{T}^2 \\ R\tilde{w}/\tilde{T} & 0 & 0 & \tilde{p}/\tilde{T} & -\tilde{p}\tilde{w}/\tilde{T}^2 \\ R\left[c_v + \tilde{K}/\tilde{T}\right] & \tilde{p}\tilde{u}/\tilde{T} & \tilde{p}\tilde{v}/\tilde{T} & \tilde{p}\tilde{w}/\tilde{T} & -(\tilde{p}\tilde{K}/\tilde{T}^2) \end{bmatrix} \tag{A.3}$$

Its inverse is

$$[\Gamma]^{-1} = \begin{bmatrix} \tilde{K}/Rc_v & -\tilde{u}/(Rc_v) & -\tilde{v}/(Rc_v) & -\tilde{w}/(Rc_v) & 1/(Rc_v) \\ -\tilde{u}\tilde{T}/\tilde{p} & \tilde{T}/\tilde{p} & 0 & 0 & 0 \\ -\tilde{v}\tilde{T}/\tilde{p} & 0 & \tilde{T}/\tilde{p} & 0 & 0 \\ -\tilde{w}\tilde{T}/\tilde{p} & 0 & 0 & \tilde{T}/\tilde{p} & 0 \\ (\tilde{T}/\tilde{p})[\tilde{K}/c_v - \tilde{T}] & -\tilde{u}\tilde{T}/(\tilde{p}c_v) & -\tilde{v}\tilde{T}/(\tilde{p}c_v) & -\tilde{w}\tilde{T}/(\tilde{p}c_v) & \tilde{T}/(\tilde{p}c_v) \end{bmatrix} \tag{A.4}$$

The flux Jacobian matrices (see Eq. 2.86) are

$$[A] = \begin{bmatrix} \tilde{u}/\tilde{T} & \tilde{p}/\tilde{T} & 0 & 0 & -\tilde{p}\tilde{u}/\tilde{T}^2 \\ \tilde{u}^2/\tilde{T} + R & 2\tilde{p}\tilde{u}/\tilde{T} & 0 & 0 & -\tilde{p}\tilde{u}^2/\tilde{T}^2 \\ \tilde{u}\tilde{v}/\tilde{T} & \tilde{p}\tilde{v}/\tilde{T} & \tilde{p}\tilde{u}/\tilde{T} & 0 & -\tilde{p}\tilde{u}\tilde{v}/\tilde{T}^2 \\ \tilde{u}\tilde{w}/\tilde{T} & \tilde{p}\tilde{w}/\tilde{T} & 0 & \tilde{p}\tilde{u}/\tilde{T} & -\tilde{p}\tilde{u}\tilde{w}/\tilde{T}^2 \\ \tilde{u}\hat{H}/\tilde{T} & (\tilde{p}/\tilde{T})(\hat{H} + \tilde{u}^2) & \tilde{p}\tilde{u}\tilde{v}/\tilde{T} & \tilde{p}\tilde{u}\tilde{w}/\tilde{T} & -(\tilde{p}\tilde{u}\tilde{K})/\tilde{T}^2 \end{bmatrix} \tag{A.5}$$

$$[B] = \begin{bmatrix} \tilde{v}/\tilde{T} & 0 & \tilde{p}/\tilde{T} & 0 & -\tilde{p}\tilde{v}/\tilde{T}^2 \\ \tilde{v}\tilde{u}/\tilde{T} & \tilde{p}\tilde{v}/\tilde{T} & \tilde{p}\tilde{u}/\tilde{T} & 0 & -\tilde{p}\tilde{v}\tilde{u}/\tilde{T}^2 \\ \tilde{v}^2/\tilde{T} + R & 0 & 2\tilde{p}\tilde{v}/\tilde{T} & 0 & -\tilde{p}\tilde{v}^2/\tilde{T}^2 \\ \tilde{v}\tilde{w}/\tilde{T} & 0 & \tilde{p}\tilde{w}/\tilde{T} & \tilde{p}\tilde{v}/\tilde{T} & -\tilde{p}\tilde{v}\tilde{w}/\tilde{T}^2 \\ \tilde{v}\hat{H}/\tilde{T} & \tilde{p}\tilde{v}\tilde{u}/\tilde{T} & (\tilde{p}/\tilde{T})(\hat{H} + \tilde{v}^2) & \tilde{p}\tilde{v}\tilde{w}/\tilde{T} & -(\tilde{p}\tilde{v}\tilde{K})/\tilde{T}^2 \end{bmatrix} \tag{A.6}$$

$$[C] = \begin{bmatrix} \tilde{w}/\tilde{T} & 0 & 0 & \tilde{p}/\tilde{T} & -\tilde{p}\tilde{w}/\tilde{T}^2 \\ \tilde{w}\tilde{u}/\tilde{T} & \tilde{p}\tilde{w}/\tilde{T} & 0 & \tilde{p}\tilde{u}/\tilde{T} & -\tilde{p}\tilde{w}\tilde{u}/\tilde{T}^2 \\ \tilde{w}\tilde{v}/\tilde{T} & 0 & \tilde{p}\tilde{w}/\tilde{T} & \tilde{p}\tilde{v}/\tilde{T} & -\tilde{p}\tilde{w}\tilde{v}/\tilde{T}^2 \\ \tilde{w}^2/\tilde{T} + R & 0 & 0 & 2\tilde{p}\tilde{w}/\tilde{T} & -\tilde{p}\tilde{w}^2/\tilde{T}^2 \\ \tilde{w}\hat{H}/\tilde{T} & \tilde{p}\tilde{w}\tilde{u}/\tilde{T} & \tilde{p}\tilde{w}\tilde{v}/\tilde{T} & (\tilde{p}/\tilde{T})(\hat{H} + \tilde{w}^2) & -(\tilde{p}\tilde{w}\tilde{K})/\tilde{T}^2 \end{bmatrix} \tag{A.7}$$

where

$$\hat{H} = c_p\tilde{T} + \frac{1}{2}(\tilde{u}^2 + \tilde{v}^2 + \tilde{w}^2) \tag{A.8}$$

APPENDIX B. MATRICES FOR NAVIER-STOKES EQUATION CHARACTERISTIC BOUNDARY CONDITIONS

Based on the formulas of $[T]^{-1}$ and $[A]$ in Appendix A, we have

$$[T]^{-1}[A] = \begin{bmatrix} u & \gamma p & 0 & 0 & 0 \\ 1/\rho & u & 0 & 0 & 0 \\ 0 & 0 & u & 0 & 0 \\ 0 & 0 & 0 & u & 0 \\ 0 & (\gamma-1)T & 0 & 0 & u \end{bmatrix} \tag{B.1}$$

where γ is the specific heat ratio $\gamma = c_p/c_v = 1 + R/c_v$.

Let $[T]^{-1}[A] = [S][\Lambda][S]^{-1}$, where $[\Lambda]$ is a diagonal matrix with elements which are eigenvalues of $[T]^{-1}[A]$, then the rows of $[S]^{-1}$ are the corresponding eigenvectors.

$$[\Lambda] = \begin{bmatrix} u+c & 0 & 0 & 0 & 0 \\ 0 & u-c & 0 & 0 & 0 \\ 0 & 0 & u & 0 & 0 \\ 0 & 0 & 0 & u & 0 \\ 0 & 0 & 0 & 0 & u \end{bmatrix} \tag{B.2}$$

where c is the local sound speed which is $c = \sqrt{\gamma RT}$.

The eigenvector matrix $[S]$ is

$$[S] = \begin{bmatrix} \frac{p}{T}\frac{\gamma}{(\gamma-1)} & -\frac{p}{T}\frac{\gamma}{(\gamma-1)} & 0 & 0 & 0 \\ \frac{c}{(\gamma-1)T} & -\frac{c}{(\gamma-1)T} & 0 & 0 & 0 \\ 0 & 0 & 0 & 1 & 0 \\ 0 & 0 & 0 & 0 & 1 \\ 1 & 1 & 1 & 0 & 0 \end{bmatrix} \tag{B.3}$$

and its inverse is

$$[S]^{-1} = \begin{bmatrix} \frac{(\gamma-1)T}{(2\gamma p)} & \frac{(\gamma-1)T}{2c} & 0 & 0 & 0 \\ \frac{(\gamma-1)T}{(2\gamma p)} & -\frac{(\gamma-1)T}{2c} & 0 & 0 & 0 \\ -\frac{(\gamma-1)T}{(\gamma p)} & 0 & 0 & 0 & 1 \\ 0 & 0 & 1 & 0 & 0 \\ 0 & 0 & 0 & 1 & 0 \end{bmatrix} \tag{B.4}$$

My eigenvector matrix $[S]$ is

$$[S] = \begin{bmatrix} (p\gamma)/c & (p\gamma)/c & 0 & 0 & 0 \\ 1 & -1 & 0 & 0 & 0 \\ 0 & 0 & 1 & 0 & 0 \\ 0 & 0 & 0 & 1 & 0 \\ T(\gamma-1)/c & T(\gamma-1)/c & 0 & 0 & 1 \end{bmatrix} \tag{B.5}$$

and its inverse is

$$[S]^{-1} = \begin{bmatrix} c/(2\gamma p) & 1/2 & 0 & 0 & 0 \\ c/(2\gamma p) & -1/2 & 0 & 0 & 0 \\ 0 & 0 & 1 & 0 & 0 \\ 0 & 0 & 0 & 1 & 0 \\ -T(\gamma-1)/(\gamma p) & 0 & 0 & 0 & 1 \end{bmatrix} \tag{B.6}$$

The wave vector $\mathcal{L}$ is defined by

$$\mathcal{L} = [\Lambda][S]^{-1}\frac{\partial \mathbf{W}}{\partial x} \tag{B.7}$$

. The matrix $[\Lambda][S]^{-1}$ is

$$[\Lambda][S]^{-1} = \begin{bmatrix} (u+c)(\gamma-1)T/(2\gamma p) & (u+c)(\gamma-1)T/(2c) & 0 & 0 & 0 \\ (u-c)(\gamma-1)T/(2\gamma p) & -(u-c)(\gamma-1)T/(2c) & 0 & 0 & 0 \\ -u(\gamma-1)T/(\gamma p) & 0 & 0 & 0 & u \\ 0 & 0 & u & 0 & 0 \\ 0 & 0 & 0 & u & 0 \end{bmatrix} \tag{B.8}$$

and its inverse is

$$[S][\Lambda]^{-1} = \begin{bmatrix} \frac{p}{(u+c)T}\frac{\gamma}{\gamma-1} & \frac{p}{(u-c)T}\frac{\gamma}{\gamma-1} & 0 & 0 & 0 \\ \frac{c}{(u+c)(\gamma-1)T} & -\frac{c}{(u-c)(\gamma-1)T} & 0 & 0 & 0 \\ 0 & 0 & 0 & 1/u & 0 \\ 0 & 0 & 0 & 0 & 1/u \\ 1/(u+c) & 1/(u-c) & 1/u & 0 & 0 \end{bmatrix} \tag{B.9}$$

In my derivation, the matrix $[\Lambda][S]^{-1}$ is

$$[\Lambda][S]^{-1} = \begin{bmatrix} (u+c)c/(2\gamma p) & (u+c)/2 & 0 & 0 & 0 \\ (u-c)c/(2\gamma p) & -(u-c)/2 & 0 & 0 & 0 \\ 0 & 0 & u & 0 & 0 \\ 0 & 0 & 0 & u & 0 \\ -u(\gamma-1)T/(\gamma p) & 0 & 0 & 0 & u \end{bmatrix} \tag{B.10}$$

and its inverse is

$$[S][\Lambda]^{-1} = \begin{bmatrix} (p\gamma)/[(u+c)c] & (p\gamma)/[(u-c)c] & 0 & 0 & 0 \\ 1/(u+c) & -1/(u-c) & 0 & 0 & 0 \\ 0 & 0 & 1/u & 0 & 0 \\ 0 & 0 & 0 & 1/u & 0 \\ T(\gamma-1)/[c(u+c)] & T(\gamma-1)/[c(u-c)] & 0 & 0 & 1/u \end{bmatrix} \tag{B.11}$$

APPENDIX C. NAVIER-STOKES CHARACTERISTIC BOUNDARY CONDITION

C.1 Transformation to Characteristic Form

The starting point of analysis for the development of boundary conditions is Eq. (C.1).

$$[T]\frac{\partial \mathbf{W}}{\partial t} + [A]\frac{\partial \mathbf{W}}{\partial x} = \mathbf{C} - \left[\frac{\partial(\mathbf{F}_{1,vis} + \mathbf{F}_{1,sgs})}{\partial x} + \frac{\partial \mathbf{F}_2}{\partial y} + \frac{\partial \mathbf{F}_3}{\partial z}\right] = \mathbf{C}', \tag{C.1}$$

where the analysis in the x direction was chosen for convenience. The choice depends on which direction of wave propagation is of interest. For example, if one wants to impose NSCBC at the outlet of a duct, the equation should be recast in the streamwise direction. If instead one hopes to apply NSCBC to the solid wall, then it is the y and/or z directions which should be modified.

By multiplying by $[T]^{-1}$ the above equation becomes

$$\frac{\partial \mathbf{W}}{\partial t} + [T]^{-1}[A]\frac{\partial \mathbf{W}}{\partial x} = [T]^{-1}\mathbf{C}', \tag{C.2}$$

Let $[T]^{-1}[A] = [S][\Lambda][S]^{-1}$, where $[\Lambda]$ is a diagonal matrix with elements that are eigenvalues of $[T]^{-1}[A]$, then the rows of $[S]^{-1}$ are the corresponding left eigenvectors $\mathbf{l}_i^T$. Similarly, the columns of matrix $[S]$ are the right eigenvectors $\mathbf{r}_j$. Multiplying Eq. (C.2) by $[S]^{-1}$, we have

$$[S]^{-1}\frac{\partial \mathbf{W}}{\partial t} + [\Lambda][S]^{-1}\frac{\partial \mathbf{W}}{\partial x} = [S]^{-1}[T]^{-1}\mathbf{C}', \tag{C.3}$$

whose m components are

$$\mathbf{l}_i^T\left(\frac{\partial \mathbf{W}}{\partial t} + \lambda_i\frac{\partial \mathbf{W}}{\partial x}\right) = \mathbf{l}_i^T\mathbf{C}^*, \quad i = 1, ..., m, \tag{C.4}$$

and $\mathbf{C}^* = [T]^{-1}\mathbf{C}'$. If we define a vector

$$\mathcal{L} = \lambda_i\mathbf{l}_i^T\frac{\partial \mathbf{W}}{\partial x}, \tag{C.5}$$

and multiplying Eq. C.3 by $[S]$ giving,

$$\frac{\partial \mathbf{W}}{\partial t} + [S]\mathcal{L} = \mathbf{C}^*, \tag{C.6}$$

It can be observed that in fact $\mathcal{L}$ is another expression for the convection terms, and each component of $\mathcal{L}$ is either an incoming or an outgoing wave, depending on the sign of its eigenvalue. For an ideal gas, the five eigenvalues are $(u+c, u-c, u, u, u)$ where c is the local sound speed. In a subsonic flow, $|u| < c$, then there should exist at least one incoming wave at the outlet and typically four incoming waves at the inlet. The outgoing waves can be directly computed from Eq. (C.5) with a one-sided difference that uses grid points on the interior side of the boundary. As described in Thompson (1990), the number of boundary conditions which must be specified at a point on the boundary is equal to the number of incoming waves at that point. We need to specify boundary conditions which determine the value of $\mathcal{L}_i$ for incoming waves and compute from definition (C.5) the values of $\mathcal{L}_i$ for outgoing waves.

C.1.0.1 Local One-Dimensional Inviscid Assumption

The matrices involved in the procedure described in the last section are listed in Appendix B. Based on the definition of $\mathcal{L}$ C.5 With the results shown in Appendix B, we have

$$\mathcal{L} = \begin{bmatrix} \mathcal{L}_1 \\ \mathcal{L}_2 \\ \mathcal{L}_3 \\ \mathcal{L}_4 \\ \mathcal{L}_5 \end{bmatrix} = \begin{bmatrix} (u+c)(\frac{c}{2\gamma p}\frac{\partial p}{\partial x} + \frac{\partial u}{2\partial x}) \\ (u-c)(\frac{c}{2\gamma p}\frac{\partial p}{\partial x} - \frac{\partial u}{2\partial x}) \\ u\frac{\partial v}{\partial x} \\ u\frac{\partial w}{\partial x} \\ u\left[\frac{\partial T}{\partial x} - \frac{(\gamma-1)T}{\gamma p}\frac{\partial p}{\partial x}\right] \end{bmatrix}; \quad [S]\mathcal{L} = \begin{bmatrix} \frac{p\gamma}{c}(\mathcal{L}_1 + \mathcal{L}_2) \\ (\mathcal{L}_1 - \mathcal{L}_2) \\ \mathcal{L}_3 \\ \mathcal{L}_4 \\ \frac{T(\gamma-1)}{c}(\mathcal{L}_1 + \mathcal{L}_2) + \mathcal{L}_5 \end{bmatrix}. \tag{C.7}$$

And by virtue of Eq. (C.6), $[S]\mathcal{L}$ is related to the time derivatives of the primitive variables which can be subject to physical boundary conditions. One major simplification is reached by using the so-called local one-dimensional inviscid (LODI) assumption, which argues that the source term on the right hand side of Eq. (C.6) can be ignored for the current purpose. In terms of the primitive variables we chose, this LODI system is

$$\frac{\partial p}{\partial t} \quad + \quad \frac{p\gamma}{c}(\mathcal{L}_1 + \mathcal{L}_2) = 0; \tag{C.8}$$

$$\frac{\partial u}{\partial t} + (\mathcal{L}_1 - \mathcal{L}_2) = 0; \tag{C.9}$$

$$\frac{\partial v}{\partial t} + \mathcal{L}_3 = 0; \tag{C.10}$$

$$\frac{\partial w}{\partial t} + \mathcal{L}_4 = 0; \tag{C.11}$$

$$\frac{\partial T}{\partial t} + \frac{T(\gamma-1)}{c}(\mathcal{L}_1 + \mathcal{L}_2) + \mathcal{L}_5 = 0. \tag{C.12}$$

Based on Eq. (C.7), all gradients normal to the boundary may be expressed as functions of the $\mathcal{L}_i$s:

$$\frac{\partial p}{\partial x} = \frac{p\gamma}{c}\left[\frac{\mathcal{L}_1}{u+c} + \frac{\mathcal{L}_2}{u-c}\right]; \tag{C.13}$$

$$\frac{\partial u}{\partial x} = \left[\frac{\mathcal{L}_1}{u+c} - \frac{\mathcal{L}_2}{u-c}\right]; \tag{C.14}$$

$$\frac{\partial v}{\partial x} = \frac{\mathcal{L}_3}{u}; \tag{C.15}$$

$$\frac{\partial w}{\partial x} = \frac{\mathcal{L}_4}{u}; \tag{C.16}$$

$$\frac{\partial T}{\partial x} = \frac{\mathcal{L}_1}{u+c} + \frac{\mathcal{L}_2}{u-c} + \frac{c}{(\gamma-1)T}\frac{\mathcal{L}_5}{u}. \tag{C.17}$$

The previous relations may be combined to express the time derivatives of other quantities of interest. For instance

$$\frac{\partial \rho}{\partial t} + \frac{\rho}{c}(\mathcal{L}_1 + \mathcal{L}_2) - \frac{\rho(\gamma-1)}{c}\mathcal{L}_5 = 0; \tag{C.18}$$

$$\frac{\partial(\dot{m}/A_c)}{\partial t} + \rho[(1+\mathcal{M})\mathcal{L}_1 + (\mathcal{M}-1)\mathcal{L}_2 - \mathcal{M}(\gamma-1)\mathcal{L}_5] = 0, \tag{C.19}$$

where $\frac{\dot{m}}{A_c} = \rho u$ is the local mass flow rate and $\mathcal{M} = u/c$ is the local Mach number. Most physical boundary conditions have a counterpart LODI relation. For example, imposing a constant inlet pressure should be accomplished (from Eq. (C.8)) by setting $\mathcal{L}_2 = \mathcal{L}_1$ to fix the amplitude variation of the pressure wave entering the domain.

C.1.0.2 NSCBC Strategy for Euler and Navier-Stokes Equations

From theoretical studies (Strikwerda, 1977; Oliger and Sundström, 1978), we know a certain number of physical boundary conditions are needed for the well-posedness of these two types of equations. The results are shown in Table C.1. The main strategy of NSCBC involves three steps:

Table C.1 Number of physical boundary conditions needed for well-posedness of 3-D Euler and Navier-Stokes equations Poinsot and Lele (1992)

Boundary Conditions	Euler	Navier-Stokes
Subsonic inflow	4	5
Supersonic inflow	5	5
Subsonic outflow	1	4
Supersonic outflow	0	4
no-slip wall	-	4

Step 1: For each inviscid physical boundary condition imposed on the boundary, eliminate the corresponding conservation equations from the system.

Step 2: For each inviscid boundary condition, use corresponding LODI relation to express the unknown $\mathcal{L}_i's$ (corresponding to incoming waves) as a function of the known $\mathcal{L}_i's$ (corresponding to outgoing waves).

Step 3: Use the remaining conservation equations of the system combined with the values of $\mathcal{L}_i's$ from Step 2 to compute all variables which were not given by the inviscid boundary conditions.

In this section we simply copy two tables (Table C.2, C.3) from Poinsot and Lele (1992), which list several choices of physical boundary conditions for the 3-D Euler and Navier-Stokes equations. The implementation of the above general theory into special physical boundary conditions will be discussed in the subsequent sections.

For inflow, imposing u_1, u_2, u_3, ρ is well posed for Euler equations and an additional viscous condition is provided for the Navier-Stokes equations. This condition states that the normal stress is constant along the normal to the boundary. For multidimensional flows, the implementation of SI 4 is straightforward, but no satisfactory method could be found for SI 3.

For outflow, the spatial derivatives of the tangential viscous stresses τ_{12}, τ_{13} and normal heat flux $q_1 = -\lambda(\partial T/\partial x_1)$ were set to be zero. These conditions relax smoothly to the inviscid conditions when the viscosity and the conductivity go to zero.

Table C.2 Physical inflow boundary conditions for 3-D Navier-Stokes equations

	Navier-Stokes		
	Inviscid conditions	Viscous conditions	Total conditions
	4	0	4
SI 1 No well-posedness proof for NS	u_1 imposed u_2 imposed u_3 imposed T imposed		Special case: Euler and NS need same conditions
	4	1	5
SI 2 Well-posed for Euler. No proof for NS	u_1 imposed u_2 imposed u_3 imposed ρ imposed	$\frac{\partial \tau_{11}}{\partial x_1} = 0$	
	4	1	5
SI 3 Well-posed for Euler and NS	$u_1 - 2c/(\gamma - 1)$ imposed u_2 imposed u_3 imposed s imposed	$\frac{\partial \tau_{11}}{\partial x_1} = 0$	Unstable
	4	1	5
SI 4 Non-reflecting No proof for Euler and NS	$\mathcal{L}_1 = 0$ $\mathcal{L}_3 = 0$ $\mathcal{L}_4 = 0$ $\mathcal{L}_5 = 0$	$\frac{\partial \tau_{11}}{\partial x_1} = 0$	

Table C.3 Physical outflow/wall boundary conditions for 3-D Navier-Stokes equations

		Navier-Stokes	
	Inviscid conditions	Viscous conditions	Total conditions
	1	3	4
SO 1 Subsonic non-reflecting	p at infinity is imposed	$\frac{\partial \tau_{12}}{\partial x_1} = 0$ $\frac{\partial \tau_{13}}{\partial x_1} = 0$ $\frac{\partial q_1}{\partial x_1} = 0$	
	1	3	4
SO 2 Subsonic reflecting	p is imposed	$\frac{\partial \tau_{12}}{\partial x_1} = 0$ $\frac{\partial \tau_{13}}{\partial x_1} = 0$ $\frac{\partial q_1}{\partial x_1} = 0$	
	4	0	4
W 1 Isothermal no-slip wall	$u_1 = 0$ $u_2 = 0$ $u_3 = 0$ $T = cte$		
	3	1	4
W 2 Adiabatic no-slip wall	$u_1 = 0$ $u_2 = 0$ $u_3 = 0$	$q_1 = 0$	
	1	3	4
W 3 Adiabatic slip wall	$u_1 = 0$	$\tau_{12} = 0$ $\tau_{13} = 0$ $q_1 = 0$	

C.1.0.3 Subsonic Inflow Boundary Conditions

At a subsonic inflow boundary, four characteristic waves, $\mathcal{L}_1$, $\mathcal{L}_3$, $\mathcal{L}_4$, $\mathcal{L}_5$ are entering the domain while $\mathcal{L}_2$ is leaving the domain. Four physical boundary conditions are needed and many different choices exist. For example, we can impose u, v, w and T which is typical when we wish to control the inlet shear and introduce flow perturbation (Poinsot and Lele, 1992). Since $\mathcal{L}_2$ is an outgoing wave, it can be calculated by interior points and one-sided differences. The other four unkown incoming waves then are computed from Eqs. (C.9) to (C.12) in terms of $\mathcal{L}_2$ and time derivatives of u, v, w and T, which are known.

$$u(0,y,z,t) = U(y,z,t) \tag{C.20}$$

$$v(0,y,z,t) = V(y,z,t) \tag{C.21}$$

$$w(0,y,z,t) = W(y,z,t) \tag{C.22}$$

$$T(0,y,z,t) = T(y,z,t) \tag{C.23}$$

By using LODI system, the expression for $\mathcal{L}_i, (i \neq 2)$ are

$$\mathcal{L}_1 = -\frac{dU}{dt} + \mathcal{L}_2 \tag{C.24}$$

$$\mathcal{L}_3 = -\frac{dV}{dt} \tag{C.25}$$

$$\mathcal{L}_4 = -\frac{dW}{dt} \tag{C.26}$$

$$\mathcal{L}_5 = -\frac{dT}{dt} + \frac{T(\gamma-1)}{c}\left[\frac{dU}{dt} - 2\mathcal{L}_2\right] \tag{C.27}$$

C.1.0.4 Subsonic Outflow Boundary Conditions

For subsonic flow at exit, there is only one incoming wave, namely $\mathcal{L}_2$, which needs special treatment. The conventional method to provide a well-posed problem is to enforce $p = p_\infty$ at the outflow boundary. This treatment will however create acoustic wave reflections which may contaminate the flow solutions. On the other hand, a perfect non-reflecting boundary condition imposed by setting $\mathcal{L}_2 = 0$ is also problematic because there is nothing to prevent the pressure from drifting. An alternative solution to this dilemma is the partial-reflecting boundary condition proposed by Rudy and Strikwerda (1980) who modified the LODI relation

for pressure as

$$\mathcal{L}_2 = \mathcal{K}(p - p_\infty) - \mathcal{L}_1 \tag{C.28}$$

where $\mathcal{K}$ is determined by $\mathcal{K} = \sigma(1 - \mathcal{M}^2)c/L$. The preferred range for constant σ is $0.2 - 0.5$. L is the characteristic length of the domain and $\mathcal{M}$ is the maximum Mach number in the flow field.

C.1.0.5 Adiabatic and Isothermal Wall Boundary Conditions

From Table C.3, it can be seen at an adiabatic wall, all velocity components should vanish and the heat flux is zero. LODI relations (C.9), (C.10), and (C.11) show that $\mathcal{L}_2 = \mathcal{L}_1$ and $\mathcal{L}_4 = \mathcal{L}_5 = 0$. $\mathcal{L}_3$ also is zero because the normal velocity is zero.

For an isothermal wall, it is of interest to observe that $\mathcal{L}_2$ should be equal to $\mathcal{L}_1$ according to Eq. (C.9), however, from Eq. (C.12), $\mathcal{L}_2$ should be equal to $-\mathcal{L}_1$! This obvious contradiction is due to the improper LODI assumption in this situation: the source term Rq (see Eq. (2.61)) is typically large and cannot be ignored.

C.1.0.6 Incorporation of NSCBC into LU-SGS Scheme

In the simulations of developing flows, either hydrodynamically or thermally or both, it is preferred to use characteristic boundary conditions at the outflow to simple extrapolation. The reason is that simple extrapolation of both velocities and pressure neither satisfies the physics nor is able to maintain the correct friction velocity level inside the flow. We will use the partial-reflecting outflow boundary condition. The incoming wave $\mathcal{L}_2$ can be expressed as

$$\mathcal{L}_2 = \mathcal{K}(p - p_\infty) - \mathcal{L}_1. \tag{C.29}$$

As a result, the matrix $[\Lambda][S]^{-1}$ is changed to $[\Lambda S]'$ at the outflow boundary. In virtue of Eq. (B.10), we have

$$[\Lambda S]' = \begin{bmatrix} (u+c)c/(2\gamma p) & (u+c)/2 & 0 & 0 & 0 \\ -(u+c)c/(2\gamma p) & -(u+c)/2 & 0 & 0 & 0 \\ 0 & 0 & u & 0 & 0 \\ 0 & 0 & 0 & u & 0 \\ -u(\gamma-1)T/(\gamma p) & 0 & 0 & 0 & u \end{bmatrix} \tag{C.30}$$

and the Jacobian matrix $[A]'$ is therefore

$$[A]' = [T][S][\Lambda S]' = \begin{bmatrix} \frac{u(\gamma-1)}{\gamma T} & 0 & 0 & 0 & -\frac{pu}{T^2} \\ \frac{c(u+c)+u^2(\gamma-1)}{\gamma T} & \frac{p(u+c)}{T} & 0 & 0 & -\frac{pu^2}{T^2} \\ \frac{uv(\gamma-1)}{\gamma T} & 0 & \frac{pu}{T} & 0 & -\frac{puv}{T^2} \\ \frac{uw(\gamma-1)}{\gamma T} & 0 & 0 & \frac{pu}{T} & -\frac{puw}{T^2} \\ \frac{u[2c(u+c)+(u^2+v^2+w^2)(\gamma-1)]}{2\gamma T} & \frac{pu(u+c)}{T} & \frac{puv}{T} & \frac{puw}{T} & -\frac{pu(u^2+v^2+w^2)}{2T^2} \end{bmatrix}. \tag{C.31}$$

Also a new source term is introduced to the right hand side of Eq. (C.2):

$$[T]\frac{\partial \mathbf{W}}{\partial t} + [A]'\frac{\partial \mathbf{W}}{\partial x} = \mathbf{C}^{*\alpha}, \tag{C.32}$$

where $[A]' = [T][S][\Lambda S]'$ and

$$\mathbf{C}^{*\alpha} = \mathbf{C}^{*} - \mathbf{C}^{\alpha}. \tag{C.33}$$

The added source term $\mathbf{C}^{\alpha}$ is

$$\mathbf{C}^{\alpha} = [T][S]\begin{bmatrix} 0 \\ \mathcal{K}(p-p_\infty) \\ 0 \\ 0 \\ 0 \end{bmatrix} = \begin{bmatrix} 1 \\ u-c \\ v \\ w \\ H-uc \end{bmatrix} \cdot \frac{p\mathcal{K}(p-p_\infty)}{Tc}. \tag{C.34}$$

In the current study, the modified system is applied to the outflow surface, which is the east face of control volume (ni, j, k). For the interior control volumes, the original integral governing equations should be used for all six surfaces. For the near-boundary volume (ni, j, k), however,

only five faces of the hexahedron use the original equations since its east surface is subject to the new system. For system without preconditioning, Eq. 2.91 becomes

$$\frac{3\Omega}{2\Delta t}\Delta\mathbf{W} + [T]^{-1}[([A]'\Delta\mathbf{W}S)_1 - ([A]\Delta\mathbf{W}S)_3 \\ +([B]\Delta\mathbf{W}S)_2 - ([B]\Delta\mathbf{W}S)_4 + ([C]\Delta\mathbf{W}S)_5 - ([C]\Delta\mathbf{W}S)_6)] = -\mathbf{R}^m. \quad \text{(C.35)}$$

at the east boundary of the computational domain. Modifying the Jacobian matrices

$$[A] = [T][\tilde{A}]; \quad [B] = [T][\tilde{B}]; \quad [C] = [T][\tilde{C}] \quad \text{(C.36)}$$

and applying LUSGS decomposition results in

$$\begin{aligned}
[L] &= -[T]^{-1}\left[([T]_{ni,j,k}[\tilde{A}]^+)_{ni-1,j,k}S_3 + ([T][\tilde{B}]^+)_{ni,j-1,k}S_4 + ([T][\tilde{C}]^+)_{ni,j,k-1}S_6\right]; \\
[D] &= \frac{3\Omega}{2\Delta t} + [T]^{-1}_{ni,j,k}[([T][\tilde{A}]'^+)_{ni,j,k}S_1 - ([T][\tilde{A}]^-)_{ni,j,k}S_3 \quad \text{(C.37)} \\
&\quad +([T][\tilde{B}]^+)_{ni,j,k}S_2 - ([T][\tilde{B}]^-)_{ni,j,k}S_3 + ([T][\tilde{C}]^+)_{ni,j,k}S_5 - ([T][\tilde{C}]^-)_{ni,j,k}S_6]; \\
[U] &= -[T]^{-1}_{ni,j,k}\left[([T][\tilde{A}']^-)_{ni+1,j,k}S_1 + ([T][\tilde{B}]^-)_{ni,j+1,k}S_2 + ([T][\tilde{C}]^-)_{ni,j,k+1}S_5\right].
\end{aligned}$$

Compared with the original matrices, the lower matrix $[L]$ does not change but both the diagonal matrix $[D]$ and the upper matrix $[U]$ do change. In the above equations,

$$\begin{aligned}
[\tilde{A}]' &= [T]^{-1}[A]'; \\
[\tilde{A}]'^{\pm} &= \frac{1}{2}([\tilde{A}]' \pm \left|\lambda_{[\tilde{A}]'}\right|[I]).
\end{aligned} \quad \text{(C.38)}$$

In this case, the diagonal matrix $[D]$ is no longer diagonal:

$$\begin{aligned}
[D] &= \frac{3\Omega}{2\Delta t} + ([\tilde{A}]'^+ - [\tilde{A}]^-)S_{13} + (\left|\lambda_{[\tilde{B}]}\right|[I])S_{24} + (\left|\lambda_{[\tilde{C}]}\right|[I])S_{56} && \text{(C.39)} \\
&= \frac{3\Omega}{2\Delta t} + \frac{1}{2}\left[([\tilde{A}'] - [\tilde{A}]) + (\left|\lambda_{[\tilde{A}']}\right| + \left|\lambda_{[\tilde{A}]}\right|)[I]\right]S_{13} && \text{(C.40)} \\
&\quad +(\left|\lambda_{[\tilde{B}]}\right|[I])S_{24} + (\left|\lambda_{[\tilde{C}]}\right|[I])S_{56}, && \text{(C.41)}
\end{aligned}$$

where

$$[\tilde{A}]' - [\tilde{A}] = [T]^{-1}([A]' - [A]) = \begin{bmatrix} -u & -\gamma p & 0 & 0 & 0 \\ uc/(\gamma p) & c & 0 & 0 & 0 \\ 0 & 0 & 0 & 0 & 0 \\ 0 & 0 & 0 & 0 & 0 \\ -uT(\gamma-1)/(\gamma p) & -(\gamma-1)T & 0 & 0 & 0 \end{bmatrix}, \quad \text{(C.42)}$$

which contains four non-diagonal elements. Since the inversion of a diagonal matrix $[D]$ is trivial in LU-SGS scheme, we move the non-diagonal elements of $[D]$ to the corresponding locations of the lower and upper matrices,

$$[L'] = [L] + \begin{bmatrix} 0 & 0 & 0 & 0 & 0 \\ uc/(\gamma p) & 0 & 0 & 0 & 0 \\ 0 & 0 & 0 & 0 & 0 \\ 0 & 0 & 0 & 0 & 0 \\ -uT(\gamma-1)/(\gamma p) & -(\gamma-1)T & 0 & 0 & 0 \end{bmatrix}, \tag{C.43}$$

and

$$[U'] = [U] + \begin{bmatrix} 0 & -\gamma p & 0 & 0 & 0 \\ 0 & 0 & 0 & 0 & 0 \\ 0 & 0 & 0 & 0 & 0 \\ 0 & 0 & 0 & 0 & 0 \\ 0 & 0 & 0 & 0 & 0 \end{bmatrix}. \tag{C.44}$$

Then matrix $[D]$ becomes

$$[D'] = \frac{3\Omega}{2\Delta t} + (\left|\lambda_{[\tilde{B}]}\right|[I])S_{24} + (\left|\lambda_{[\tilde{C}]}\right|[I])S_{56} \tag{C.45}$$

$$+ \begin{bmatrix} -u/2 + \bar{\lambda}_A & 0 & 0 & 0 & 0 \\ 0 & c/2 + \bar{\lambda}_A & 0 & 0 & 0 \\ 0 & 0 & \bar{\lambda}_A & 0 & 0 \\ 0 & 0 & 0 & \bar{\lambda}_A & 0 \\ 0 & 0 & 0 & 0 & \bar{\lambda}_A \end{bmatrix} S_{13}, \tag{C.46}$$

where $\bar{\lambda}_A = (|\lambda_{[\tilde{A}']} + |\lambda_{[\tilde{A}]})/2$. And the new iteration equation for the near-boundary volume (ni, j, k) is

$$([L'] + [D'] + [U'])\Delta\mathbf{W} = -\mathbf{R}', \tag{C.47}$$

where $-\mathbf{R}' = -\mathbf{R} - [T]^{-1}\mathbf{C}^{\alpha}$.

Similarly, for preconditioning system, Eq. 2.101 becomes

$$[\Gamma]^{-1}[T]\frac{3\Omega}{2\Delta t}\Delta\mathbf{W} + [\Gamma]^{-1}[([A]'\Delta\mathbf{W}S)_1 - ([A]\Delta\mathbf{W}S)_3$$
$$+([B]\Delta\mathbf{W}S)_2 - ([B]\Delta\mathbf{W}S)_4 + ([C]\Delta\mathbf{W}S)_5 - ([C]\Delta\mathbf{W}S)_6)] = -\mathcal{R}^m \tag{C.48}$$

for the east boundary control volume. As a result, the matrices in the $L-D-U$ decomposition become

$$\begin{aligned}
[L] &= -[\Gamma]^{-1}_{ni,j,k}\left[([\Gamma][\tilde{A}]^{+})_{ni-1,j,k}S_3 + ([\Gamma][\tilde{B}]^{+})_{ni,j-1,k}S_4 + ([\Gamma][\tilde{C}]^{+})_{ni,j,k-1}S_6\right]; \\
[D] &= ([\Gamma]^{-1}[T])_{ni,j,k}\frac{3\Omega}{2\Delta t} + [\Gamma]^{-1}_{ni,j,k}[([\Gamma][\tilde{A}]'^{+})_{ni,j,k}S_1 - ([\Gamma][\tilde{A}]^{-})_{ni,j,k}S_3 \qquad \text{(C.49)} \\
&\quad +([\Gamma][\tilde{B}]^{+})_{ni,j,k}S_2 - ([\Gamma][\tilde{B}]^{-})_{ni,j,k}S_3 + ([\Gamma][\tilde{C}]^{+})_{ni,j,k}S_5 - ([\Gamma][\tilde{C}]^{-})_{ni,j,k}S_6]; \\
[U] &= -[\Gamma]^{-1}_{ni,j,k}\left[([\Gamma][\tilde{A}]'^{-})_{ni+1,j,k}S_1 + ([\Gamma][\tilde{B}]^{-})_{ni,j+1,k}S_2 + ([\Gamma][\tilde{C}]^{-})_{ni,j,k+1}S_5\right].
\end{aligned}$$

Compared with the original matrices, the lower matrix $[L]$ does not change but both the diagonal matrix $[D]$ and the upper matrix $[U]$ do change. In the above equations,

$$\begin{aligned}
[\tilde{A}]' &= [\Gamma]^{-1}[A]'; \\
[\tilde{A}]'^{\pm} &= \frac{1}{2}([\tilde{A}]' \pm \left|\lambda_{[\tilde{A}]'}\right|[I]). \qquad \text{(C.50)}
\end{aligned}$$

The diagonal matrix $[D]$ is simplified as

$$\begin{aligned}
[D] &= ([\Gamma]^{-1}[T])\frac{3\Omega}{2\Delta t} + ([\tilde{A}]'^{+} - [\tilde{A}]^{-})S_{13} + (\left|\lambda_{[\tilde{B}]}\right|[I])S_{24} + (\left|\lambda_{[\tilde{C}]}\right|[I])S_{56} \qquad \text{(C.51)} \\
&= ([\Gamma]^{-1}[T])\frac{3\Omega}{2\Delta t} + \frac{1}{2}\left[([\tilde{A}]' - [\tilde{A}]) + (\left|\lambda_{[\tilde{A}']}\right| + \left|\lambda_{[\tilde{A}]}\right|)[I]\right]S_{13} \qquad \text{(C.52)} \\
&\quad +(\left|\lambda_{[\tilde{B}]}\right|[I])S_{24} + (\left|\lambda_{[\tilde{C}]}\right|[I])S_{56}, \qquad \text{(C.53)}
\end{aligned}$$

and

$$[\tilde{A}]' - [\tilde{A}] = [\Gamma]^{-1}([A]' - [A]) = \begin{bmatrix} -\frac{u}{R} & -\frac{\gamma p}{R} & 0 & 0 & 0 \\ \frac{uc}{\gamma p} & c & 0 & 0 & 0 \\ 0 & 0 & 0 & 0 & 0 \\ 0 & 0 & 0 & 0 & 0 \\ \frac{uT(1-\gamma)}{\gamma p} & (1-\gamma)T & 0 & 0 & 0 \end{bmatrix}. \qquad \text{(C.54)}$$

The non-diagonal elements of $[D]$ were moved to the corresponding locations of the lower and upper matrices,

$$[L'] = [L] + \begin{bmatrix} 0 & 0 & 0 & 0 & 0 \\ \frac{uc}{\gamma p} & 0 & 0 & 0 & 0 \\ 0 & 0 & 0 & 0 & 0 \\ 0 & 0 & 0 & 0 & 0 \\ \frac{uT(1-\gamma)}{\gamma p} & (1-\gamma)T & 0 & 0 & 0 \end{bmatrix}, \qquad \text{(C.55)}$$

and

$$[U'] = [U] + \begin{bmatrix} 0 & -\frac{\gamma p}{R} & 0 & 0 & 0 \\ 0 & 0 & 0 & 0 & 0 \\ 0 & 0 & 0 & 0 & 0 \\ 0 & 0 & 0 & 0 & 0 \\ 0 & 0 & 0 & 0 & 0 \end{bmatrix}. \tag{C.56}$$

In this way, matrix $[D]$ becomes diagonal again:

$$[D'] = ([\Gamma]^{-1}[T])\frac{3\Omega}{2\Delta t} + (\left|\lambda_{[\tilde{B}]}\right|[I])S_{24} + (\left|\lambda_{[\tilde{C}]}\right|[I])S_{56}, \tag{C.57}$$

$$+\frac{1}{2}S_{13}\begin{bmatrix} -\frac{u}{R} + \bar{\lambda}_A & 0 & 0 & 0 & 0 \\ 0 & c + \bar{\lambda}_A & 0 & 0 & 0 \\ 0 & 0 & \bar{\lambda}_A & 0 & 0 \\ 0 & 0 & 0 & \bar{\lambda}_A & 0 \\ 0 & 0 & 0 & 0 & \bar{\lambda}_A \end{bmatrix}, \tag{C.58}$$

where $\bar{\lambda}_A = \left|\lambda_{[\tilde{A}']}\right| + \left|\lambda_{[\tilde{A}]}\right|$. And the new iteration equation for the near-boundary volume (ni, j, k) is

$$([L'] + [D'] + [U'])\Delta\mathbf{W} = -\mathcal{R}'. \tag{C.59}$$

BIBLIOGRAPHY

Anderson, D.M., McFadden, G.B. and Wheeler, A.A., 1998. Diffuse-interface methods in fluid mechanics. *Annual Review of Fluid Mechanics*, *30*, 139-165.

Armenio, V., Piomelli, U. and Fiorotto, V., 1999. Effect of the subgrid scales on particle motion. *Phys. Fluids*, *11*, 3030.

Balaras, E., 2004. Modeling complex boundaries using an external force field on fixed Cartesian grids in large-eddy simulations. *Computers & Fluids*, *33*, 375–404.

Belov, A., Martinelli, L. and Jameson, A., 1995. A new implicit algorithm with multigrid for unsteady incompressible flows calculations. *AIAA paper*, 95-0049.

Benocci, C. & Pinelli, A., 1990. The role of the forcing term in the large eddy simulation of equilibrium channel flow. *Engineering Turbulence Modeling and Experiments*, W. Rodi and E.N. Ganic, New York, 287-296.

Beyer, R.P. and LeVeque, R.J., 1992. Analysis of one-dimensional model for the immersed boundary method. *SIAM J. Numer. Anal.*, *29*, 332-364.

Benocci, C. and Pinelli, A. ,1990. The role of the forcing term in the large eddy simulation of equilibrium channel flow. *Engineering Turbulence Modeling and Experiments*, W. Rodi and E. N. Ganic (Eds), New York, 287–296.

Biemuller, M., Meyer, L. and Rehme, K., 1996. Large eddy simulation and measurement of the structure in two rectangular channels connected by a gap. *Engineering Turbulence Modeling and Experiments*, *3*, 249-258.

Billig, F.S., 1967. Shock-wave shapes around spherical- and cylindrical-nosed bodies. *J. Spacecraft, 4(6).*

Blackburn, H.M. and Henderson, R.D., 1999. A study of two-dimensional flow past an oscillating cylinder. *J. Fluid Mech.*, *385*, 255-286.

Boiron, O., Chiavassa, G. and Donat, R., 2009. A high-resolution penalization method for large Mach number flows in the presence of obstacles. *Computers & Fluids*, *38*, 703-714.

Boivin, M., Simonin, O. and Squires, K.D., 1998. Direct numerical simulation of turbulence modulation by particles in isotropic turbulence. *J. Fluid Mech.*, *375*, 235-263.

Carrara, M.D. and DesJardin, P.E., 2003. A filtered mass density function approach for modeling separated two-phase flows for LES I: Mathematical formulation. *Int. J. Multiphase Flow*, *32*, 365-384.

Cebeci, T. and Smith, A.M.O., 1974. Analysis of turbulent boundary layers. *Academic Press*, New York.

Chang, D. and Tavoularis, S., 2005. Unsteady numerical simulations of turbulence and coherent structures in axial flow near a narrow gap. *J. Fluid Eng.*, *127*, 458-466.

Chapman, D.R., 1979. Computational aerodynamics, development and outlook. *AIAA J.*, *17*, 1293-1313.

Chen, K.H. & Shuen, J.S., 1994. Three dimensional coupled implicit methods for spray combustion flows at all speeds. *AIAA paper*, 94-3047.

Choi, Y.-H. and Merkle, C. L., 1993. The application of preconditioning in viscous flows. *J. Comp. Phys.*, *105*, 207–223.

Choi, J.-II., Oberoi, R.C., Edwards, J.R. and Rosati, J.A., 2007. An immersed boundary method for complex incompressible flows. *J. Comp. Phys.*, *224*, 757-784.

Clift, R., Grace, J.R. and Weber, M.E. 1978. Bubbles, drops and particles. *Acacemic Press*, New York.

Colella, P., Graves, D.T., Keen, B.J. and Modiano, D., 2006. A Cartesian grid embedded boundary method for hyperbolic conservation laws. *J. Comp. Phys.*, *211*, 347-366.

Cristallo, A. and Verzicco, R., 2006. Combined immersed boundary/large-eddy-simulations of incompressible three dimensional complex flows. *Flow Turbulence Combust.*, *77*, 3-26.

Crowe, C.T., Sommerfeld, M. and Tsuji, Y., 1997. Multiphase flows with droplets and particles. *CRC; 1 edition.*

Dailey, L. D. (1997). Large eddy simulation of turbulent flows with variable property heat transfer using a compressible finite volume formulation. *Ph.D. Thesis*, Iowa State University, Ames, Iowa, U.S.A.

Deardroff, J.W., 1970. A numerical study of three-dimensional turbulence channel flow at large Reynolds number. *J. Fluid Mech.*, *41*, 452-456.

Dennis SCR and Chang G-Z, 1970. Numerical solutions for steady flow past a circular cylinder at Reynolds number up to 100. *J. Fluid Mech.*, *42*, 471-489.

Drew, D.A. and Passman, S.L. 1999. Theory of multicomponent fluids. *Springer-Verlag New York*, Inc.

Eckert, E.R.G. and Soehngen, E., 1952. Distribution of heat-transfer coefficients around circular cylinders in crossflow at Reynolds number from 20 to 500. *Tran. ASME*, *75*, 343-347.

Eggles, J.G.M., Unger, F., Weiss, M.H., Westerweel, J., Adria, R.J., Friedrich, R. and Nieuwstadt, F.T.M., 1994. Fully developed turbulent pipe flow: a comparison between direct numerical simulation and experiment. *J. Fluid Mech.*, *268*, 175-210.

Elghobashi S. and Truesdell G.C., 1993. On the two-way interaction between homogeneous turbulence and dispersed solid particles. I: Turbulence modification. *Phys. of Fluids, A 5(7)*, 1790-1801.

Fadlun, E.A., Verzicco, R., Orlandi, P. and Mohd-Y.J., 2000. Combined immersed-boundary finite-difference methods for three-dimensional complex flow simulations. *J. Comp. Phys.*, *161*, 35-60.

Favre, A., 1983. Turbulence: space-time statistical properties and behavior in supersonic flows. *Phys. of Fluids*, *26*, 2851-2863.

Feng, J. and Merkle, C. L., 1990. Evaluation of preconditioning methods for time-marching methods. *AIAA Paper*, 90-0016.

Fornberg, B., 1980. A numerical study of steady viscous flow past a circular cylinder, *J. Fluid Mech.*, *98*, 819.

Germano, M., Piomelli, U., Moin, P. & Cabot, W., 1991. A dynamic subgrid-scale eddy viscosity model, *J. Fluid Mech.*, *177*, 133-166.

Germano, M., 1992. Turbulence: the filtering approach, *J. Fluid Mech.*, *238*, 325-336.

Ghias, R., Mittal, R. and Dong, H., 2004. Large-eddy simulation of the tip flow of a rotor in hover, *AIAA Paper 2004-2432*.

Ghias, Mittal and Dong, 2007, A sharp interface immersed boundary method for compressible viscous flows, *J. Comput. Phys.*, *225*, 528-553.

Ghosal, S. and Moin, P., 1995. The basic equations for the large eddy simulation of turbulent flows in complex geometry. *Journal of Computational Physics*, *118*, 24–37.

Ghosal, S., Lund, T. S., Moin, P. and Akselvoll, K., 1995. A dynamic localization model for large-eddy simulation of turbulent flows. *Journal of Fluid Mechanics*, *286*, 229–255.

Gilmanov, A. and Acharya, S., 2006. An immersed boundary method and material point methodology for moving/compliant surfaces with heat transfer. *Proceedings of IMECE2006*, 2006 ASME International Mechanical Engineering Congress and Exposition, Chicago, IL.

Gnielinski, V., 1976. Neue gleichungen für den wärme- und den stoffübergang in turbulent durchströmenten rohren und kanalen. *Int. Chem. Eng.*, *16*, 359.

Goldstein, D., Handler, R. and Sirovich, L., 1993. Modeling a no-slip flow with an external force field. *J. Comp. Phys.*, *105*, 354.

Grigoriadis, D.G.E., Bartzis, J.G. and Goulas, A., 2004. Efficient treatment of complex geommetries for large eddy simulations of turbulent flows. *Comp. & Fluids*, *33*, 201-222.

Guellouz, M.S. and Tavoularis, S., 2000. The structure of turbulent flow in a rectangular channel containing a cylindrical rod-Part 1: Reynolds-averaged measurements. *Exp. Therm. Fluid Sci.*, *23*, 59-73.

Guilmineau, E. and Queutey, P., 2002. A numerical simulation of vortex shedding from an oscillating circular cylinder. *J. Fluids and Structures*, *16(6)*, 773-794.

Hedstrom, G. W., 1979. Non-reflecting boundary conditions for non-linear hyperbolic system. *J. Comp. Phys.*, *30*, 222–237.

Hooper, J.D., 1980. Developed single phase turbulent flow through a square-pitch rod cluster. *Nucl. Eng. Des.*, *60*, 365-379.

Hooper, J.D., Rehme, K., 1984. Large-scale structural effects in developed turbulent flow through closely-spaced rod arrays. *J. Fluid Mech.*, *145*, 305-337.

Hughes, T.J.R., Oberai, A.A. and Mazzei, L., 2001. Large eddy simulation of turbulent channel flows by the variational multiscale method. *Phys. Fluids*, *13*, 1784.

Iaccarino, G. and Verzicco, R., 2003, Immersed boundary technique for turbulent flow simulations, *Appl. Mech. Rev.*, *56(3)*, 331-347.

Ikeno, T. and Kajishima, T., 2005. Decay of swirling turbulent flow in rod-bundle. *J. of Fluid Sci. and Tech.*, *1(1)*, 36-47.

Ikeno, T. and Kajishima, T., 2007. Finite difference immersed boundary method consistent with wall conditions for incompressible turbulent flow simulations. *J. Comput. Phys.*, *226*, 1485-1508

Incropera, F.P., Dewitt, D.P., Bergman, T.L. and Lavine, A.S., 2005. *Fundamentals of Heat and Mass Transfer*, John Wiley & Sons, Inc.

Jones, O.C., 1976. An improvement in the calculation of turbulent friction in rectangualar ducts. *J. Fluids Engineering*, *98*, 173-181.

Jordan, S.A., 1999. A large-eddy simulation methodogy in generalized curvilinear coordinates. *J. Comp. Phys.*, *148*, 322–340.

Kasagi, N., Kuroda, A. and Hirata, M., 1989. Numerical investigation of near wall turbulent heat transfer taking into account the unsteady heat conduction in the solid wall. *J. Heat Transfer*, *111*, 53.

Kim, J. W. and Lee, D. J., 2000. Generalized characteristic boundary conditions for computational aeroacoustics. *AIAA Journal*, *38*, 2040-2049.

Kim, J. W. and Lee, D. J., 2004. Generalized characteristic boundary conditions for computational aeroacoustics, part 2. *AIAA Journal*, *42*, 47-55.

Kim, J., Kim, D. and Choi, H., 2001. An immersed-boundary finite-volume method for simulations of flow in complex geometries. *J. Comp. Phys.*, *171*, 132-150.

Kirkpatrick, M.P., Armfield, S.W. and Kent, J.H., 2003. A representation of curved boundaries for the solution of the Navier-Stokes equations on a staggered three-dimensional Cartesian grid. *J. Comp. Phys.*, *184*, 1-36.

Kuerten, J.G.M., 2006. Subgrid modeling in particle-laden channel flow. *Phys. Fluids*, *18*, 025108.

Lai, M.C. and Peskin, C.S., 2000. An immersed boundary method with formal second-order accuracy and reduced numerical viscosity. *J. Comp. Phys.*, *160*, 705-719.

Lee, K.B. and Jang, H.G., 1997. A numerical prediction on the turbulent flow in closely spaced bare rod arrays by a nonlinear $k - \epsilon$ model. *Nucl. Eng. Des.*, *172*, 351-357.

LeVeque, R.J. and Li, Z., 1994. The immersed interface method for elliptic equations with discontinuous coefficients and singular sources. *SIAM J. Numer. Anl.*, *31*, 1019.

Li, Z.L. and Ito, K., 2006. The immersed interface method – Numerical solutions of PDEs involving interfaces and irregular domains, *SIAM Frontiers in Applied Mathematics*, U.S.A, 2006.

Lilly, D.K., 1992. A proposed modification of the Germano subgrid-scale closure method. *Phys. Fluids A*, *4*, 633–635.

Linnick MN and Fasel HF, 2003. A high-order immersed boundary method for unsteady incompressible flow calculations. *AIAA 2003-1124*, In: 41st AIAA aerospace sciences meeting and exhibit, Reno, NV.

Mahesh, K., Constantinescu, G. and Moin, P., 2000. Large-eddy simulation of gas-turbine combustors. *CTR Annual Research Briefs*.

Mahesh, K., Constantinescu, G. and Moin, P., 2004. A numerical method for large-eddy simulation in complex geometries. *J. Comp. Phys.*, *197*, 215-240.

Majumdar, S., Iaccarino, G. and Durbin, P., 2001. RANS solvers with adaptive structured boundary non-conforning grids. *Center for Turbulence Research*, Annual Reserach Briefs, 353-366.

Mashayek, F. and Pandya, R.V.R. 2003. Analytical description of particle/droplet-laden turbulent flows. *Proc. Eng. Comb. Sci.*, *29*, 329-378.

Meneveau, C. and Katz J., 2000. Scale-invariance and turbulence models for large-eddy simulation. *Annual Review of Fluid Mechanics*, *32*, 1–32.

McEligot, D. M., 1986. Convective heat transfer in internal gas flows with temperature- dependent properties. *Adv. Transport Processes*, *4*, 113-200.

McEligot, D. M., Condie, K.G., McCreery, G.E., Mcllroy, H.M., Pink, R.J., Hochreiter, L.E., Jackson, J.D., Pletcher, R.H., Smith, B.L., Vukoslavcevic, P., Wallace, J.M., Yoo, J.Y., Lee, J.S., Ro, S.T. and Park, S.O., 2005. Advanced computational thermal fluid physics (CTFP) and its assessment for light water reactors and supercritical reactos. *Project 2002-016-K*, U.S.-RoK International Nuclear Energy Research Initiative, Final Technical Report, Oct. 2005.

Menter, F. and Esch, T., 2001, Advanced turbulence modeling in CFX. *CFX Update*, *20*, 4-5.

Miller, G.H. and Colella, P., 2002. A conservative three-dimensional Eulerian method for coupled solid-fluid shock capturing, *J. Comput. Phys.*, *183*, 26-82.

Mittal, R. Utturkar, Y. and Udaykumar, H.S., 2002. Computational modeling and analysis of biomimetic flight mechanisms. *AIAA paper*, 2002-0865.

Mittal, R. Bonilla, C. and Udaykumar, H.S., 2003. Cartesian grid methods for simulating flows with moving boundaries. *Computational Methods and Experimental Measurements-XI.*

Mittal, R. Seshadri, V. and Udaykumar, H.S., 2003. Flutter, tumble and vortex induced autorotation. *Theor. Comput. Fluid Dyn.*, *17(3)*, 165-170.

Mittal, R. and Iaccarino, G., 2005. Immersed boundary methods. *Annual Review of Fluid Mechanics*, *37*, 239-261.

Mohd-Yusof, J., 1997. Combined immersed-boundary/B-spline methods for simulations of flow in complex geometries. *CTR Annual Research Briefs*.

Mohd-Yusof, J., 1998. Development of immersed boundary methods for complex geometries. *CTR Annual Research Briefs*.

Moin, P., Squires, K., Cabot, W. and Lee, S., 1991. A dynamic subgrid-scale model for compressible turbulence and scalar transport. *Phys. Fluids A*, *3*, 2746-2757.

Moin, P., 2002, Advances in large eddy simulation methodology for complex flows, *Int. J. Heat and Fluid Flow*, *23*, 710-720.

Oesterle, B. and Zaichik, L.I., 2004. On Lagrangian time scales and particle dispersion modeling in equilibrium turbulent shear flows. *Phys. Fluids*, *16(9)*, 3374-3384.

Ovchinnikov, V., Piomelli, U. and Choudhari, M.M., 2006, Numerical simulations of boundary-layer transition induced by a cylinder wake. *J. Fluid Mechanics*, *547*, 413-441.

Pacheco-Vega, A., Pacheco J.R. and Rodiċ, T., 2007. An immersed-boundary method for compressible viscous flows. *Computers & Fluids*, *35*, 693-702.

Pai, M.G. and Subramaniam, S., 2006. Modeling interphase turbulent kinetic energy transfer in Lagrangian-Eulerian spray computations. *Atomization and Sprays*, *16*, 807-826.

Pai, M.G. and Subramaniam, S., 2007. Modeling droplet dispersion and interphase turbulent kinetic energy transfer using a new dual-timescale Langevin model. *Int. J. Multiphase Flow*, *33(3)*, 252-281.

Palma, P.D., Tullio, M.D., Pascazio, G. and Napolitano, M., 2006, An immersed-boundary method for compressible viscous flows, *Computers & Fluids*, *35*, 693-702.

Pan, K.L., Shyy, W. and Law, C.K., 2002. An immersed-boundary method for the dynamics of premixed flames. *Int. J. Heat and Mass Tran.*, *45*, 3503-3516.

Pao, Y.H., 1965. Structure of turbulent velocity and scalar fields at large wave numbers. *Phy. Fluids*, *8*, 1063-1075.

Peskin, C.S., 1972. Flow patterns around heart valves: a numerical method. *J. Com. Phys.*, *10*, 252-271.

Piomelli, U. and Liu, J., 1995. Large-eddy simulation of rotating channel flows using a localized dynamic model. *Physics of Fluids*, *7*, 839–848.

Piomelli, U. and Balaras, E., 2002. Wall-layer models for large-eddy simulations. *Annu. Rev. Fluid Mech.*, *34*, 349-374.

Pletcher, R. H. and Chen, K.-H., 1993. On solving the compressible Navier-Stokes equations for unsteady flows at very low Mach numbers. *AIAA Paper*, 93-3368.

Poinsot, T. J. and Lele, S. K., 1992. Boundary conditions for direct simulations of compressible viscous flows. *J. Comp. Phys.*, *101*, 104–129.

Pope, S.B. 2000. Turbulent flows. *Cambridge University Press*, U.K.

Pozorski, J., Apte, S.V. and Raman, V., 2004. Filtered particle tracking for dispersed two-phase turbulent flows. *Proceeding of the Summer Program*, Center for Turbulece Research.

Qin, Z.H., 2007. Large eddy simulation of turbulent heat transfer in stationary and rotating square ducts. *Ph.D. Thesis*, Iowa State University, Ames, Iowa, U.S.A.

Rehme, K., 1989. Experimental observations of turbulent flow through subchannels of rod bundles. *Exp. Therm. Fluid Sci.*, *2*, 341-349.

Rehme, K., 1978. The structure of turbulent flow through a wall subchannel of a rod bundle. *Nuclear Engineering and Design*, *45*, 311-323.

Rehme, K., 1987. The structure of turbulent flow through rod bundles. *Nuclear Engineering and Design*, *99*, 141-154.

Rehme, K., 1992. The structure of turbulence in rod bundles and the implications on natural mixing between the subchannels. *Int. J. Heat Mass Transfer*, *35*, 567-581.

Rieger, H. and Jameson, A., 1988. Solution of steady three dimensional compressible Euler and Navier Stokes equations by an implicit LU scheme. *AIAA Paper*, 88-0619.

Robinson, S.K. ,1991. Coherent motions in the turbulent boundary layer. *Annu. Rev. Fluid Mech.*, *23*, 601-639.

Rudy, D. H. and Strikwerda, J. C., 1980. A nonreflecting outflow boundary condition for subsonic Navier-Stokes calculations. *J. Comp. Phys.*, *36*, 55–70.

Saiki, E.M. and Biringen, S., 1996. Numerical simulation of a cylinder in uniform flow: application of a virtual boundary method, *J. Comput. Phys.*, *123*, 450-465.

Sankaran, V., and Menon, S., 2002. LES of spray combustion in swirling flows. *J. Turb.*, *3*, 1-23.

Satake, S. and Kunugi, T., 1999. Direct numerical simulation of turbulent pipe flow with uniform surface heat flux. *Trans. JSME*, *192*.

Schlichting H., 1979. Boundary layer Theory. *McGraw-Hill, Inc.*, New York.

Silva, L.E. ALF, Silveira-Neto A, Damasceno JJR, 2003. Numerical simulation of two-dimensional flows over a circular cylinder using the immersed boundary method. *J. Comp. Phys.*, *189*, 351.

Simonin, O., Zaichik, L.I., Alipchenkov, V. and Fevier, P. 2006. Connection between two statistical approaches for the modeling of particle velocity and concentration distributions in turbulent flow: The mesoscopic Eulerian formalism and the two-point probability density function method. *Phys. Fluids*, *18*, 125107.

Smagorinsky, J., 1963. General circulation experiments with the primitive equations. I. The basic experiment. *Monthly Weather Review*, *91*, 99–164.

Smith, B.L. *http://www.efdl.usu.edu/KNERI/KNERI.html.*

Smith, B.L., 2005. Particle image velocimetry measurements of turbulent flow through a rod bundle. *DOE Report DE-AC07-05ID14517.*

Spyropoulos, E. T. and Blaisdell, G. A., 1995. Evaluation of the dynamic subgrid-scale model for large eddy simulation of compressible turbulent flows. *AIAA Paper*, 95-0355.

Squires, K.D. and Eaton, J.K., 1990. Particle response and turbulence modification in isotropic turbulence. *Phys. of Fluids*, *A 2(7)*, 1191-1203.

Stolz, S., Adams, N.A. and Kleiser, L., 2001. An approximate deconvolution model for large-eddy simulation with application to incompressible wall-bounded flows. *Phys. Fluids*, *13*, 997.

Su, S.W., Lai, M.C. and Lin, C.A., 2007. An immersed boundary technique for simulating complex flows with rigid boundary. *Computers & Fluids*, *36*, 313-324.

Subramaniam, S. 2003. Modeling turbulent two-phase flows. *Proc. of 16th Annual Conference on Liquid Atomization and Spray Systems*, Int. Liquid Atomization and Spray System Soc., Monterey.

Sundaram, S. and Collins, L., 1997. Collision statistics in an isotropic particle-laden turbulent suspension. Part 1. Direct numerical simulations. *J. Fluid Mech.*, *335*, 75-109.

Sundaram, S. and Collins, L., 1999. Collision statistics in an isotropic particle-laden turbulent suspension. Part 1. Direct numerical simulations. *J. Fluid Mech.*, *335*, 75-109.

Tannehill, J.C., Anderson, D.A. and Pletcher, R.H., 1997, Computational fluid mechanics and heat transfer, 2nd ed., *Taylor & Francis.*

Tyagi, M. and Acharya S., 2005. Large eddy simulation of turbulent flows in complex and moving rigid geometries using the immersed boundary method. *Int. J. Numer. Meth. Fluids*, *48*, 691-722.

Tessicini, F., Iaccarino, G., Fatica, M., Wang M. and Verzicco, R., 2002. Wall modeling for large-eddy simulation using an immersed boundary method. *Center for Turbulent Research, Annual Research Briefs.*

Thompson, K. W., 1987. Time dependent boundary conditions for hyperbolic systems. Part 1. *J. Comp. Phys.*, *68*, 1–24.

Thompson, K. W., 1990. Time dependent boundary conditions for hyperbolic systems. Part 2. *J. Comp. Phys.*, *89*, 439–461.

Thompson, P. A. and Troian, S. M., 1997. A general boundary condition for liquid flow at solid surfaces. *Letters to Nature*, *389* (25), 360–362.

Tritton, D.J., 1959. Experiments on the flow past a circular cylinder at low Reynolds number, *J. Fluid Mech.*, *6*, 547.

Tseng, Y.-H. and Ferziger, J.H., 2003. A ghost-cell immersed boundary method for flow in complex geometry. *J. Comp. Phys.*, *192*, 593-623.

Turkel, E., 1987. Preconditioned methods for solving the incompressible and low speed compressible equations. *J. Comp. Phys.*, *72*, 277–298.

Udaykumar, H.S., Mittal, R., Rampungoon, P. and Khanna, A., 2001. Computation of solid-liquid phase front in the sharp interface limit on fixed grids. *J. Comp. Phys.*, *153*, 534-574.

Udaykumar, H.S., Mittal, R., Rampungoon, P. and Khanna, A., 2001. A sharp interface Cartesian grid method for simulation flows with complex moving boundaries. *J. Comp. Phys.*, *174*, 345-380.

Udaykumar, H.S., Mittal, R., Rampungoon, P., 2002. Interface tracking finite volume method for complex solid -fluid interactions on fixed meshes. *Commun. Numer. Methods Eng.*, *18*, 89-97.

Uijttwaal, W.S.J. and Oliemans, R.V.A., 1996. Particle dispersion and deposition in direct numerical and large eddy simulation of vertical pipe flows. *Phys. Fluids*, *8*, 2590.

Verzicco, R., Fatica, M., Iaccarino and Orlandi, P., 2004. Flow in an impeller-stirred tank using an immersed-boundary method. *AIChE J.*, *50*, 1109-1118.

Vinkovic, I., Aguirre, C., Ayrault, M. and Serge, S., 2006. Large-eddy simulation of the dispersion of solid particles in a boundary layer. *Boundary Layer Meterology*, *121(2)*, 283-311.

Vitturi, M.M., Ongaro, T.E., Neri, A., Salvetti, M.V. and Beux, F., 2007. An immersed boundary method for compressible multiphase flows: application to the dynamics of pyrocalstic density currents. *Comput. Geosci.*, *11*, 183-198.

Vreman, B., Geurts, B. and Kuerten, H., 1995. Subgrid-Modeling in LES of compressible flow. *Applied Scientific Research*, *54*, 191–203.

Vreman, A.W., 2003. The filtering analog of the variational multiscale method in large-eddy simulation. *Phys. Fluids*, *15*, L61.

Wang, L.P. and Squires, K.D., 1996. Large eddy simulation of particle-laden turbulent channel flow. *Phys. Fluids*, *8*, 1207-1223.

Wang, M. and Moin, P., 2000. Computation of trailing-edge flow and noise using large -eddy simulation. *AIAA J.*, *38*, 2201-2209.

Wang, M. and Moin, P., 2002. Dynamic wall modeling for large-eddy simulation of complex turbulent flows, *Phys. of Fluids*, *14(7)*, 2043-2051.

Wang, W.-P. and Pletcher, R.H., 1996. On the large eddy simulation of a turbulent channel flow with significant heat transfer. *Phys. Fluids*, *8(12)*, 3354-3366.

Wang, A.B., Tràvnìĉek Z. and Chia, K.C., 2000. On the relationship of effective Reynolds number and Strouhal number for the laminar vortex shedding of a heated circular cylinder. *Phys. Fluids*, *12(6)*, 1401-1410.

Wang, W. and Pletcher, R.H., 2008. Large eddy simulation of duct sub-channel flows with non-body conformal grids, submitted to International Journal of Heat and Fluid Flow. August, 2008.

Williamson, C.H.K., 1996. Vortex dynamics in the cylinder wake. *Annu. Rev. Fluid Mech.*, *28*, 477-539.

Winkler, C.M., Rani, S.L. and Vanka, S.P., 2006. A numerical study of particle wall-deposition in a turbulent square duct flow. *Pow. Tech.*, *170*, 12-25.

Wu, X. and Trupp, A.C., 1994. Spectral measurements and mixing correlation in simulated rod bundle subchannels. *Int. J. Heat Mass Transfer*, *37(8)*, 1277-1281.

Wu, X., 1994. Numerical study on the turbulence structures in closely spaced rod bundle subchannels, *Num. Heat Trans., Part A 25*, 649-670.

Xu, S. and Wang, Z.J., 2006. An immersed interface method for simulating the interaction of a fluid with moving boundaries. *J. Comp. Phys.*, *216*, 454-493.

Xu, X. F., 2003. Large eddy simulation of compressible turbulent pipe flow with heat transfer. *Ph.D. Thesis*, Iowa State University, Ames, Iowa, U.S.A.

Xu, X. F., Lee, J. S., Pletcher, R. H., Shehata, A. M. and McEligot, D. M., 2004. Large eddy simulation of turbulent forced gas flows in vertical pipes with high heat transfer rates. *International Journal of Heat and Mass Transfer*, *47*, 4113–4123.

Xu, X.F. and Plecther, R., 2005. A compressible finite volume formulation for large eddy simulation of turbulent pipe flows at low Mach number in Cartesian coordinates. *J. Comp. Phys.*, *203*, 22-48.

Xu, Y. and Subramaniam S., 2006. A multiscale model for dilute turbulent gas-particle flows based on the equilibration of energy concept *Physics of Fluids*, *18(3)*, 033301.

Yamamoto, R., Nakayama, Y. and Kim, K., 2004. A smooth interface method for simulating liquid crystal colloid dispersions. *J. Phys.: Condensed matter*, *16*, 1945-1955.

Yamamoto, Y., Pottohoff, M., Tanaka, T., Kajishima, T. and Tsuji, Y., 2001. Large eddy simulation of turbulent gas-particle flow in a vertical channel: effect of considering inter-particle collisions. *J. Fluid Mech.*, *442*, 303-334.

Yang, G., Causon, D.M., Ingram, D.M., Saunders, R. and Batten, P., 1997. A Cartesian cut cell method for compressible flows Part B: Moving body problems. *Aeronautical J.*, *101(1002)*, 57-65.

Yang, J. and Balaras, E., 2006. An embedded-boundary formulation for large-eddy simulation of turbulent flows interacting with moving boundaries. *J. Comp. Phys.*, *215*, 12-40.

Ye, T., Mittal, R., Udaykumar, H.S. and Shyy, W., 2003. An accurate Cartesian grid method for viscous incompressible flows with complex immersed boundaries. *J. Comp. Phys.*, *156*, 209-240.

Yoon, S. and Jameson, A., 1987, An LU-SSOR scheme for the Euler and Navier-Stokes equations. *AIAA Paper*, 87-600.

You, D., Mittal, R., Wang, M. and Moin, P., 2003. Study of rotor tip-clerance flow using large eddy simulation, *AIAA J.*, 0838.

You, D., Mittal, R., Wang, M. and Moin, P., 2004. Computational methodology for large-eddy simulation of tip- clearance flows. *AIAA J.*, 271-279.

Mohd-Yusof, J., 1996. Interaction of massive particles with turbulence. *PhD thesis*, Cornell University.

Yuu, S., Ueno, T. and Umekage, T., 2001. Numerical simulation of the high Reynolds number slit nozzle gas-particle jet using subgrid-scale coupling large eddy simulation. *Chem. Eng. Sci.*, *56*, 4293-4307.